Modeling, Analysis and Control of a Variable Flux Machine

Bigyan Basnet

A Thesis

In the Department

of

Electrical and Computer Engineering

Presented in Partial Fulfillment of the Requirements

For the Degree of

Doctor of Philosophy (Electrical and Computer Engineering) at

Concordia University

Montréal, Québec, Canada

June 2021

CONCORDIA UNIVERSITY

SCHOOL OF GRADUATE STUDIES

This is to certify that the thesis prepared

By: Bigyan Basnet

Entitled: Modeling Analysis and Control of a Variable Flux Machine

and submitted in partial fulfillment of the requirements for the degree of

Doctor of Philosophy (Electrical & Computer Engineering)

complies with the regulations of the University and meets the accepted standards with respect to originality and quality.

Signed by the final examining committee:

_____Chair
Dr. Muthu Packirisamy

_____External Examiner
Dr. Emmanuel B. Agamloh

_____External to Program
Dr. Anjali Awasthi

_____Examiner
Dr. Luiz A.C. Lopes

_____Examiner
Dr. Chunyan Lai

_____Supervisor
Dr. Pragasen Pillay

Approved by _____
Dr. Wei- Ping Zhu , Graduate Program Director

16, June , 2020 _____
Dr. Mourad Debbabi, Dean,
Gina Cody School of Engineering & Computer Science

ABSTRACT

Modeling, Analysis and Control of a Variable Flux Machine

Bigyan Basnet, Ph.D.
Concordia University, 2021

Electric motors are the key elements in electric propulsion systems. The performance of Electric vehicles (EVs) significantly depends on the electric motors. Permanent magnet synchronous machines (PMSMs) with rare-earth magnets are widely used in EV applications because they fulfill most requirements of EV motors. However, low efficiency at high speed, limited resources and fluctuating prices of rare-earth permanent magnets (PMs) have forced industries to develop alternatives to rare-earth machine technologies. Recently, Variable-Flux PMSMs (VF-PMSMs) also known as memory motors have been introduced to overcome the drawbacks of PMSMs. This thesis focuses on the modeling, analysis and control of the Aluminum-Nickel-Cobalt (AlNiCo) magnet-based VF-PMSMs.

This thesis presents the effect of different magnetization pulse widths and methods on the magnetization level, back-EMF and no-load losses of the VF-PMSM. The injection of the magnetization or de-magnetization current pulse will change the magnet flux linkage and back-EMF harmonics. An adaptive nonlinear filter is used to estimate the back-EMF during the motoring mode. The harmonics present in the machine back-EMF due to different magnetization and de-magnetization current pulse widths and magnetization methods are analyzed. Besides, the quality of the back-EMF for different speeds and machine no-load losses are presented for different magnetization states (MSs).

During de-magnetization and re-magnetization, a $d-axis$ current pulse is injected to change the MS. However, the injected $d-axis$ current abruptly changes the magnet flux linkage changing the magnet torque as well as reluctance torque and results in a pulsating torque. To solve this pulsating torque issue, a $q-axis$ current reference during the re-magnetization is determined by two different methods: voltage limit method and load torque method. The derived $q-axis$ current reduces the torque pulsation during the re-magnetization.

A closed-loop current controller-based parameter measurement of VF-PMSMs for different MSs is presented. Automated machine parameters such as flux linkage, inductance and resistance are generated in real-time by the real-time processor.

A co-simulation-based VF-PMSM drive system and loss analysis due to pulse-width modulation (PWM) inverter drive is presented. An integrative simulation approach gives higher fidelity results since it includes magnetic saturation (inductance nonlinearities), machine geometry (torque ripple and spatial harmonics) effects. Besides, the comparative effect of the sinusoidal current and PWM inverter fed VF-PMSM's losses have been studied. The co-simulation results are validated with the conventional simulation (dq −mathematical model) model, finite element model and experimental results.

ACKNOWLEDGEMENT

I would like to express my deep gratitude to my supervisor, Professor Pragasen Pillay for his continuous support, motivation, enthusiasm, and immense knowledge. He has inspired me in many ways, from the beginning to the end of my research program. His guidance helped me during all times of my research and writing of this thesis.

Besides my advisor, I would also like to thank my committee: Associate Professor Emmanuel B. Agamloh, Professor Anjali Awasthi, Professor Luiz A.C. Lopes and Assistant Professor Chunyan Lai for their insightful comments, suggestions and their valuable time.

I thank my fellow labmates in the PEER group at Concordia University for being supportive during my Ph.D. journey. Sincere thanks to Dr. Akrem Mohamed Aljehaimi, Dr. Mohammad A. Masadeh, Dr. Rajendra Thike, Dr. Mathews Boby, Dwaipayan, Sumeet, Mohan, Yupeng and Tamenwe for their help and advice.

I would like to express my deepest gratitude to my parents and wife Manisha, for their continuous encouragement and support.

I would like to acknowledge the support of the Natural Sciences & Engineering Research Council of Canada and Concordia University. This work is done as part of NSERC/Hydro-Québec Senior Industrial Research Chair entitled “Design and Performance of Special Electrical Machines” held by Professor Pragasen Pillay at Concordia University. This research is also partly funded by the NSERC Discovery Grant entitled "Novel Electric Machine Design Topologies For Electrified Transportation".

TABLE OF CONTENTS

LIST OF FIGURES

LIST OF TABLES

LIST OF ABBREVIATIONS

EV	Electric Vehicle
NdFeB	Neodymium Magnet (rare-earth permanent magnet)
AlNiCo	Aluminum-Nickel-Cobalt
PM	Permanent Magnet
PMSM	Permanent Magnet Synchronous Machine
IPMSM	Interior Permanent Magnet Synchronous Machine
VF-PMSM	Variable Flux Machine
VF-PMSM	Variable Flux- Permanent Magnet Synchronous Machine
MSs	Magnetization States
FOC	Field Oriented Control
FW	Field Weakening
Low-Hc	Low Coercivity
LCF	Low Coercivity Force
$d-axis$	Direct Axis
$q-axis$	Quadrature Axis
EMF	Electromotive Force
PWM	Pulse Width Modulation
VSI	Voltage Source Inverter
FEM	Finite Element Model
FEA	Finite Element Analysis
FFT	Fast Fourier Transform
hp	Horse Power
DC	Direct current
MTPA	Maximum Torque Per Ampere
kW	KiloWatt
ms	Millisecond

VFD	Variable Frequency Drive
SPWM	Sinusoidal Pulse Width Modulation
SVPWM	Space Vector Pulse Width Modulation
THD	Total Harmonic Distortion

LIST OF SYMBOLS

Symbol	Unit	Definition
v_d	V	d-axis stator voltage
v_q	V	q-axis stator voltage
V_s	V	Maximum available voltage
i_d	A	d-axis current
i_q	A	q-axis current
I_s	A	Peak value of rated stator current
L_d	H	d-axis inductance
L_q	H	q-axis inductance
$\lambda_m(i_d)$	Wb-turn or V.s	Magnet flux linkage
λ_f	Wb-turn or V.s	Magnet flux linkage at fully magnetized state
R_s	Ω	Stator winding resistance
ω_e	rad/sec	Electrical angular speed
ω_m	rpm	Mechanical angular speed
T_e	N.m	Electromagnetic torque
T_l	N.m	Load torque
$V_{n,p}$	V	no-load phase back-EMF
P		Number of pole pairs
p		Derivative
V_{dc}	V	DC bus voltage
B	T	Magnetic flux density
Br	T	Remnant magnet flux density of the magnet
H	A/m	Magnetic field intensity
λ_d	Wb-turn or V.s	Air-gap flux linkage d-axis component
λ_q	Wb-turn or V.s	Air-gap flux linkage q-axis component

θ_r	rad	Rotor angle
*		superscript indicates the reference value
^		superscript indicates the estimated value

Chapter 1. Introduction

1.1 Research Background

Electric motors are the key elements in electric propulsion systems. The performance of Hybrid electric vehicles (HEVs) or pure electric vehicles (EVs) can be significantly improved by relevant improvements in electric motors. High torque, high power density, high starting torque, high efficiency over a wide range of speed (3-4 per unit speed), intermittent overload capability for short durations are the major requirements of EV's electrical machines [1], [2], [3].

With the progress in materials, power electronics, and control drive technologies various electric motors have been developed over the past few decades. The permanent magnet synchronous motors (PMSMs) and induction motors (IMs) are currently the two most dominant motors in EVs/HEVs [4]. IMs are widely used in EVs/HEVs, especially in early designs due to the robust structure, relatively low cost, well-established manufacturing techniques, comparatively good efficiency and peak torque capability, and good dynamic performance which can be achieved by vector control or direct torque control. However, IMs have a narrow constant power speed range (2-3 per unit speed), lower efficiency compared to PMSM due to the inherent rotor loss and lower power factor [5].

Although the synchronous reluctance motors (SynRMs) are robust and have relatively lower cost, their use in EVs/HEVs is still immature due to poor torque and overloading capabilities, low power factor, and high torque ripple which results in higher noise and vibration [4].

Rare earth PMSMs have been widely utilized in EV applications thanks to their high torque densities, high efficiencies, and wide constant power region [6], [7]. PMSMs are operated at high speed using continuous flux weakening current [8], [9]. However, the continual flux weakening current increases ohmic and core losses and reduces efficiency in the flux weakening region. Besides, limited flux weakening capability, fluctuating price, and limited resources of rare-earth permanent magnets (PMs) have forced industries to develop alternatives to rare-earth machine technologies.

Ferrite magnets are inexpensive; however, a reduction of the torque component is unavoidable when ferrite PMs are adopted since its residual flux density is one-third of that of the NdFeB magnet [10]. Although low coercive field (LCF) magnets, like Alnico [11] provide comparable magnet flux density to rare earth PM used in PMSMs, they are rarely employed in the present machines because the magnets are often easily demagnetized by the stator field. If PMSMs with AlNiCo are designed with controllable de-magnetization, they will provide equivalent torque densities compared to rare-earth PMSMs [12], [13], [14].

1.2 Variable-flux Machines

Variable-flux PMSMs (VF-PMSMs) also named as VFMs or memory motors have gained popularity and were developed by Ostovic [15], [16]. The major benefits of VF-PMSMs over the rare earth PMSMs are achieving a wide torque-speed envelope with minimum energy losses caused by field weakening and achieving a similar performance with reduced rare earth material. The VF-PMSMs can dynamically change the intensity of magnetization and memorize the flux density level in the rotor magnets, and therefore is referred to as Memory Motors [16]. Recent studies have introduced the VF-PMSMs as a strong rival to the PMSMs for applications including electrified transportation [17], [18], [19]. Besides, the high Curie temperature of LCF magnets allows VF-PMSMs to be used in harsh environments. Therefore VF-PMSMs could be a potential choice where extended speed range, as well as high operating temperature, are required [20], [21], [22], [23].

Generally, the existing VF-PMSMs can be divided into AC- magnetized types [24], [11], [15], [17], [25], [26] and DC-magnetized types [27], [28], [29] based on the current pulse pattern. The AC-magnetized VF-PMSMs employ stator armature winding to produce a $d-axis$ current pulse using vector control. The benefits of using armature windings are simple structures similar to the conventional PM machines, as well as fewer circuit components and cost. However, the drawbacks are high requirements on the armature winding and inverter rating [30]. If the relatively weak LCF magnets are solely employed, the torque densities are lower than the counterparts equipped with rare earth PMSMs. Therefore, hybrid topologies incorporating rare-earth PM and LCF magnet are utilized for high speed, high torque applications [31], [32]. The hybrid variable flux topologies can be

divided into series and parallel. The overall categorization of the existing VF-PMSMs is illustrated in Fig.1-1.

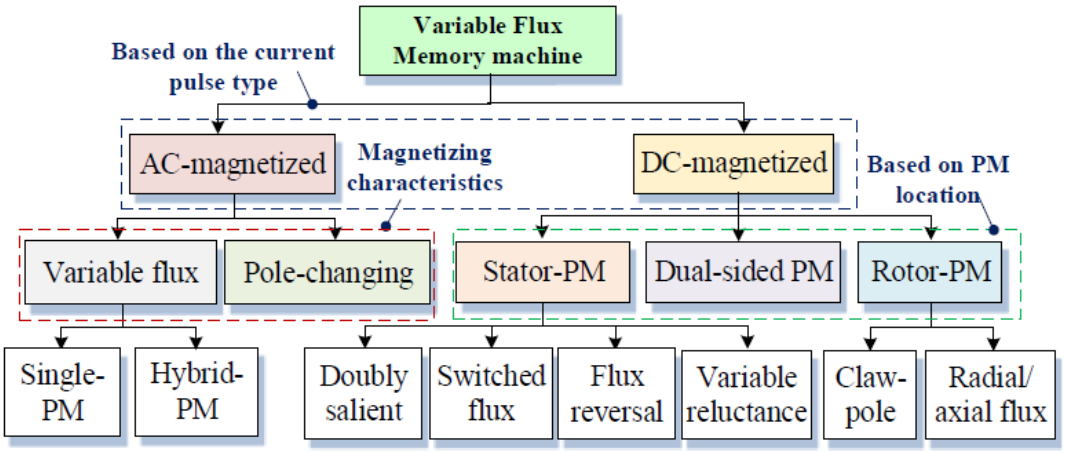

Fig.1-1 Categorization of variable flux memory machines [20].

In this thesis, a tangentially magnetized single PM variable flux machine is considered. The VF-PMSMs can be magnetized and demagnetized to the specified magnetization state (MS) by supplying a current pulse. This eliminates the requirement for continuous flux weakening current in the high-speed region, which results in higher efficiency than PMSMs [25], [33].

A high starting torque as well as a wide speed range is achieved with different MSs. Moreover, the pulse current duration of a few milliseconds (ms) dissipates negligible losses compared to the flux weakening of conventional PMSMs.

The VF-PMSM designed as a traction machine achieves 18% (city drive) to 35% (highway drive) loss reduction compared to interior PMSMs [34]. This makes the VF-PMSMs an attractive option for the motor drive system in electric vehicle applications [35], [36].

1.3 Recent Advances in Variable Flux Machines

In the last decade, VF-PMSMs have experienced rapid technical advancements and received growing research interests from research scholars and EV manufacturers worldwide [30]. The motivation behind the VF-PMSM research interest is the possibility to combine the high torque density of conventional rare-earth PM machines with variable PM flux characteristics for manipulating losses. The MS can be "memorized" by a specific current pulse, allowing field weakening (FW) control current to be greatly reduced and the corresponding losses minimized. Also, since the back EMF can be controlled due to the variable flux property, the inverter failure under high-speed operation can be well prevented [30].

New VF-PMSM topologies and related control strategies are emerging. Various novel VF-PMSMs are published with particular reference to their topologies, characteristics, the working principle, and related control techniques. To overcome the drawbacks in the existing VF-PMSMs, some new designs are introduced for performance improvement.

1.3.1 Single PM VF-PMSM

For the conventional VF-PMSMs design with $Lq>Ld$, it is difficult to avoid unintentional de-magnetization. Thus, the PM flux linkage cannot be fully utilized. In order to fully use the magnet flux, flux intensified VF-PMSMs are proposed [24], [12], [37]. Fig.1-2 shows a VF-PMSM with a single LCF magnet material. This type of machine is tangentially magnetized. The flux intensified VF-PMSMs are designed to have a wider torque-speed envelope while reducing the losses especially resulting from high speed field weakening operation. The flux-concentrated flux intensified VF-PMSM design with a reduced magnetizing current is proposed in [38].

Precise MS control is a critical issue and various control schemes are proposed [39], [40], [41]. To obtain the variation laws of MS quickly and precisely, a 3-D neural-network hysteresis model of AlNiCo is proposed [40]. Reference [41] proposes a MS estimation control scheme by estimating the initial rotor position. A closed-loop MS control method to

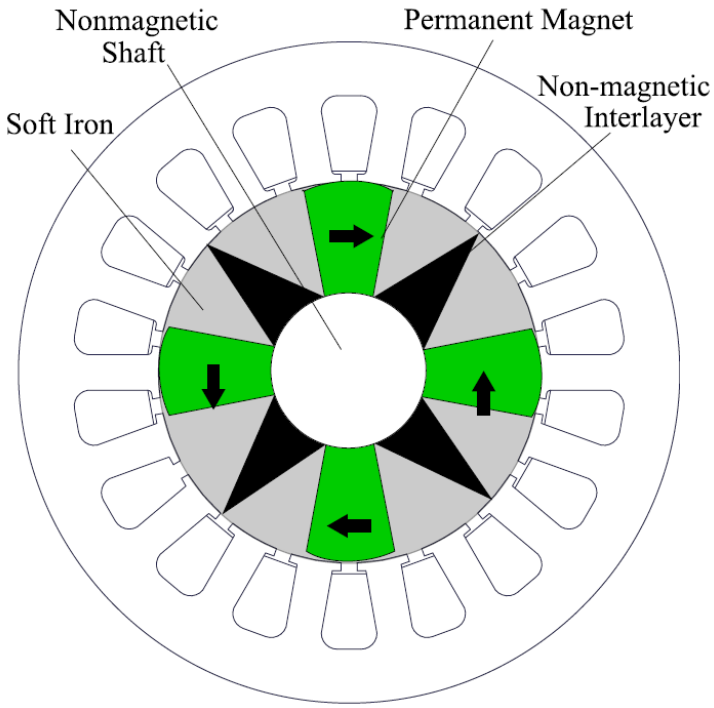

Fig.1-2 Cross-section of a VF-PMSM with single PM material [3].

enable reliable loss minimization control of VF-PMSMs is proposed [42]. The MS is estimated at every sample instant and is used as feedback for the closed-loop control.

Control and the MS change is implemented at zero speed, zero load condition by using a voltage disturbance state filter to correct the estimates from a flux observer to avoid the pulsating torque during MS change [43]. The pulsating torque ripple is minimized. However, this work does not investigate the voltage limitations and the MS manipulation is established only at low speeds. The MS is a percentage of the magnet flux linkage to the total magnet flux linkage that could be produced. The MS should be properly selected according to different working conditions, for instance, high MS at high torque requirement and low MS at high speed requirement [24].

The artificial neural network-based MTPA control scheme is implemented for the spoke-type flux intensified VF-PMSM in [12]. With this control method, the control effort

is significantly simplified by reducing the effect of the inductance nonlinearity under MS control.

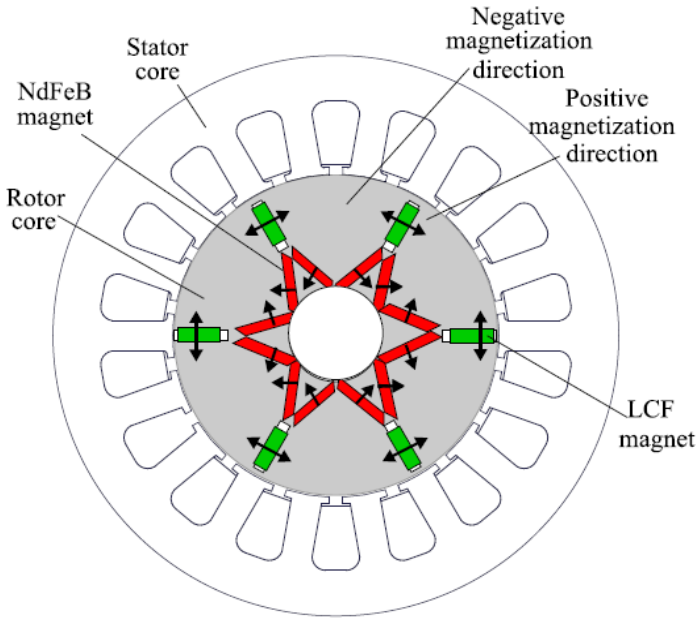

Fig.1-3 (a) Cross-section of a VF-PMSM with Parallel hybrid PM material [43].

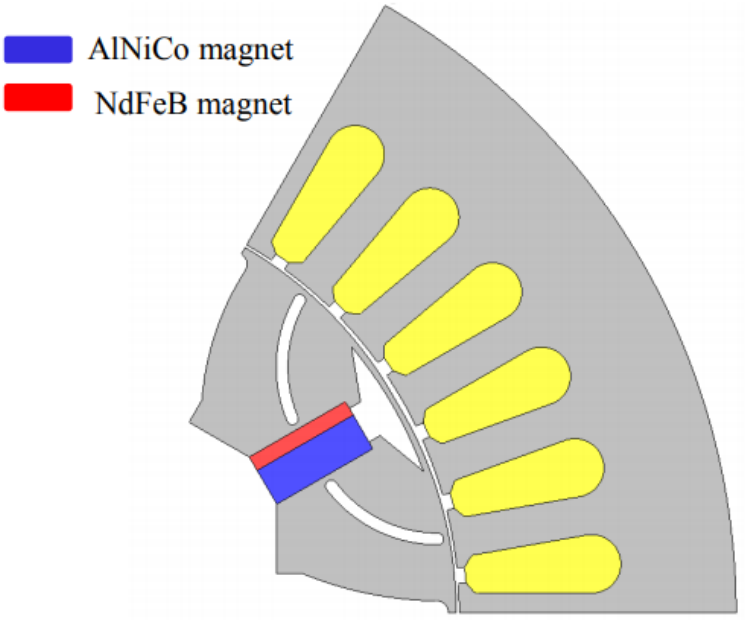

Fig.1-4 (a) Cross-section of a VF-PMSM with Series hybrid PM material [44].

1.3.2 Hybrid PM VF-PMSM

The unintentional de-magnetization of the LCF PM occurs especially under loaded conditions due to the cross-coupling effect. Therefore, various improved hybrid-PM structures have been proposed and investigated.

1.3.2.1 Parallel PM- Hybrid VF-PMSM

In the parallel PM- hybrid VF-PMSM, the main flux through the air gap is the sum of two parallel branches i.e., the sum of constant flux and variable flux. This kind of topologies is investigated in [26], [44]. It is observed that the cross-coupling between the two magnets is high and the LCF PMs tend to get demagnetized by the adjacent high coercive force PM thus making the operating point of the VPMs very unstable.

1.3.2.2 Series PM- Hybrid VF-PMSM

In a series hybrid arrangement, the constant flux always assists the variable flux thereby stabilizing the operating point of the VPM [45], [46]. The complicated rotor flux barriers are avoided in series hybrid VF-PMSM since the LCF working point is inherently stable due to the assistance of constant flux PM. Thus, series PM- Hybrid VF-PMSM can handle high armature and high electrical loading.

1.4 Inverted Saliency VF-PMSM

Regular PMSMs can withstand the unintentional magnet de-magnetizing effect by the armature current because of the high coercivity of the rare-earth magnet. However, the armature de-magnetizing field can cause problems for AlNiCo-based VF-PMSMs because of the low coercivity of AlNiCo magnets. A tangential magnetization method can overcome the armature de-magnetizing effect [47]. Fig.1-5 and Fig.1-6 show the rotor topology and the $dq-axes$ flux path. In this design, two sets of barriers are curved to prevent the $q-axis$ flux from going through the magnet. The top barrier on the magnet minimizes the

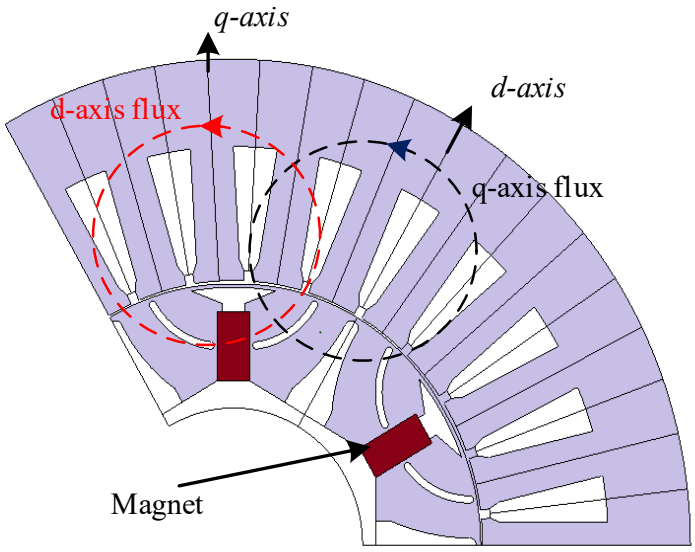

Fig.1-5 Illustration of the $dq-axes$ flux paths for tangential magnetization.

rotating flux in that area. The $d-axis$ flux line passes through the magnet uniformly while the $q-axis$ flux passes along the magnet face instead of going through the magnets as in conventional radial designs. This avoids unintentional de-magnetization by the armature current and facilitates uniform magnetization and de-magnetization.

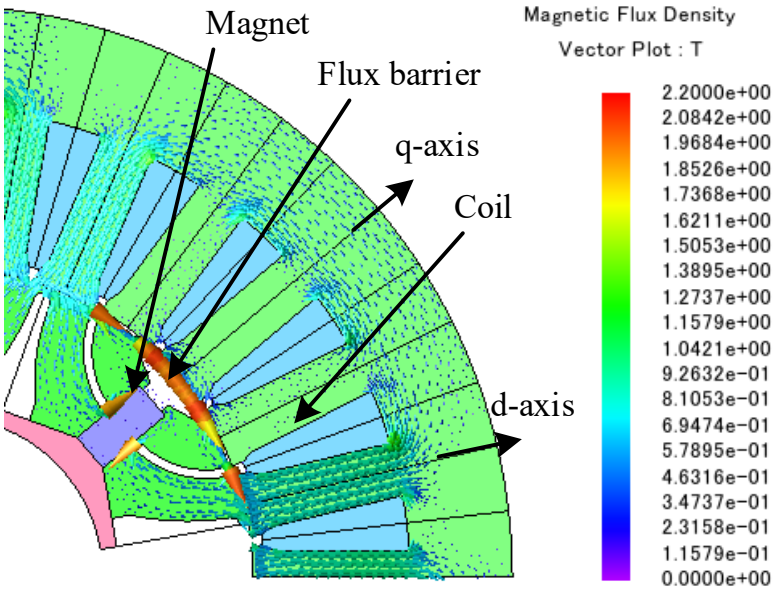

Fig.1-6 FEA simulated $q-axis$ flux density vector plot in the variable flux machine.

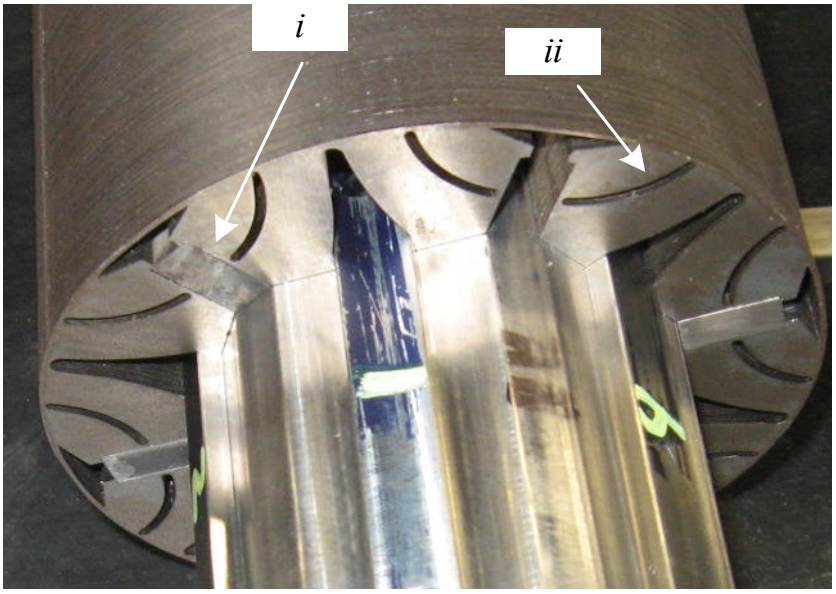

Fig.1-7 (a) Prototyped rotor, i- AlNiCo magnets. ii- Rotor lamination.

This allows the de-magnetization possible just by using the short duration $d-axis$ current pulse. The air gap length is non-uniform to prevent the magnet from unintentional de-magnetization by the armature reaction. Fig.1-7 shows the rotor topology of the prototyped VF-PMSM [11].

1.4.1 VF-PMSM Magnetization state

The dynamics of magnetization and de-magnetization obtained from the finite element analysis (FEA) software are shown in Fig.1-8. Initially, the machine is running at rated speed with no load and is at 100% MS. At time 0.02 s, the VF-PMSM is demagnetized supplying a de-magnetization current pulse. The de-magnetization pulse exposes the magnet to an external magnetic field. Once the de-magnetization pulse is removed, the magnet flux linkage is nearly 0 Wb. Similarly, the re-magnetization pulse is supplied at 0.06 s to extend the magnet flux linkage. In this fashion, the MS of the VF-PMSM can be changed to the specified value by an external magnetic field.

The LCF of the AlNiCo 9 magnet shows a unique feature of magnetization state control in the VF-PMSM. Fig.1-9 shows the B-H loop of the AlNiCo 9 magnet for 100% MS and

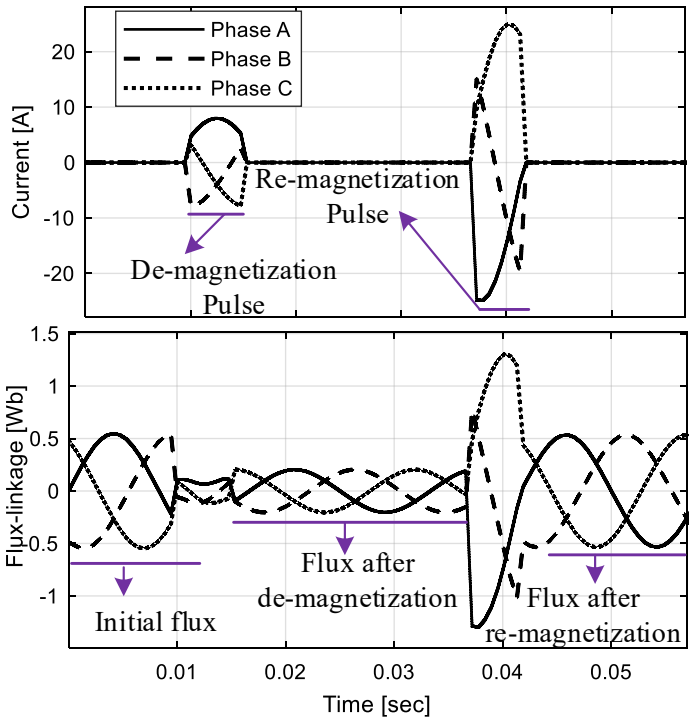

Fig.1-8. FEA simulated three-phase current and magnet flux linkage when de-magnetizing and re-magnetizing pulses are applied.

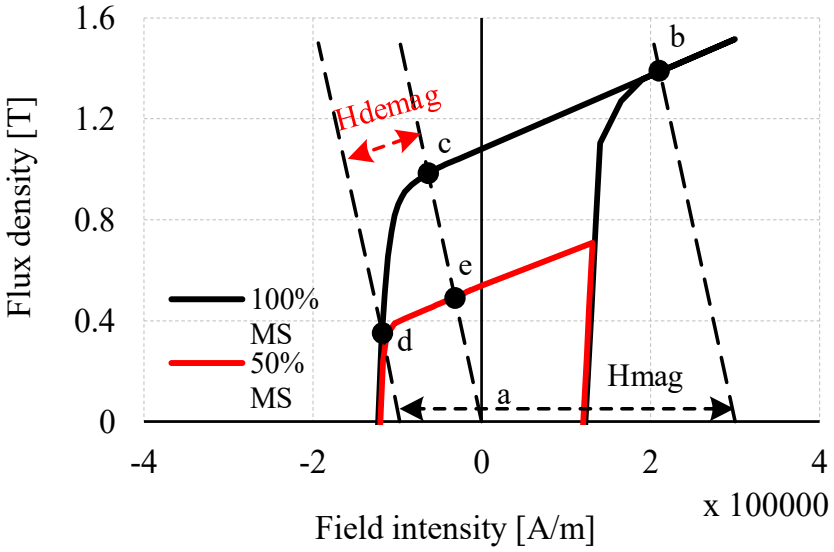

Fig.1-9. B-H loop of AlNiCo 9 for 1 st and 2 nd quadrants.

50% MS in the 1 st and 2 nd quadrants. Initially, the magnet is operating at point c. A de-

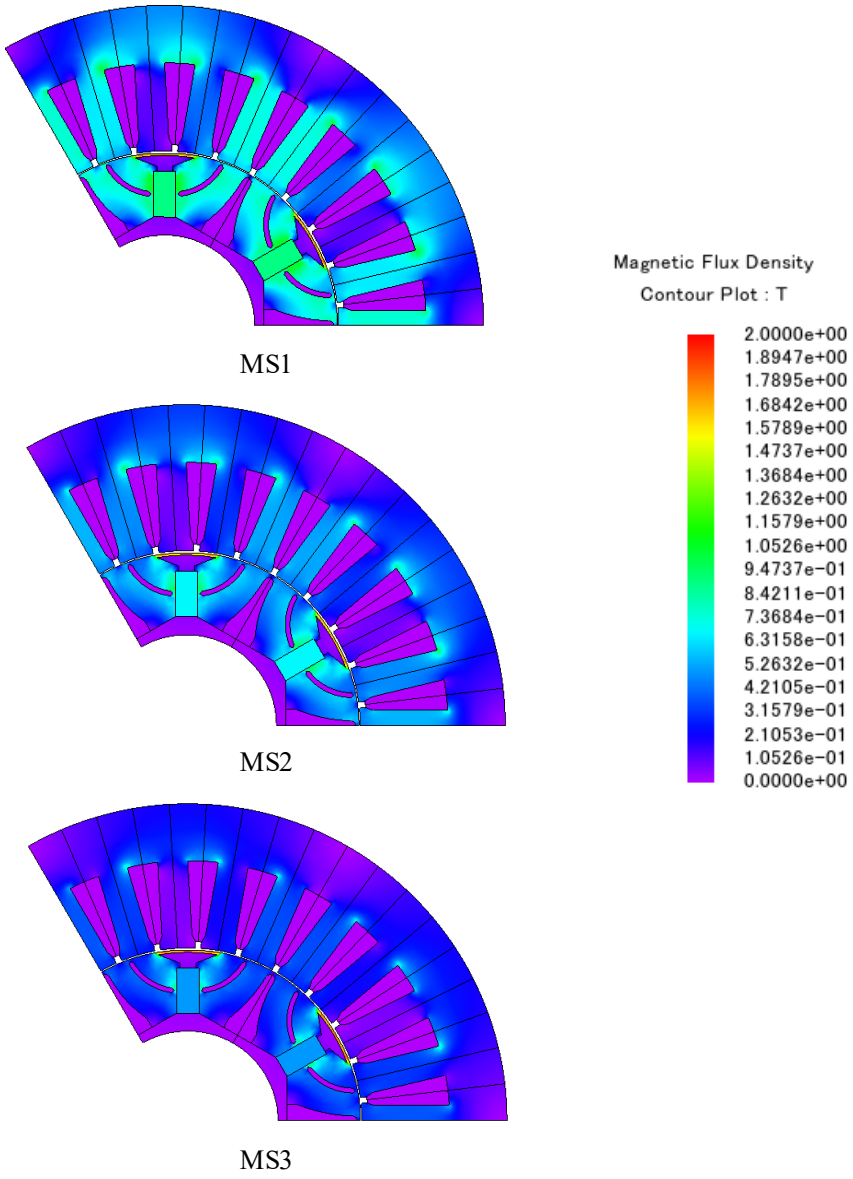

Fig.1-10. Flux distribution of the VF-PMSM at different MSs.

magnetization force of H_{demag} is applied and the operating point is shifted to point d. However, once the de-magnetization force is released the magnet recoils along a new magnetization curve parallel to the original B-H curve. The magnet operating point because of the de-magnetization pulse will be point e instead of point d. This behavior of the magnet can be observed in the FEA simulated de-magnetization or re-magnetization process shown

in Fig.1-8. After the pulse is removed, the magnet flux linkage recoils to the new magnetization level.

The flux distributions of the VF-PMSM at different MSs (100%, 70% and 50%) are shown in Fig.1-10. Since the magnet flux density decreases with the decrease in the MS, the torque also decreases.

Fig.1-11 shows the comparison between the experimentally obtained and FEA obtained relationship between the rotor flux linkage and de-magnetization and re-magnetization current for the prototyped machine. Because of the LCF magnet, a small change in current can change the MS significantly [48], [49]. It can be seen that the negative 10.8 A $d-axis$ current pulse exposes the magnet to a 100% de-magnetization state. However, the re-

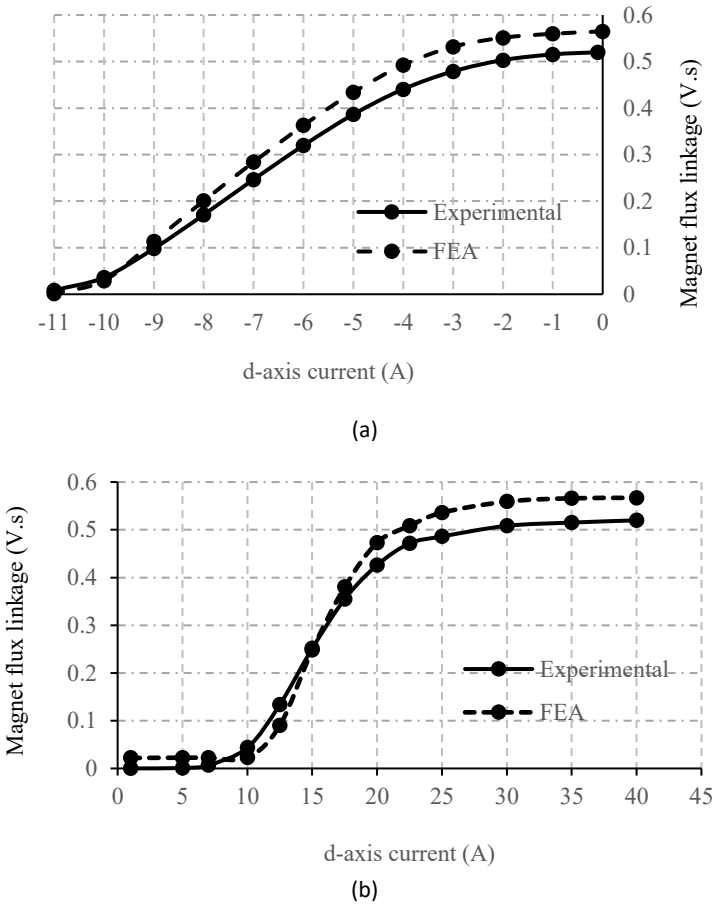

Fig.1-11. (a) de-magnetization curve (b) re-magnetization curve of the VF-PMSM.

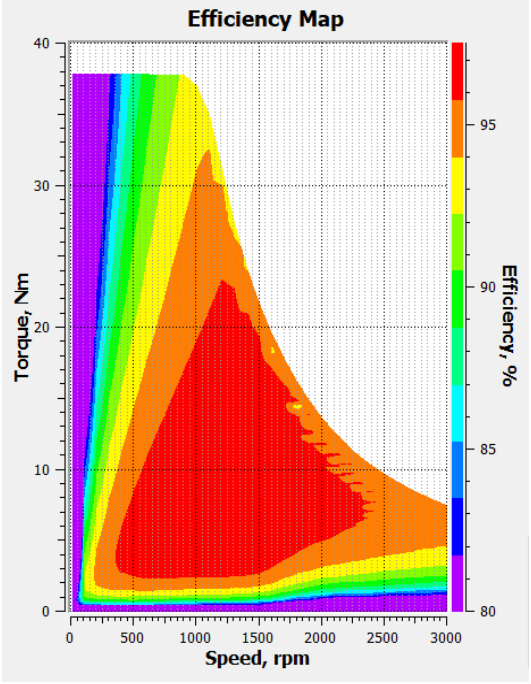

(a)

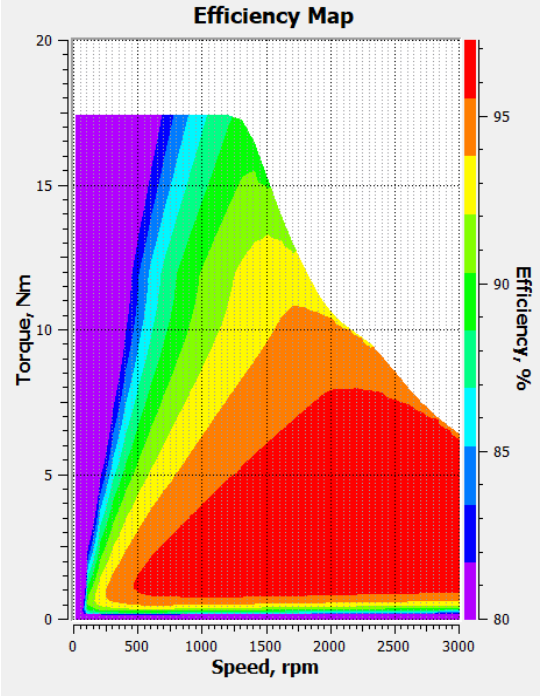

(b)

Fig.1-12. Efficiency map for different MSs (a) 100% MS (b) 50% MS.

magnetization current requirement is much higher than the de-magnetization current. It is found that 2.8 per unit current is required to expose the magnet to 100% MS.

Fig.1-12 shows the efficiency map for different MSs. As the MS decreases, the maximum efficiency shifts to a higher speed region. Besides, the base speed is also extended as the MS decreases.

1.4.2 Temperature Effects on AlNiCo magnets

Alnico magnets offer outstanding temperature stability. The output performance from AlNiCo magnets varies the least with temperature changes, making it an ideal choice for temperature-sensitive applications.

The loss through high temperature in Alnico may only be up to 5% but very high temperatures (over 530 ℃) may start to permanently alter the metallurgical structure which would cause a significant permanent and irreversible drop in output.

Most magnets perform better when the temperature drops. That's because the atoms that comprise magnets vibrate more slowly and less randomly when cold. The result is a better alignment of the atoms that generate the magnetic field, boosting its strength [50]. For AlNiCo magnets, -75 ℃ is regarded as a reasonably acceptable lower temperature although irreversible losses of around 10% are reported at -190 ℃. However, the actual losses are a function of the magnet geometry, total magnetic circuit and the BH curve shape [51]. This makes the AlNiCo based EV a preferable option for cold weather.

1.4.3 Design Specifications and Dimensions

All the simulations, FEA analysis and experiments throughout this thesis are performed in a single VF-PMSM designed by M. Ibrahim [11].

The designed VF-PMSM is a 6-pole, 27-slot machine. The general dimensions are given in Table 1-1.

Table 1-1 The VF-PMSM dimensions

Magnet length	14.2 mm
Magnet thickness	7 mm
Rotor outer radius	54.5 mm
Air gap length	0.4 mm-0.75 mm
Rotor inner radius	53.75 mm-54.1 mm
Stack length	120 mm

1.5 Minimum Inverter Rating

Usually, the magnetizing pulse current required to magnetize the magnet 100% is larger than the machine-rated current. The inverter rating should be high enough to handle the surge current even though the pulse current is of a few milliseconds. This leads to an oversized inverter. Thus, minimum inverter sizing as small as possible and large enough to magnetize the machine at no-load and full load must be determined.

The VFM used in this study has a current rating of 10A and requires 2.1 p.u. current for a minimum of 10 ms to achieve 100% MS. To find the minimum inverter rating to supply sufficient magnetization, industrial 3-phase inverter packs (Semikron SKiiP 04AC066V1 and Semikron SKiiP 14NAB066V1) are considered. Generally, the industrial inverter can endure a surge current of twice the nominal current for 1 ms. The surge current varies depending upon the inverter's heat sink and external cooling. However, the device's safe operating area and transient thermal impedance must be considered for a duration other than 1ms. The conduction and switching loss (loss due to device switching for t=10 ms) is calculated.

Two cases have been considered to study the inverter sizing for VFM: magnetizing current only and magnetizing current at full load. In the first case, only the magnetizing current (30 A) is considered. In the second case, the motor current and the magnetizing current (33 A) are considered. Considering the worst case, a 30 A pulse for 10 ms will raise

the device junction temperature by 25°C. This is within the maximum junction temperature limit of 150°C for the Semikron SKiiP 14NAB066V1 and limit of 150°C for the Semikron SKiiP 04AC066V1. This shows that the IGBT inverter of rating 21 A at T_s=70°C and peak current of 40 A for 1ms can fully magnetize the VFM, while IGBT inverter of rating 25 A at T_s=70°C and peak current of 40 A for 1ms can fully magnetize the VFM when the motor is running at full load.

Thus, an inverter with 2.1 times the rated machine current will be able to provide the magnetization current and an inverter with 2.5 times the rated machine current will be able to provide the magnetization current when the motor is running at full load. However, since the magnetization current amplitude and width vary depending on the design, this current rating is not true for all VFMs.

1.6 Objectives

The objectives of this thesis are:

- To study the effect of different magnetization pulse widths and methods on the magnetization level, back-EMF and no-load losses of the VF-PMSM.
- To study the quality of the back-EMF for different speeds and different MSs.
- To study the machine no-load losses due to different magnetizing current pulse widths for different MSs.
- To study the effect of de-magnetization and re-magnetization pulse on the machine torque.
- To develop an algorithm to minimize the pulsating torque during the magnetization process.
- To investigate the parameter variation of VF-PMSM for different MSs.
- To develop a drive system for VF-PMSM in a co-simulation platform and to study the effect of the PWM inverter on machine losses.

1.7 Limitations

The limitations of the thesis are:

- A lookup table-based method is used to estimate the MS due to the unavailability of flux transducers and the difficulty associated with their placement inside the motor due to the limited space.
- Due to the unavailability of a high bandwidth torque transducer, it is difficult to observe the pulsating effect in the experiment.
- DC bus voltage available in battery-powered EVs is limited. However, a constant 400V DC bus is considered during the experiment to reduce the pulsating torque.

1.8 Thesis Outline

This thesis proceeds as follows.

Chapter 2: This chapter presents the operating point trajectory for different MSs. The VF-PMSM drive system that can estimate the back-EMF during the motoring mode has been explained. An adaptive nonlinear filter has been adopted to extract the desired harmonics from the distorted back-EMF signal. The operating principle of the VF-PMSM and the effect of different MSs on the rotor speed has been explained by the experimental results. The process of achieving the desired MS has been explained. The minimum magnetizing pulse width to magnetize the VF-PMSM 100% is experimentally determined. The machine no-load losses are discussed for different magnetization pulse widths and speeds.

Chapter 3: This chapter presents an algorithm to reduce the torque pulsation in VF-PMSM during the magnetization process. Since the magnitude of the magnetizing current can be much higher than the machine rated current, an undesired torque is produced if the i_q current is kept constant during the MS change. To achieve smooth torque performance during the MS change, the $q-axis$ current reference during the re-magnetization period is determined by two different methods: the voltage limit method and the load torque method.

Chapter 4: For accurate control and efficiency optimization, an accurate estimation/ measurement of the machine parameters is inevitable. The VF-PMSMs have different MSs

and thus the parameter estimation/measurement is of prime importance for proper control. A current control-based method is used to measure flux linkage, inductance and resistance for the VF-PMSM at different MSs. Automated real-time parameter measurements are performed without requiring offline post-processing.

Chapter 5: This chapter presents an electric vehicle motor drive system and loss analysis due to pulse-width modulation (PWM) inverter drive for a VF-PMSM using a co-simulation platform. A pair of software tools: finite element method (FEM) based software, which allows computing the electromagnetic behavior and MATLAB, which allows the dynamic simulation of the control circuit and power converters are coupled to develop the VF-PMSM drive. Such an integrative simulation approach gives higher fidelity results since it includes magnetic saturation (inductance nonlinearities), machine geometry (torque ripple and spatial harmonics) effects. Besides, the comparative effect of the sinusoidal current and PWM inverter fed VF-PMSM's losses have been studied. The PWM inverter superimposes carrier harmonics in the basic current waveform and applies a high-frequency magnetic field to the motor. As a result, the iron loss is generated in the rotor and stator of the motor. Since an additional loss due to the PWM inverter has to be considered in high-efficiency motors in the design phase, the impact of different switching frequencies on motor loss, terminal current and torque ripple are investigated. The co-simulation results are validated with conventional simulation (dq-mathematical model), FEM and experimental results.

Chapter 6: This chapter presents the thesis conclusions and future works.

1.9 Contributions

The achieved contributions in this Ph.D. work are as follows.

In chapter 2, an adaptive nonlinear filter has been adopted to estimate the back-EMF during the motoring mode. The effect of different magnetization pulse widths and magnetization methods on the back-EMF is analyzed for different MSs. The effect of different MSs on the rotor speed has been explained by the experimental results. This work was presented at the 45th Annual Conference of the IEEE Industrial Electronics Society,

Lisbon, Portugal. The extended version of the paper was published in IEEE Transactions on Industrial Electronics.

B. Basnet, A. M. Aljehaimi and P. Pillay, "Effect of Magnetization Pulse Width on the Back EMF of a Variable Flux Machine and on Inverter Sizing," *IECON 2019 - 45th Annual Conference of the IEEE Industrial Electronics Society*, Lisbon, Portugal, 2019, pp. 1028-1033, doi: 10.1109/IECON.2019.8927414.

B. Basnet, A. M. Aljehaimi and P. Pillay, "Back EMF Analysis of a Variable Flux Machine for Different Magnetization States," in *IEEE Transactions on Industrial Electronics*, Sept 2020, doi: 10.1109/TIE.2020.3026281.

In chapter 3, an algorithm to reduce the torque pulsation during the VF-PMSM magnetization is proposed. To achieve smooth torque performance during the MS change, the $q-axis$ current reference is controlled. This research work has been submitted to the IEEE Journal of Emerging and Selected Topics in Power Electronics.

B. Basnet and P. Pillay, "Torque Pulsation Reduction During Magnetization in Variable Flux Machines," *IEEE Journal of Emerging and Selected Topics in Power Electronics* (Under review).

In chapter 4, a current control-based method is presented to measure flux linkage, inductance and resistance for the VF-PMSM at different MSs. The automated machine parameters are generated in real-time without requiring offline post-processing. The research work has been submitted to the 13th annual IEEE Energy Conversion Congress and Exposition (ECCE 2019) and is waiting for the reviewers' decision.

B. Basnet and P. Pillay, " Automatic Flux Linkage and Inductance measurement for a Variable Flux Machine at the Different Magnetization States," *IEEE Energy Conversion Conference & Congress (ECCE)*, Vancouver, Canada, 2021.

In chapter 5, the VF-PMSM drive system in the co-simulation platform is presented. The effect of sinusoidal current and PWM inverter-fed VF-PMSM's losses have been studied. This work was presented at the 2020 IEEE Transportation Electrification

Conference & Expo, Chicago, IL, USA. The extended version of the paper is ready to submit in IEEE Transactions on Transportation Electrification.

B. Basnet and P. Pillay, "Co-simulation Based Electric Vehicle Drive for a Variable Flux Machine," *2020 IEEE Transportation Electrification Conference & Expo (ITEC)*, Chicago, IL, USA, 2020, pp. 1133-1138, doi: 10.1109/ITEC48692.2020.9161605.

B. Basnet and P. Pillay, " Co-simulation Based Electric Vehicle Drive and PWM Loss Analysis for a Variable Flux-Permanent Magnet Synchronous Machine," *IEEE Transactions on Transportation Electrification* (Prepared for submission).

Chapter 2. Effect of Pulse Widths and Magnetization Methods on the Back-EMF And Loss of a VFM

2.1 Introduction

The back electromotive force (EMF) waveform is an important characteristic of electrical machines [52]. Machine designers always pay attention to this, as non-sinusoidal back-EMF waveforms may introduce torque ripple, harmonic currents and increase inverter capacity [53], [54]. Intensive study on the back-EMF analysis has been performed for different motors such as PMSMs [55], [56], [57], [58], and PM BLDC motors [59], [60]. Meanwhile, some VF-PMSMs have a non-uniform air gap to reduce unintentional de-magnetization by armature reaction and to reduce the magnetizing current. This special design will induce spatial harmonics in the machine back-EMF [61]. Moreover, a sudden magnetization current pulse of magnitude 1 p.u. to 3 p.u. will introduce additional harmonics in the back-EMF at different magnetization levels.

In this chapter, the operating point trajectory for the VF-PMSM is presented for different MSs. The drive system that can estimate the back-EMF during the motoring mode has been explained. An adaptive nonlinear filter has been adopted to extract the desired harmonics from the distorted back-EMF signal. The operating principle of the VF-PMSM and the effect of different MSs on the rotor speed has been explained by experimental results. The VF-PMSM open-circuit voltage is presented when running as a generator and has been compared with the estimated back-EMF when running as a motor for various magnetization levels. The precise MS control is a critical issue. Thus, the process of achieving the desired MS is explained. Besides, the quality of the back-EMF and corresponding harmonics spectrum when magnetized by different pulse widths methods are presented. The minimum magnetizing pulse width to magnetize the VF-PMSM 100% is experimentally determined. During the machine design process, it is very important to analyze the losses. Thus, the machine no-load core loss; separating hysteresis and eddy current losses are discussed for different magnetization pulse widths and speeds. Different possible magnetization methods and their effects on the back-EMF are explained.

2.2 Characteristics of the VF-PMSM

The VF-PMSM dynamics are given as:

$$\begin{bmatrix} v_d \\ v_q \end{bmatrix} = \begin{bmatrix} R_s & 0 \\ 0 & R_s \end{bmatrix} \begin{bmatrix} i_d \\ i_q \end{bmatrix} + \begin{bmatrix} 0 & -\omega L_q \\ \omega L_d & 0 \end{bmatrix} \begin{bmatrix} i_d \\ i_q \end{bmatrix} + \omega \begin{bmatrix} 0 \\ \lambda_m(i_d) \end{bmatrix} \tag{2-1}$$

Neglecting the ohmic voltage drops and assuming the steady-state condition,

$$\begin{aligned} v_d &= -\omega L_q i_q \\ v_q &= \omega L_d i_d + \omega \lambda_m(i_d) \end{aligned} \tag{2-2}$$

The inverter has to deliver the continuous rated motor current i_s. The terminal voltage limit, v_s is decided by the maximum available voltage from the inverter. Therefore, the voltage limit and the current limit are given as

$$\begin{aligned} v_d^2 + v_q^2 &\leq v_s^2 \\ i_d^2 + i_q^2 &\leq i_s^2 \end{aligned} \tag{2-3}$$

The voltage ellipse is given by [62], [63].

$$\left(\omega L_q i_q\right)^2 + \left(\omega L_d i_d + \omega \lambda_m(i_d)\right)^2 = v_s^2 \tag{2-4}$$

For the given i_d, the corresponding i_q is plotted to generate the voltage ellipse. Equation (2-4) generates a voltage ellipse in a dq plane for any speed. A family of progressively smaller ellipses is produced with an increase in speed.

The operating trajectory for the VF-PMSM in the (i_d, i_q) plane is shown in Fig.2-1. A comparison has been made with the same rating, design, and saliency ratio PMSM motor. The operating point trajectories for the PMSM and VF-PMSM as the speed increases are 0acd and 0abe respectively. A maximum torque per ampere (MTPA) trajectory for both motors is the same. However, beyond the rated speed and in the 2^{nd} quadrant, the rare-earth magnet needs a higher magnetic force than the AlNiCo magnet for the same level of magnet de-magnetization. As seen in Fig.2-1, a higher amount of de-magnetizing current (point d)

is required for the PMSM while a lower amount of de-magnetizing current (point e) is required for the VF-PMSM to reach the maximum speed. Fig.2-2 shows the simulated operating point trajectory for the VF-PMSM at different MSs. It is seen that the MTPA changes with change in magnet MSs. However, the voltage limits in Fig.2-1 and Fig.2-2 for the VF-PMSM are semi-ellipses because of the nonlinear relationship of the magnet flux linkage with the $d-axis$ current. Such a nonlinear relation does not exist in normal PMSMs with the rare-earth permanent magnet.

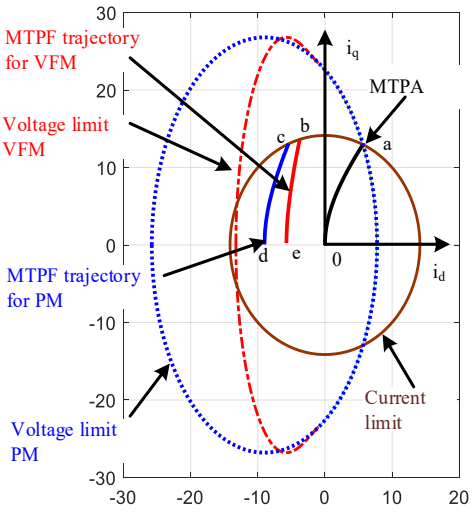

Fig.2-1. Simulated operating point trajectory for VF-PMSM and PMSM.

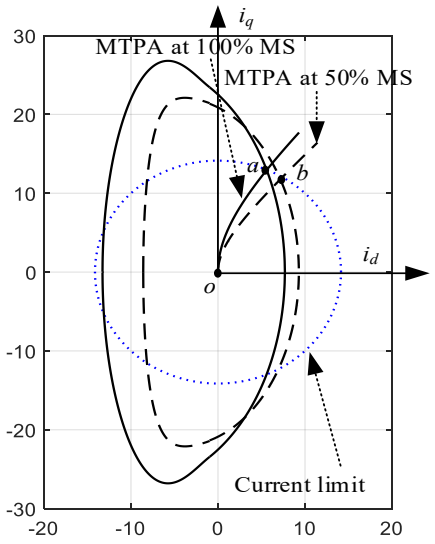

Fig.2-2. Simulated VF-PMSM voltage limit curves at MTPA for different MSs.

2.3 VF-PMSM Drive

Fig.2-3 shows the block diagram of the VF-PMSM drive system. A vector control strategy is used to control the speed and the magnet flux. The VF-PMSM has a different de-magnetizing and re-magnetizing current requirement for different MSs. As a result, magnetization and de-magnetization control should be included in the standard vector control for the PMSM. The vector control operation is constrained by the current and voltage limit that can be supplied by the inverter. When the inverter runs out of voltage, there are two possible ways to reduce the back-EMF. Either by field weakening control or by the magnetization or de-magnetization pulse command [64], [65], [66]. The current pulse method is implemented in this chapter to control the MS. The current pulses are manually controlled based on speed and load requirements by Mag/Demag pulse command block. The

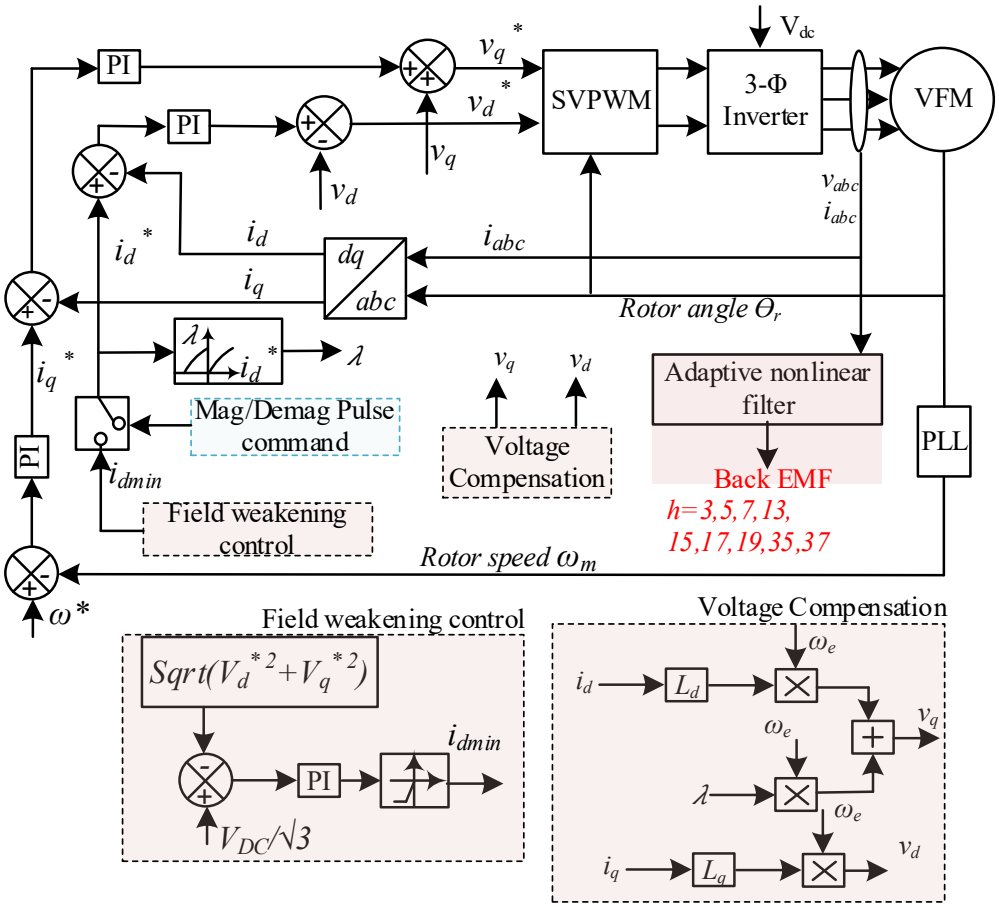

Fig.2-3. Block diagram of the VF-PMSM drive system.

magnet flux can be reduced by injecting a de-magnetization current pulse. Similarly, when high torque is required a magnetization current pulse is injected.

The field weakening control block continuously injects the negative $d-axis$ current [67]. It does not rely on the parameters of the machine but depends on the voltage limit from the inverter. A current limiter is kept at the output of the field weakening controller to limit the maximum negative current that can be allowed to the machine. The voltage compensation block compensates for the voltage generated by the dq-current controller.

The VF-PMSMs are often demagnetized or remagnetized online at the desired MS depending on the driving requirements. However, when the machine is running, the MS cannot be measured and thus has to be estimated. Precise information of the MS is necessary to determine the current to be injected. If the rotor magnet flux is known, the MS can be calculated as (2-14). Several publications have been proposed to estimate the rotor flux for VF-PMSMs and PMSMs [68], [69]. Magnet flux estimation using the back-EMF estimation is one of many approaches. However, some VF-PMSMs rotors are specially designed with uneven air-gap lengths to prevent magnet de-magnetization by the load current and to reduce magnetization current. Thus, harmonics are present in the machine back-EMF and results in non-sinusoidal back-EMF and vary with different MSs.

During the motoring mode, the back-EMF can be calculated by sensing the terminal phase voltage as

$$back\ EMF = v(t) - i(t) * R \tag{2-5}$$

However, the exact back-EMF is difficult to calculate because switching harmonics and device noise are added, resulting in the addition of undesired harmonics. Thus, a proper back-EMF estimation is required to estimate the MS during the motoring mode.

2.4 Adaptive Nonlinear Filter

In order to estimate the harmonics in the back-EMF, an adaptive nonlinear filter is adopted [70].

A distorted back-EMF signal $\mu(t)$ consists of both desirable sinusoidal components and some undesirable components.

$$\mu(t) = y_h(t) + e(t) \tag{2-6}$$

where $e(t)$ is the error (switching harmonics and noise) and $y_h(t)$ is the desired components of interest and is given as

$$y_h(t) = A_h sin(w_h t + \delta_h), \tag{2-7}$$
$$h = 1,3,5,7,15,17,19,35,37$$

Here, A_h, w_h, and δ_h are amplitude, frequency, and phase, respectively. All harmonics, h, given in (2-7), are the desirable harmonics and this information is taken upfront from an offline test. The offline test means running the machine as a generator and analyzing the harmonics present in the machine phase back-EMF.

The gradient descent method minimizes the least square error between the input, $\mu(t)$ and the desired sinusoidal output, $y_h(t)$. The cost function is given as

$$F(t, \theta_h) = [\mu(t) - y_h(t, \theta_h)]^2/2 = [\Delta e(t, \theta_h)]^2/2 \tag{2-8}$$

where θ_h is the vector of parameters used to define the output signal and is given as $\theta_h = [A_h, w_h, \delta_h]$.

The gradient-descent method adjusts the unknown parameter, θ such that the cost function, F tends to its minimum point. The parameter vector $\theta_h(t)$ is estimated using the gradient descent method as

$$\frac{d\theta_h(t)}{dt} = -\mu \frac{\partial[F(t, \theta_h)]}{\partial \theta_h(t)} \tag{2-9}$$

μ is a positive diagonal matrix and controls the algorithm convergence speed and stability of the algorithm. A set of differential equations is obtained following the steps outlined in (2-9). Using vector parameters, the following equations are derived

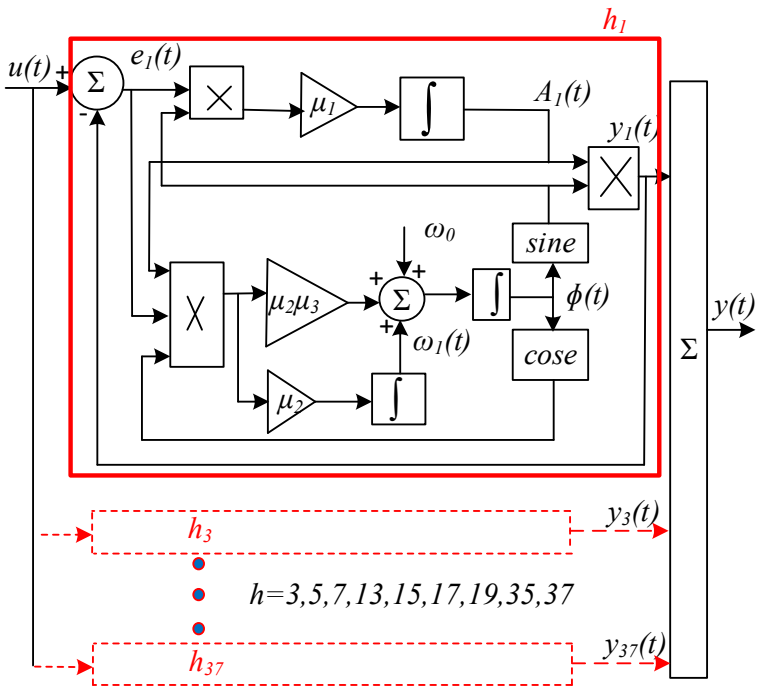

Fig.2-4. Block diagram of the adaptive nonlinear filter.

$$A_h^{\cdot}(t) = \mu_1 e(t) sin\varphi_h(t) \tag{2-10}$$

$$w_h^{\cdot}(t) = \mu_2 e(t)\, A_h(t) cos\varphi_h(t) \tag{2-11}$$

$$\varphi_h^{\cdot}(t) = \mu_3 e(t)\, A_h(t) cos\varphi_h(t) + w_h(t) \tag{2-12}$$

where $\varphi_h = w_h t + \delta_h$, is the total phase. The dot on top of the parameters means differentiation with respect to time. Equations (2-10) - (2-12) form the main unit of the filter.

μ is the step size of the gradient descent method that governs the convergence speed to the solution of the equations (2-10) - (2-12). A small step size results in low steady-state error but very slow convergence speed to the solution. On the other hand, a large step size leads to a quick response with a higher steady-state error. A trade-off, therefore, exists between the transient convergence speed and the steady-state accuracy.

μ_1 is the most sensitive step size in the algorithm and controls the speed of the filter's transient amplitude variations. Small values for μ_1 results in very slow convergence, while,

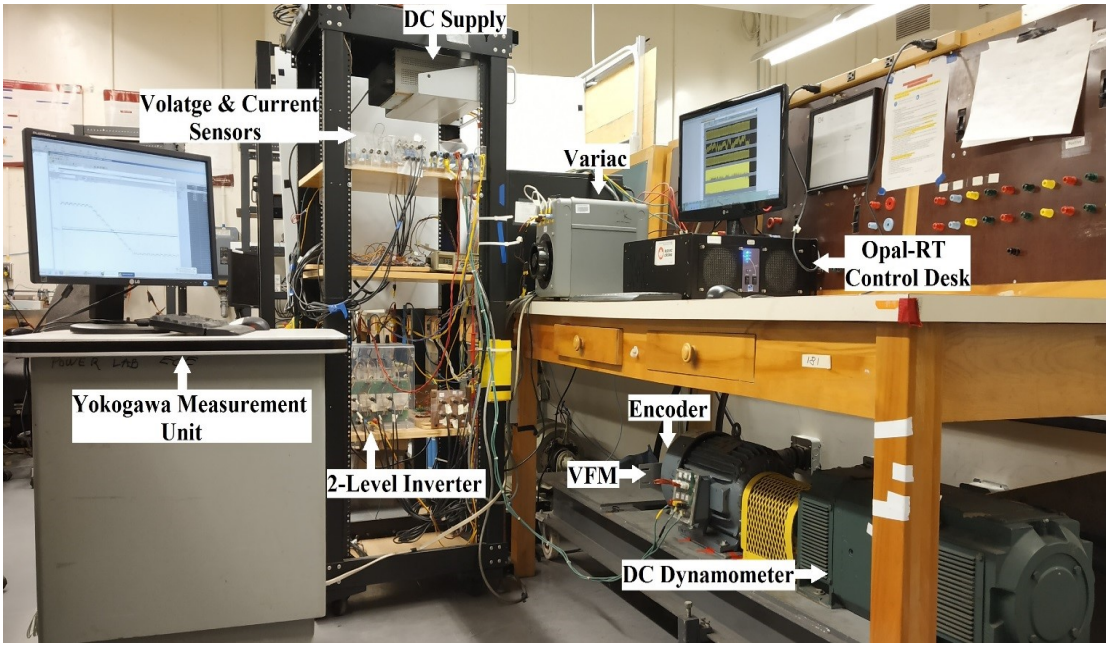

Fig.2-5. Experimental setup.

larger values cause a high steady-state error. μ_2 and μ_3 control the speed of the filter's transient frequency variations.

The structure of the filter is shown in Fig.2-4. A block (inside red solid line) is constructed for each harmonic. Each block gives the amplitude, frequency, and phase of the harmonic order. This filter is then used in an online drive system to estimate the phase back-EMF

2.5 Back-EMF Analysis

The experimental setup is shown in Fig.2-5. The VF-PMSM is driven by a space vector pulse width modulation controlled two-level inverter. The inverter switching frequency is 5 kHz. The rotor position is given by a 12-bit optical encoder that is mounted on the machine shaft. An OPAL-RT is used for real-time control. The VF-PMSM is mounted with a DC dynamometer. The dynamometer has two important roles.

1. To know what order harmonics are present in the VF-PMSM back-EMF. The back-EMF is measured when the VF-PMSM is run as a generator, mounted to a dynamometer.

2. The MS can be calculated from the back-EMF using (2-13) and (2-14) which require the VF-PMSM to run as a generator.

To calculate the MS of the VF-PMSM experimentally, a lookup table is developed between the no-load flux linkage and current pulse. The back-EMF of the VF-PMSM is employed to estimate the flux linkage as

$$\lambda = \frac{\sqrt{2}V_{n,p}}{w_e} = \frac{\sqrt{2}V_{n,p}}{2\pi P \frac{w_m}{60}} \tag{2-13}$$

Then, the MS is calculated as

$$MS\% = \frac{\lambda}{\lambda_f} * 100 \tag{2-14}$$

where λ_f is the flux linkage of the fully magnetized VF-PMSM.

Table 2-1 shows the experimentally calculated MS using (2-14). As the back-EMF decreases, the flux linkage also decreases resulting in a lower MS. For similar speed, the back-EMF reduces from 33.07 V to 19.82 V when the MS reduces from 96% to 48%. The reduction in the magnet flux linkage will reduce the torque output. Thus, above the base speed, the magnet flux linkage decreases nonlinearly.

The dynamics of de-magnetization and re-magnetization are shown in Fig.2-6. Initially, the machine is running at medium speed and is at 100% MS. However, as the speed increases

Table 2-1 Measured speed, phase voltage, flux linkage and MS for the VF-PMSM.

Speed [rpm]	**Phase voltage [V]**	**Flux linkage [Wb]**	**MS [%]**
351.65	33.07	0.5	96.19
313.37	30.94	0.44	84.64
345.39	30.34	0.39	75.02
359.32	19.82	0.24	47.88

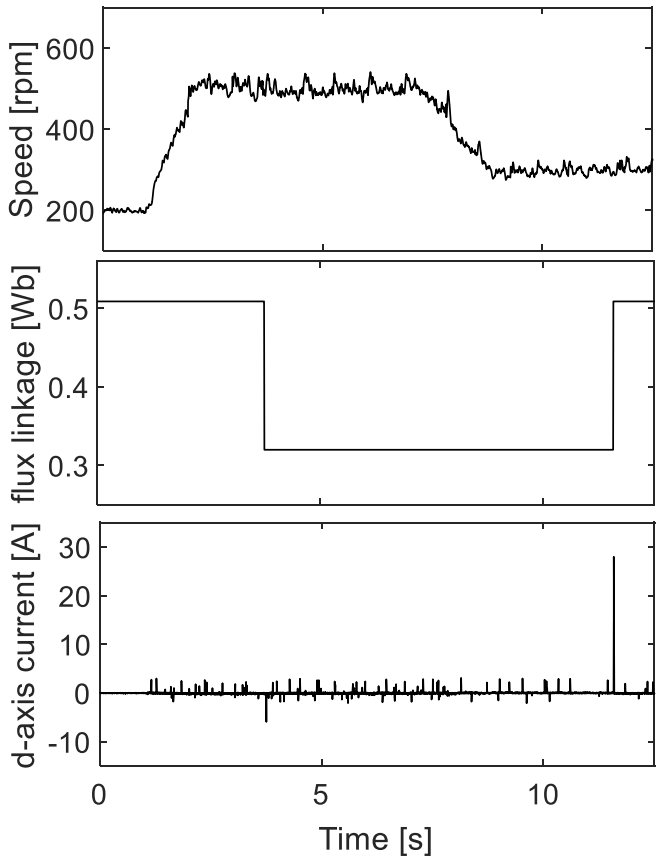

Fig.2-6. Operating principle of the VF-PMSM.

and exceeds the rated/ base speed, the terminal voltage tends to violate the dc-link voltage limits. Thus, a de-magnetization current pulse is introduced. At low speed, the magnet is remagnetized to increase the magnet flux. Usually, the magnetization current is much higher than the de-magnetization current. In these ways the machine can be magnetized/demagnetized online at the desired MS depending on the driving requirements. During the experiment, the MS of the VF-PMSM can be changed by the Mag/Demag pulse command block shown in Fig.2-3.

The zoomed view during the de-magnetization process is shown in Fig.2-7. Rotor angle, $d-axis$ current, $q-axis$ current and estimated back-EMF are shown. During the de-magnetization, the $q-axis$ current rises to maintain the speed reference. Moreover, due to the de-magnetizing pulse, the MS decreases, and thus the magnitude of the back-EMF also

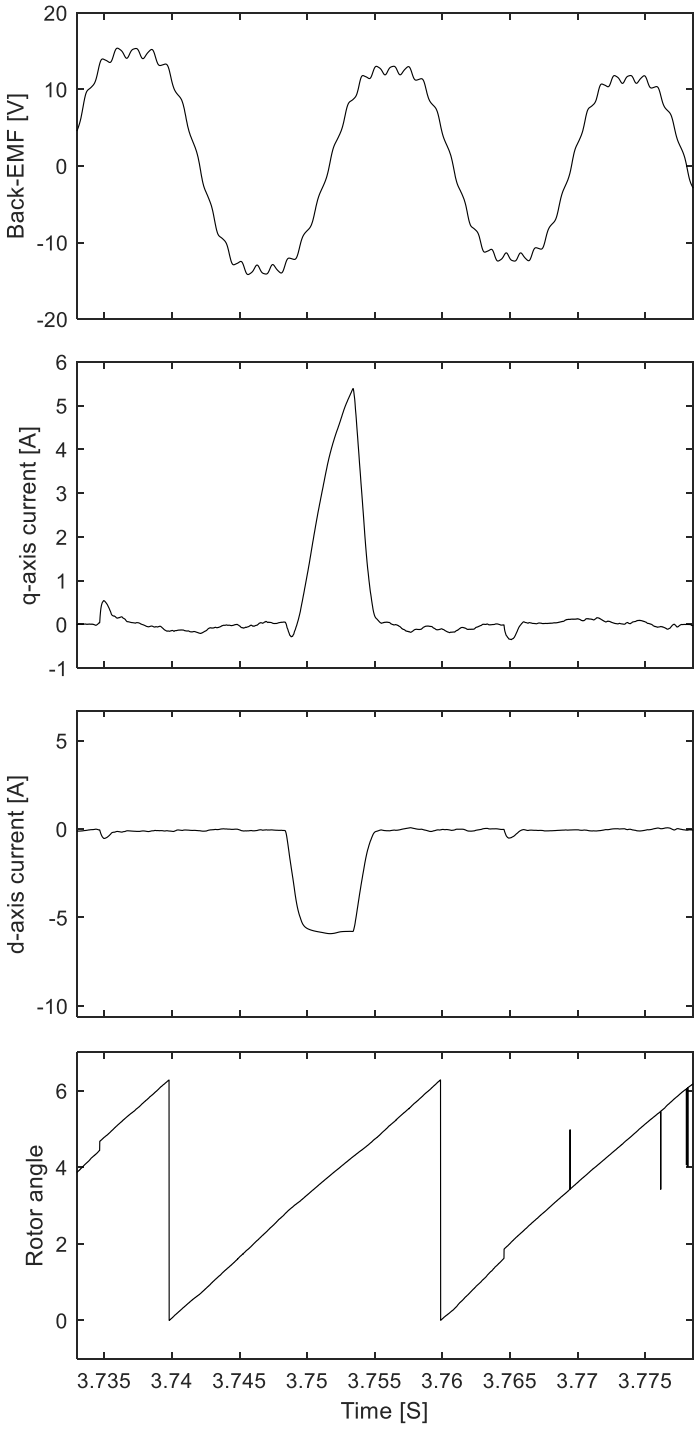

Fig.2-7. Zoomed view showing the de-magnetization of the VF-PMSM.

decreases. However, it is observed that the rotor position is not affected by the de-magnetization and re-magnetization pulse at the running condition.

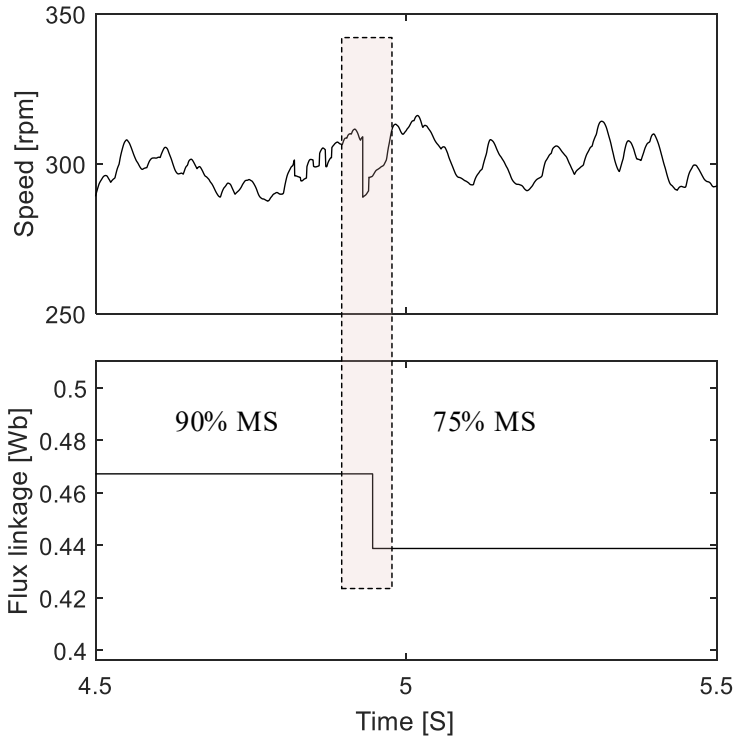

(a)

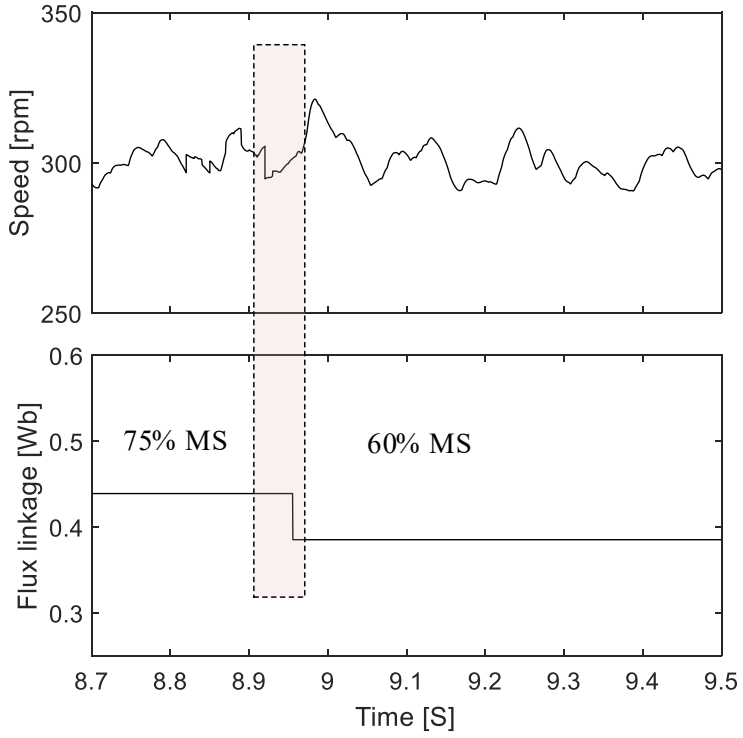

Fig.2-8. Effect of different MSs on the rotor speed.

The effect of change in MS on the rotor speed is shown in Fig.2-8. The results are

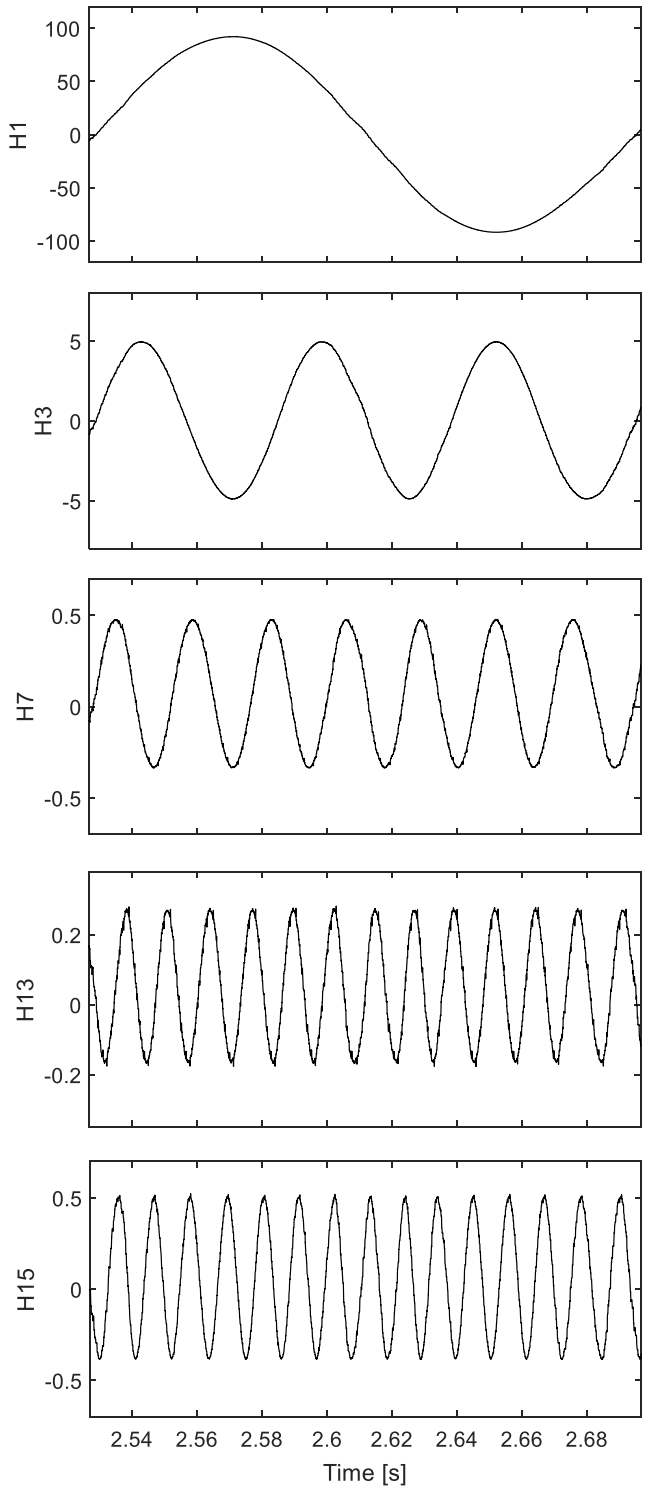

Fig.2-9. Each harmonic component extracted using the adaptive nonlinear filter for 600 rpm at 100% MS.

shown for three different magnetization levels. It is observed that the change in MS will not

have a significant effect on the rotor speed. However, a little speed oscillation is observed for a very short time during the MS change.

Fig.2-9 shows the estimated back-EMF harmonic components when the motor is running at 600 rpm and is at 100% MS. The phase voltage is measured using the OPAL-RT voltage sensor (OP5511) at 50 kHz sampling frequency when the motor is running. The fundamental, $3^{rd}, 7^{th}, 13^{th}, 15^{th}$ order harmonics waveforms are shown. The total back-EMF is generated by the sum of all the desired harmonics.

Fig.2-10 shows one electric cycle of the measured back-EMF at rated speed and its harmonic components for different MSs. The open-circuit voltage is measured when the

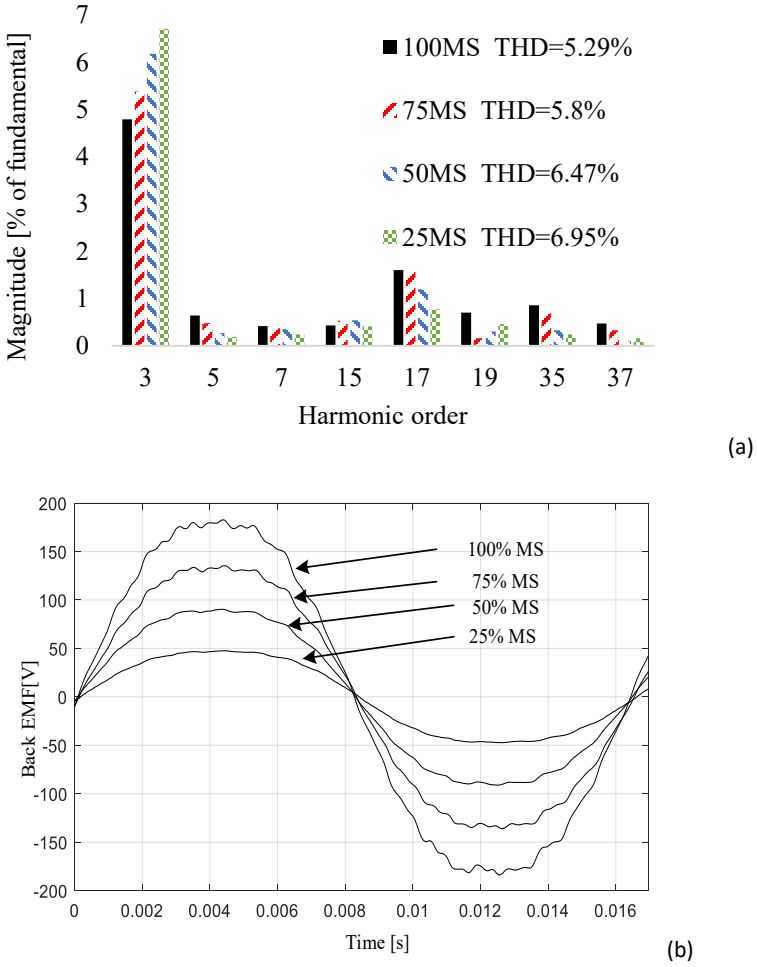

Fig.2-10. Measured one electric cycle at 1200rpm for different MSs (a) Harmonic spectrum. (b) back-EMF waveform.

VF-PMSM is running as a generator at a sampling time of 2e-6s. The differential probe (700924) with 100 MHz bandwidth is connected with Yokogawa (SL1000). Harmonic order like 3,5,7,15,17,19,35,37 are present. The magnitude of the 3^{rd} and 17^{th}order harmonics are high. Although similar harmonics are present, the harmonic magnitudes change with the change in the MS. The 3^{rd} order harmonic decreases with a rise in MS and vice versa for 17^{th} order harmonics. It's seen that the higher the MS the lower the total harmonic distortion (THD).

The THD is given as

$$THD = 100 * \frac{\sqrt{\sum_{h=2}^{N} v_{h,rms}^2}}{v_{1,rms}} \tag{2-15}$$

Although similar order harmonics are present for all the MS, the fundamental decreases with a decrease in the MS. Moreover, the increase in 3^{rd} order harmonic is much higher as the MS is decreased. Thus, the THD increases with a decrease in the MS.

Fig.2-11 shows the normalized electric cycle estimated back-EMF (black) and measured open-circuit voltage (red) for 600 rpm 50% MS. In order to compare with an open-circuit voltage of the machine, the VF-PMSM (without changing the MS) was run as a generator. Fig.2-11 verifies that the adaptive nonlinear filter can track and extract the required harmonic components from the distorted signal.

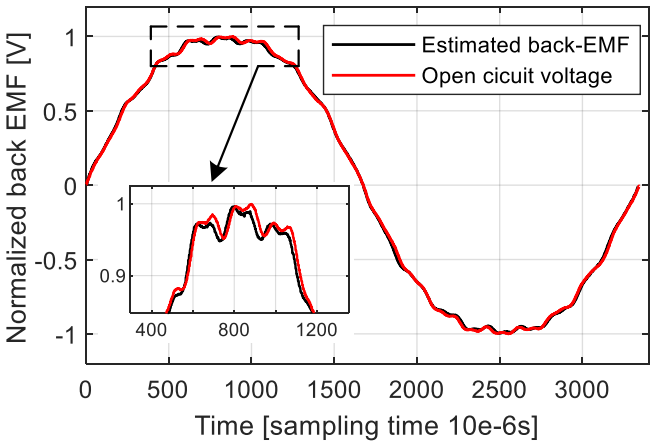

Fig.2-11. One electric cycle of estimated back-EMF (black) and measured open-circuit voltage (red) at 600rpm 50% MS.

2.5.1 Different pulse widths

The de-magnetization and re-magnetization process is explained in Fig.2-12. First, the VF-PMSM is mounted with a DC dynamometer. Since magnet flux is calculated from the phase back-EMF when the VF-PMSM is run as a generator, mounting to a dynamometer is important. Before magnetizing to the required MS, the magnet is completely demagnetized.

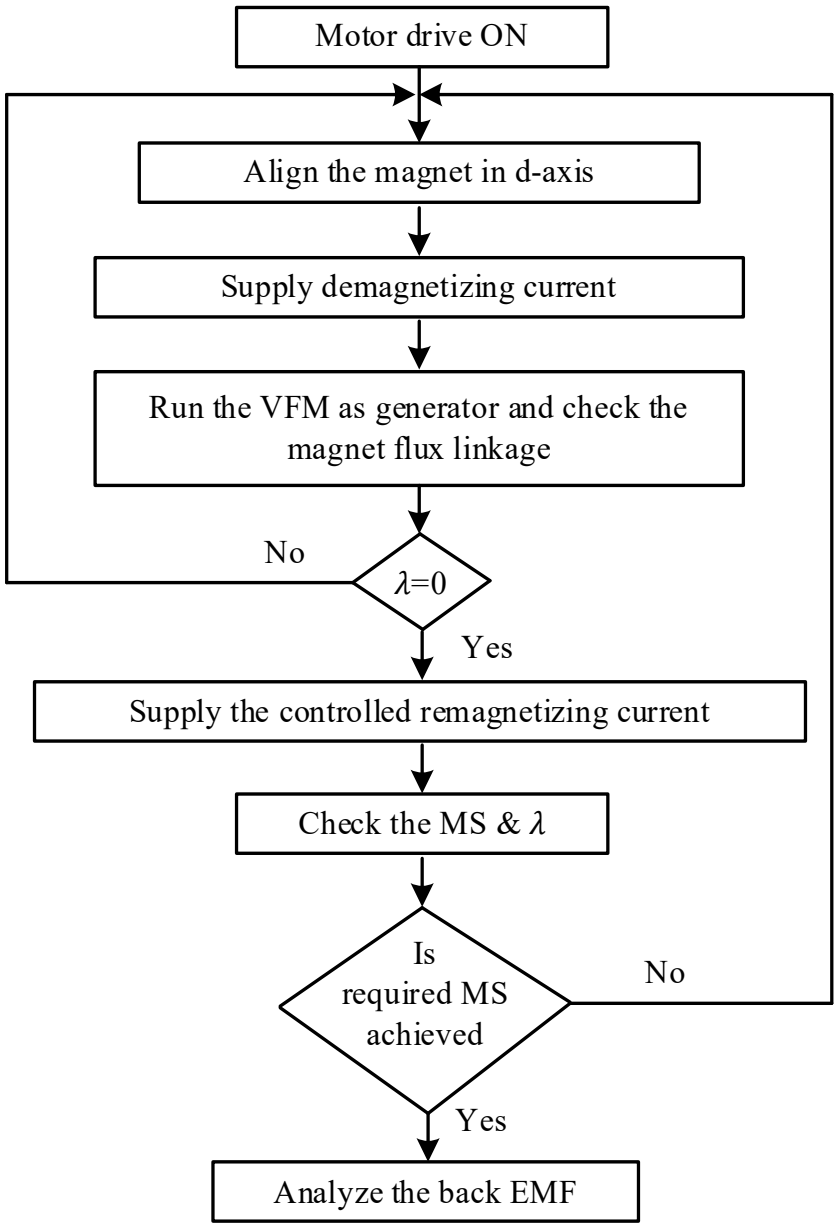

Fig.2-12. Flowchart of the magnetizing process.

Verification is done by checking the magnet flux when the VF-PMSM is run as a generator as per (2-13). If the magnet is not completely demagnetized, the steps are followed again by completely de-magnetizing the magnet. After de-magnetization, the required current pulse is supplied to reach the desired MS. The MS verifications are again done by running the VF-PMSM as a generator. Then the back-EMF is analyzed when the magnet is magnetized with different pulse widths.

The VF-PMSM can be magnetized with different magnetization pulse widths and methods. However, minimum pulse widths to 100% magnetize the machine has to be determined to calculate the optimum inverter rating. The machine MS depends on magnetization pulse amplitude, duration, and available DC bus voltage. The DC bus (400 V) is fixed during the experiment since the DC bus is limited in practical applications.

The back-EMF comparison for various pulse widths varying from 10-50 ms is conducted. Fig.2-13 shows the normalized estimated back-EMF waveforms for various pulse widths when the motor is running at half the rated speed and is at 50% MS. The back-EMF waveforms are very close for all current pulse widths above 10 ms. However, it is seen that the magnet is not 100% magnetized with a pulse width of less than 10 ms. Thus, the minimum current pulse required to fully magnetize the machine was 30A, for 10 ms.

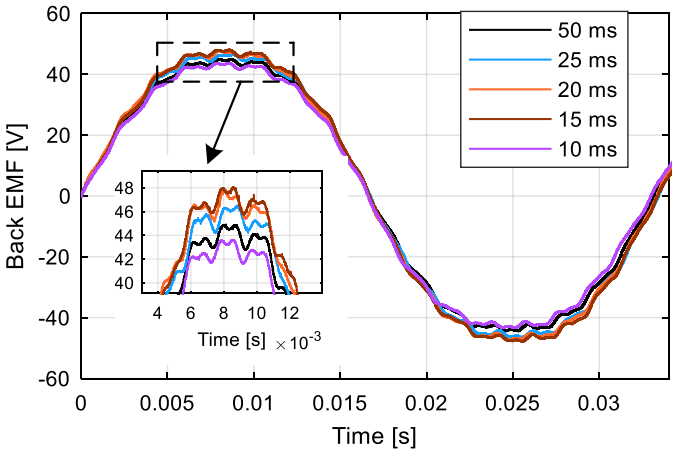

Fig.2-13. One electric cycle of back-EMF for different magnetization pulse widths (600rpm for 50% MS).

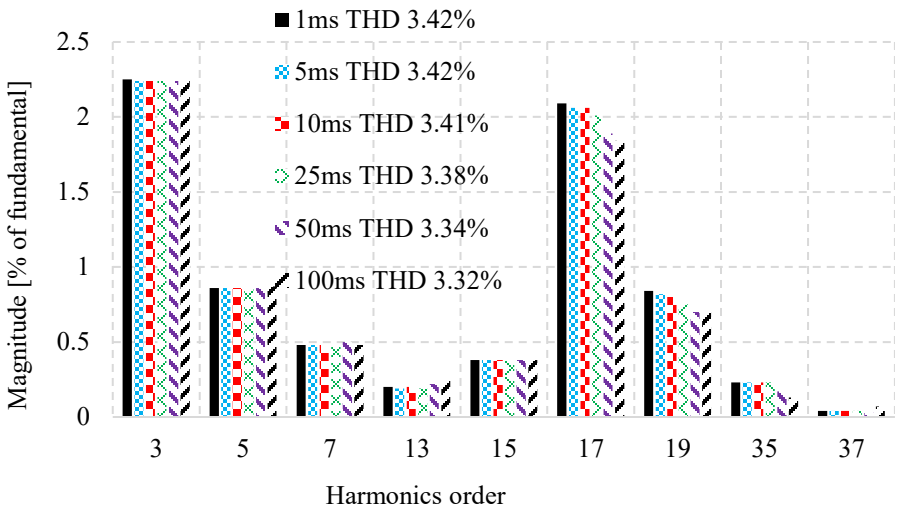

Fig.2-14. Harmonics spectrum of FEA generated back-EMF for different magnetization pulse widths at rated speed.

The harmonic spectrum of the back-EMF from the experiment and FEA are shown in Fig.2-10(a) and Fig.2-14, respectively. Although the same order harmonics are present, harmonic magnitudes are different. This is because the prototyped VF-PMSM has lower slotting effects (tooth harmonics) compared to the FEA design. The higher magnitude in the 17^{th} and 19^{th} order harmonics in the FEA design is due to the higher slotting effect. The slot harmonics depend on the magnitude of the air gap flux. It is seen that the coil flux linkage in FEA is 0.56 weber compared to 0.52 weber in the prototyped machine. The coil flux linkage is the product of the number of turns and flux. Since the number of turns is the same, flux is higher for FEA resulting in higher slot harmonics.

Harmonics order due to slotting are given by

$$Tooth\ harmonics = 3nq \pm 1 \tag{2-16}$$

where n is an integer and q is the number of slots per pole per phase. As per (2-16), the 17^{th} and 19^{th} are the dominating harmonics apart from spatial harmonics (harmonics introduced because of the spatial distribution of flux density) for 27 slots 6 poles machine. In Fig.2-14, the tooth harmonic magnitude decreases with an increase in the magnetization

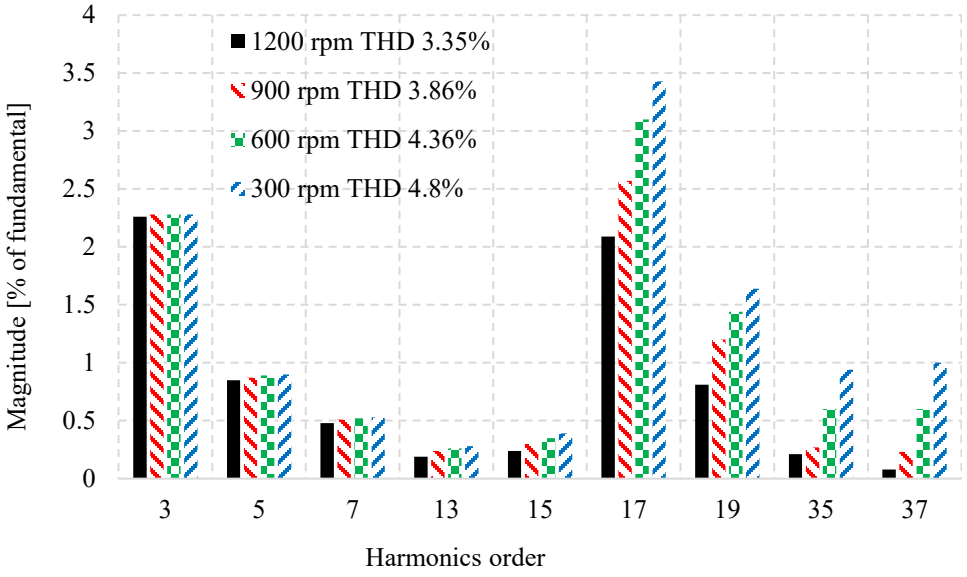

Fig.2-15. Harmonics spectrum of FEA generated back-EMF when magnetized by 10 ms for different speeds.

pulse width. The back-EMF THD decreases to 3.32% from 3.42% for 100 ms and 1 ms, respectively. However, the quality of back-EMF is not only the design consideration factor, but losses due to longer pulse width also have to be considered. Fig.2-15 shows the harmonic spectrum of FEA generated back-EMF when magnetized by 10 ms for different speeds. As the speed decreases the back-EMF quality decreases. A significant increase in the slotting effect is observed as the speed decreases that the back-EMF THD increases from 3.35% to 4.8%.

To study the effect of pulse duration in the magnet, the air gap flux density has to be analyzed. The air gap flux density waveforms for different magnetization pulse widths are shown in Fig.2-16. It is seen that the air gap flux density THD decreases with an increase in pulse width. A 10 ms pulse width has 22.5% THD while 100 ms has 22.2% THD. The flux density vector in the magnet also changes with change in the magnetizing current pulse. It is seen that the magnet flux density is more uniform when magnetized by higher pulse widths.

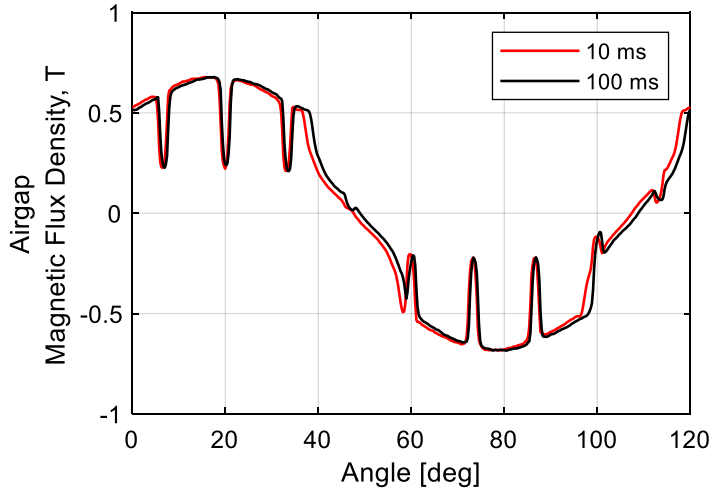

Fig.2-16. One electric cycle of air gap magnetic flux density for different magnetization pulse widths.

2.5.2 Different Magnetization Methods

An intensive study on back-EMF harmonics is performed with different magnetization methods. The VF-PMSM can be magnetized or demagnetized in three different operating conditions: standstill, running and locked rotor conditions.

Standstill and running magnetization methods are performed when the motor drive is online. An online drive means the magnetizing current pulse is supplied through a controlled inverter. The rotor position must be known while magnetizing/de-magnetizing online, and the $d-axis$ current has to be injected in the rotor $d-axis$. In the standstill magnetization method, a current pulse is supplied through the drive to the motor terminal at zero rotor speed. In the running magnetization method, the $d-axis$ current pulse is supplied when the motor is running, regardless of the rotor speed. This is a good approach to magnetize or demagnetize the VF-PMSM in terms of application, such as an electric vehicle since it provides the flexibility to vary the motor MS regardless of the speed.

The locked rotor method is a DC method. In this method, before supplying the $d-axis$ current pulse, the rotor is locked in the $d-axis$. Injecting a positive current pulse to motor phase A with shorted phases B and C will lock the rotor at the $d-axis$. This can be a

Table 2-2 Estimated back EMF harmonic spectrum for different magnetization methods

		Running	**Locked**	**Standstill**
Fundamental Frequency (Hz)		30.03	29.29	29.9
Fundamental Amplitude (V)		48.22	49.22	48.77
3rd	% of fundamental magnitude	5.68%	4.44%	5.55%
17th		1.59%	1.5%	1.84%

redundant process because each time the rotor should be locked and unlocked to check the motor MS.

Table 2-2 shows the harmonic spectrum for different magnetization methods when magnetized by a 25ms pulse width. Although other harmonic orders are also affected by magnetization methods, only the 3^{rd} and 17^{th} order harmonics are mentioned. The 3^{rd} and 17^{th} order harmonics magnitude is less in the locked rotor method resulting in a lower back-EMF THD.

2.6 Losses in the machine

Loss measurement is an important factor in a machine design process [71], [72]. The dissipated energy by the magnetizing pulse current depends on the current pulse width, i.e, 35 J for 10 ms and 175 J for 50 ms. Thus, the magnetizing pulse width must be as low as possible in terms of Joule loss.

Apart from the copper loss, core loss is an important factor in the high-efficiency motor design. If the core loss is high, the temperature rises and there is a higher probability that the material will lose its property. If an accurate prediction of core loss is done for different magnetizing pulse widths, then a model with a reduced magnetizing pulse width can be modeled.

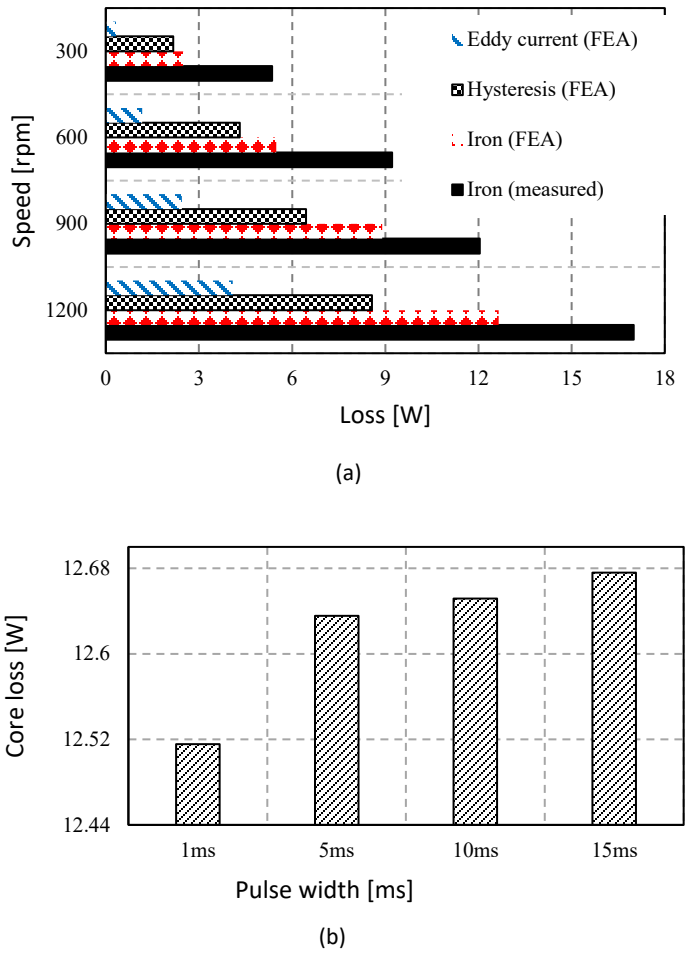

Fig.2-17. No-load machine losses (a) for different speeds at 100% MS. (b) for different magnetization pulse widths at the rated speed.

The motor core loss calculation in the adopted FEA software is based on calculating the machine core losses using curve fitting techniques that utilize core loss data provided by steel manufacturers under sinusoidal excitations. Fig.2-17 (a) shows the FEA no-load machine losses for different speeds at 100% MS. The core loss is shown when the machine is magnetized by a 10 ms pulse width. The hysteresis and eddy current losses are separated. It is seen that the losses increase as the rotor speed increases. At higher speeds, the iron loss increases rapidly, as eddy current loss is proportional to the square of frequency and hysteresis loss is proportional to frequency. The core loss obtained from the FEA has been compared with that obtained from the experiment. The core loss results obtained from the measurement and FEA are in good correlation. The difference can be attributed to the change

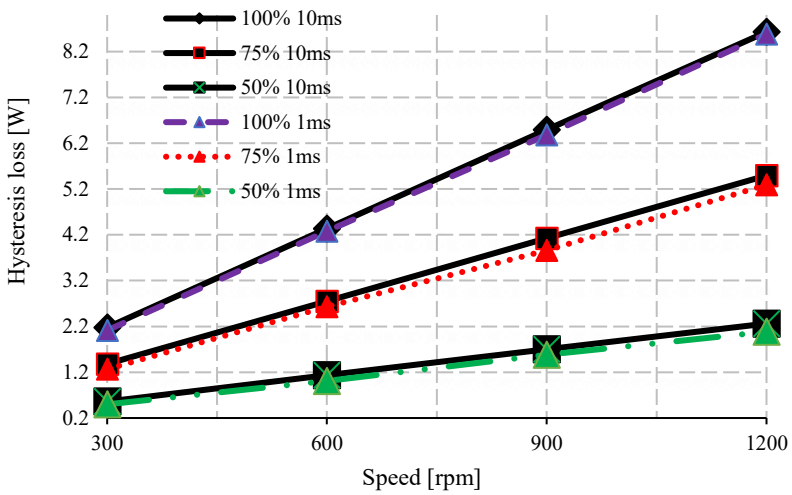

Fig.2-18. Hysteresis loss for different magnetization pulse widths and MSs.

of the magnetic properties of the VF-PMSM steel core during the manufacturing process and errors in the measurement.

Fig.2-17 (b) shows the iron loss for different magnetization pulse widths at the rated speed. With the increase in the pulse width, there is an increase in the loss.

Fig.2-18 shows the hysteresis loss for different magnetization pulse widths and MSs (100%, 75%, and 50%) at the rated speed. It is seen that the hysteresis loss increases linearly with the rotor speed. The higher the magnetizing pulse width and speed, the higher the hysteresis loss.

2.7 Summary

The VF-PMSM used has a non-uniform air gap to avoid unintentional de-magnetization by armature reaction and to reduce magnetizing current. This special design introduces spatial harmonics in the machine back-EMF. A nonlinear adaptive filter that can extract time and frequency varying sinusoidal signals from a nonstationary waveform is used to estimate the back-EMF during the motoring mode. The effect of different magnetizing pulse widths on the machine back-EMF and no-load losses are analyzed. The higher the pulse width, the higher the losses but the back-EMF quality is improved. Although the locked rotor magnetizing process is redundant, lower THD in the back-EMF is observed than other

magnetizing methods. The minimum magnetizing pulse width to magnetize the VF-PMSM 100% is experimentally determined to be 10 ms with a fixed DC bus of 400 V.

Chapter 3. Torque Pulsation Reduction During Magnetization

3.1 Introduction

Torque pulsation is a serious issue from the motor drive perspective and has to be minimized. During the de-magnetization and re-magnetization process, a $d-axis$ current pulse is injected into the machine to change the MS. Since the magnitude of the magnetizing current can be much higher than the machine rated current, an undesired torque is produced if the i_q current is kept constant during the MS change [43]. Thus, during the MS change, the magnet torque, as well as reluctance torque, varies which produces a pulsating torque. The pulsating torque is more severe in inverted-saliency ($L_d > L_q$) type VF-PMSMs since a +ve i_d current will produce higher reluctance torque as well as higher magnet torque.

In chapter 2, the VF PMSM back EMF estimation during the motoring mode is presented. The effect of back EMF harmonics can be used to study the torque ripple. However, in this chapter, pulsating torque due to the magnetization pulse is discussed.

To avoid the pulsating torque, MS control has been implemented on no-load and zero-speed conditions. Smooth torque control during the MS change under nonzero speed and the loaded condition is presented [43]. However, the proposed method based on the voltage disturbance state filter and observer-based current decoupling method is complex.

In this chapter, the pulsating torque issue during the magnetization of an inverted saliency VF-PMSM is investigated. To achieve smooth torque performance during the MS change, the $q-axis$ current reference during re-magnetization is determined by two different methods: the voltage limit method and the load torque method. The derived $q-axis$ current reduces the torque pulsation during re-magnetization.

3.2 Problem Illustration

Fig.3-1 shows the torque-speed and power-speed curves for 100% MS and 50% MS. It can be seen that the torque is reduced to 0.6 p.u. when the magnet is demagnetized to 50% MS. Similarly, the power is also reduced with a reduction in the MS. Although the torque-

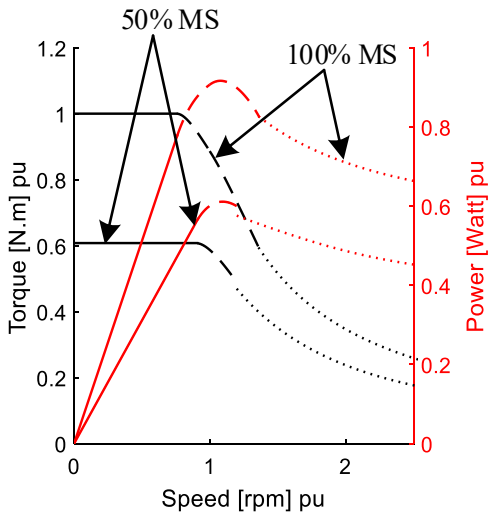

Fig.3-1. Torque-speed and power-speed curve for different MSs.

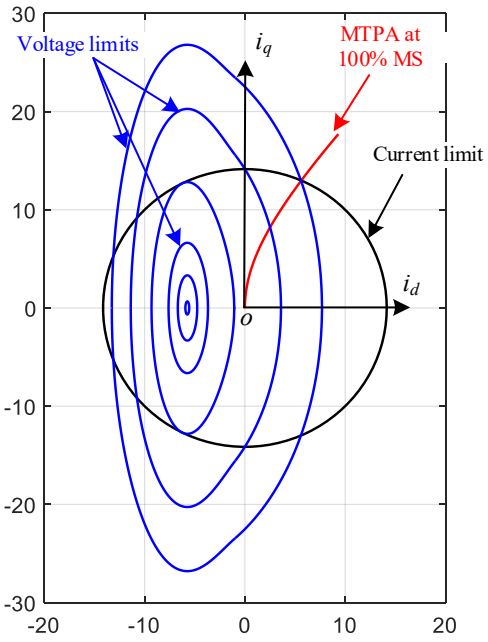

Fig.3-2. Voltage limit curves for different speeds.

speed curve follows the same pattern for different MSs, the base speed at which the maximum torque is achieved is extended for lower MS.

Fig.3-2 shows the voltage limit curves for different speeds. As the speed increases, the voltage limit ellipse shrinks. Theoretically, the maximum speed is achieved when the $q-axis$ current is zero.

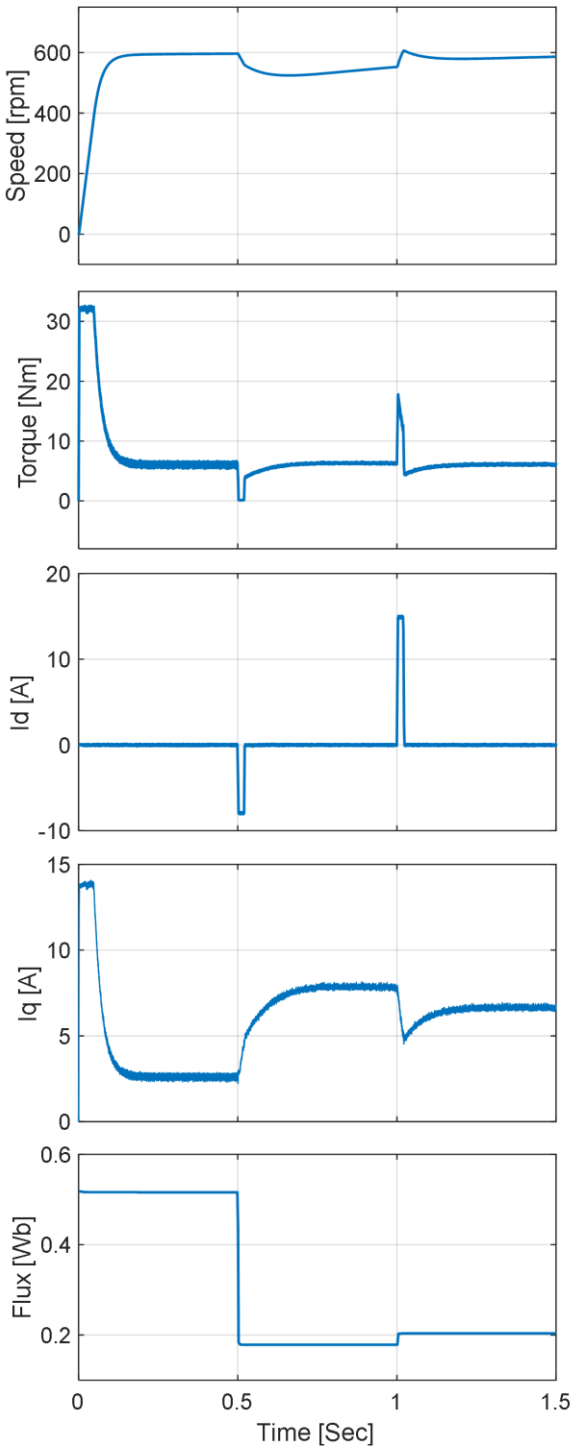

Fig.3-3. De-magnetization and re-magnetization during the loaded condition. Illustration of the pulsating torque during MS change.

Fig.3-3 shows the simulation results during the MS control for nonzero speed and loaded conditions. Initially, the motor is running at 600 rpm, 100% MS with 6 $N.m$ of load torque.

A de-magnetization pulse of 8 A and a re-magnetization pulse of 15 A are injected at 0.5 s and 1 s, respectively. These de-magnetization and re-magnetization pulses will change the magnet flux linkage based on the amplitude of the current pulse. Since the magnet flux linkage is decreased at 0.5 s, the $q-axis$ current increases to generate the same torque. However, the injected $d-axis$ current abruptly changes the magnet torque as well as reluctance torque and results in a pulsating torque.

The VF-PMSM used in this study is designed with positive saliency, $L_d > L_q$ [11]. This allows the maximum torque to be obtained with a magnetizing $d-axis$ current component that stabilizes the low-coercive field magnets at high torque conditions. The torque is defined as

$$T = \frac{3P}{2}\left[i_q\,\lambda_m(i_d) + \left(L_d - L_q\right) i_d i_q\right] \tag{3-1}$$

The torque depends on the $dq-axes$ armature currents and λ_m. Since λ_m is a function of i_d, both the magnet torque as well as reluctance torque are changed with the MS change, resulting in pulsating torque. The $d-axis$ current needed to demagnetize and remagnetize the magnets are shown in Fig.3-4. The de-magnetizing current is within the machine-rated current while the amount of $d-axis$ current to magnetize the magnet is much higher than the machine-rated current. Due to this higher re-magnetizing current, higher pulsating torque is seen during the magnetization in Fig.3-3.

Therefore, pulsating torque is inevitable during the MS change in a VF-PMSM if the $q-axis$ current is not controlled. The magnitude of the pulsating torque depends on the injected $d-axis$ current amplitude to change the MS and its corresponding effect on the magnet flux linkage. Hence, the objective is to mitigate the pulsating torque during the change in the magnetization state.

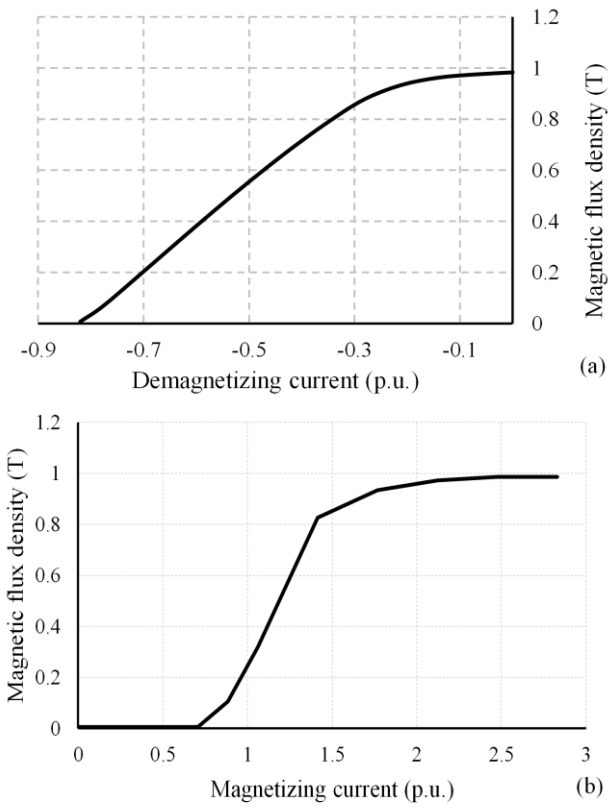

Fig.3-4. Magnetic flux density versus $d-axis$ current (p.u.). (a) De-magnetization curve. (b) Re-magnetization curve.

3.3 Proposed Torque Pulsation Reduction Methods

Usually, the $q-axis$ current reference is determined by the speed error $(\omega^* - \omega)$ through the proportional-integral (PI) controller. However, during the MS control, both the magnet torque and reluctance torque change resulting in speed oscillations. The speed oscillation depends on the injected $d-axis$ current amplitude. Thus, if the same $q-axis$ current is taken as a reference to generate the $q-axis$ voltage, the pulsating torque will be high.

Two different $q-axis$ current control methods are proposed.

3.3.1 Voltage Limit - Method I

The dynamics of a VF-PMSM is given by

$$v_d = R_s i_d + L_d \frac{di_d}{dt} - \omega_e L_q i_q$$
$$v_q = R_s i_q + L_q \frac{di_q}{dt} + \omega_e L_d i_d + \omega_e \lambda_m(i_d). \tag{3-2}$$

Assuming the steady-state condition,

$$v_d = R_s i_d - \omega_e L_q i_q$$
$$v_q = R_s i_q + \omega_e L_d i_d + \omega_e \lambda_m(i_d). \tag{3-3}$$

The vector sum of the $dq - axes$ voltage has to be less or equal to the maximum available voltage from the inverter [63]. The voltage limit is given as

$$v_d^2 + v_q^2 \leq v_s^2. \tag{3-4}$$

Solving the voltage limit equation for i_q gives

$$(R_s i_d - \omega_e L_q i_q)^2 + (R_s i_q + \omega_e L_d i_d + \omega_e \lambda_m(i_d))^2 = v_s^2. \tag{3-5}$$

i.e.
$$i_q{}^2\left(R_s{}^2 + \omega_e{}^2 L_q{}^2\right) + i_q\left[2R_s\omega_e\left((L_d i_d + \lambda_m(i_d) - L_q i_d\right)\right]$$
$$= -\left[\left(\omega_e\left(L_d i_d + \lambda_m(i_d)\right)\right)^2 + R_s{}^2 i_d{}^2 - v_s^2\right]. \tag{3-6}$$

The solution of the quadratic equation is given as

$$i_q = \frac{R_s\omega_e\left((L_d i_d + \lambda_m(i_d) - L_q i_d\right) + \sqrt{\left(R_s\omega_e(L_d i_d + \lambda_m(i_d) - L_q i_d\right)^2 - \left(R_s{}^2 + \omega_e{}^2 L_q{}^2\right)\left(\left(\omega_e\left(L_d i_d + \lambda_m(i_d)\right)\right)^2 + R_s{}^2 i_d{}^2 - v_s^2\right)}}{\left(R_s{}^2 + \omega_e{}^2 L_q{}^2\right)} \tag{3-7}$$

Fig.3-5 shows the block diagram of the VF-PMSM drive system. A vector control strategy is used to control the speed and the magnet flux linkage. The magnetization and de-magnetization current control is included in the standard vector control for the PMSM drive. The current pulses are manually controlled based on speed and load requirements by the Mag/Demag pulse command block. The $q - axis$ current control unit during the MS control

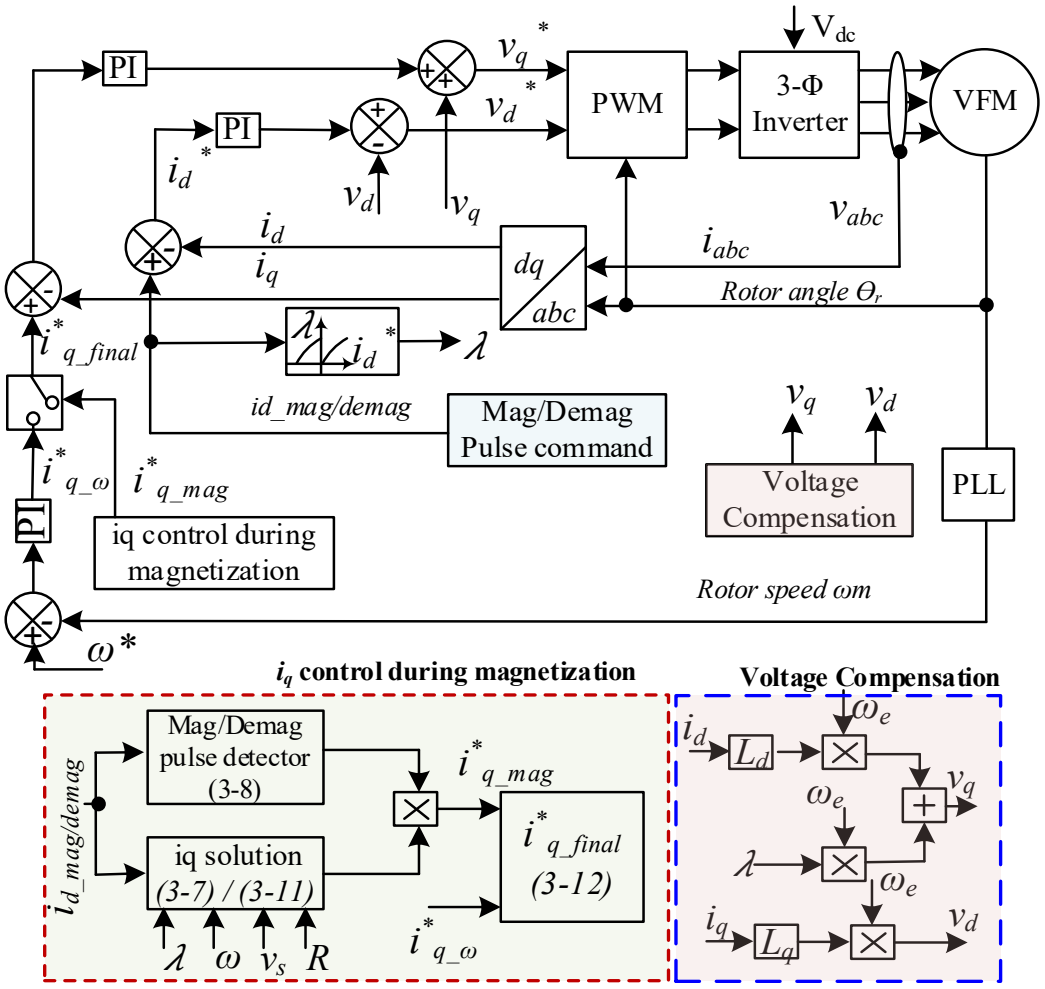

Fig.3-5. Block diagram of the drive system.

is highlighted by the red-dashed rectangle. The $q-axis$ current control unit is a relay-based circuit, which can detect the de-magnetizing or re-magnetizing pulse by the Mag/Demag pulse command block.

Hence, once the magnetizing or de-magnetizing pulse is detected, the $q-axis$ current determined by equation (3-7) is given as the $q-axis$ current reference. The Mag/Demag pulse detector block has the following characteristics.

$$y = f(x) = \begin{cases} 1, & for\ x < -1\ (Demag) \\ 0, & for -1 \le x \le 1 \\ 1, & for\ x > 1\ (Mag) \end{cases} \tag{3-8}$$

The output from equation (3-8) is multiplied by the i_q solution determined by (3-7). If the Mag/Demag pulse command block is active, i_q is determined by the voltage limit method else by the speed error PI controller. The final $q-axis$ current reference that determines the $q-axis$ voltage, $i^*_{q\_final}$ is given by:

$$i^*_{q\_final} = \begin{cases} i^*_{q\_mag}, & for\ x \neq 0 \\ i^*_{q\_w}, & for\ x = 0 \end{cases} \tag{3-9}$$

Fig.3-6 shows the pulse detection and $i^*_{q\_final}$ generation results. First, the de-magnetization and re-magnetization signals are detected. The $q-axis$ current calculated by equation (3-7) is determined. A control block given by equation (3-9) will select the $q-axis$ current either from the speed error PI controller or from the voltage limit method.

Fig.3-7 shows the simulated results for the same operating conditions as in Fig.3-3. The proposed method has a swift change in the $q-axis$ current for both de-magnetization and re-magnetization. Since the de-magnetization current pulse amplitude is lower than the machine-rated current, a lower pulsating torque is observed. However, the proposed method produces higher pulsating torque during the de-magnetization process. Thus, in further studies, the proposed method is only implemented for the re-magnetization process.

3.3.2 Load Torque - Method II

As given by equation (3-1), the electromagnetic torque depends on i_d, i_q and λ_m. For a given magnetizing or de-magnetizing current the corresponding λ_m can be calculated. Then the corresponding i_q can be determined from the torque equation. If the change in the speed is ignored then the torque is given as

$$T_e = T_{load} + B\omega \tag{3-10}$$

Using, (3-1) in (3-10), i_q can be calculated as

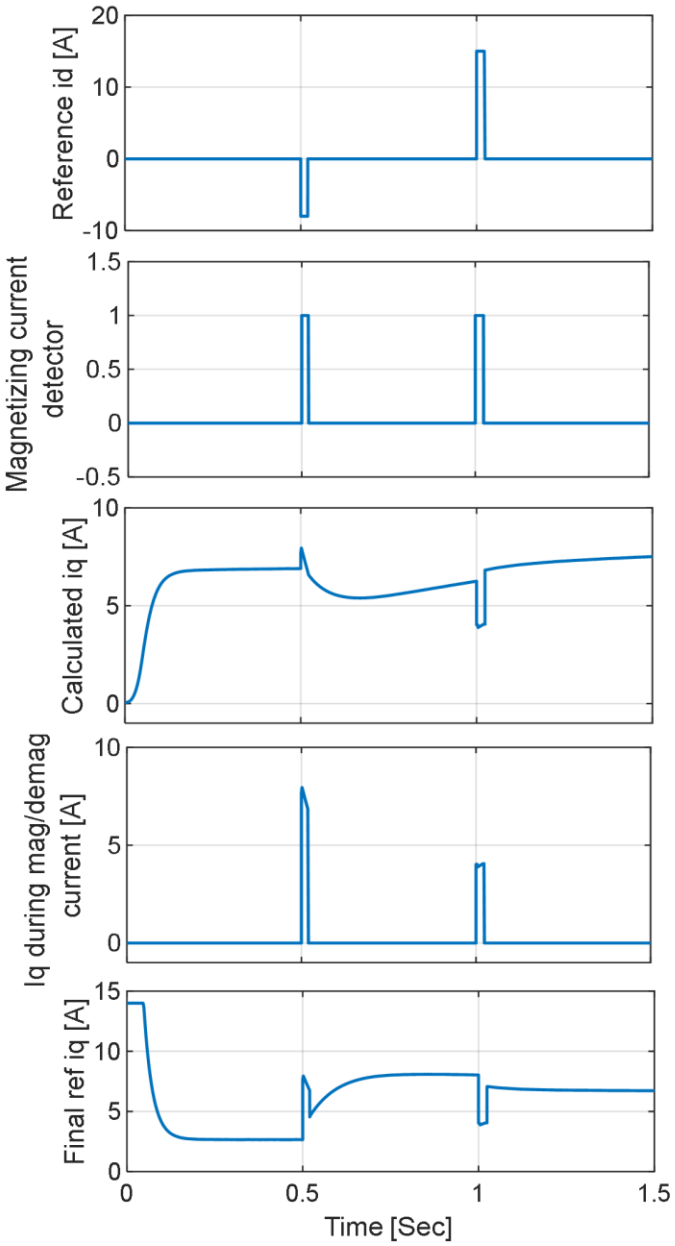

Fig.3-6. De-magnetization and re-magnetization detection and the corresponding final $q-axis$ current generation process.

$$i_q = \frac{T_{load} + B\omega}{\frac{3P}{2}\left[\lambda_m(i_d) + \left(L_d - L_q\right) i_d\right]} \tag{3-11}$$

As given by equation (3-9), $i^*_{q\_final}$ is generated only during the MS change. The overall combined equation is given as

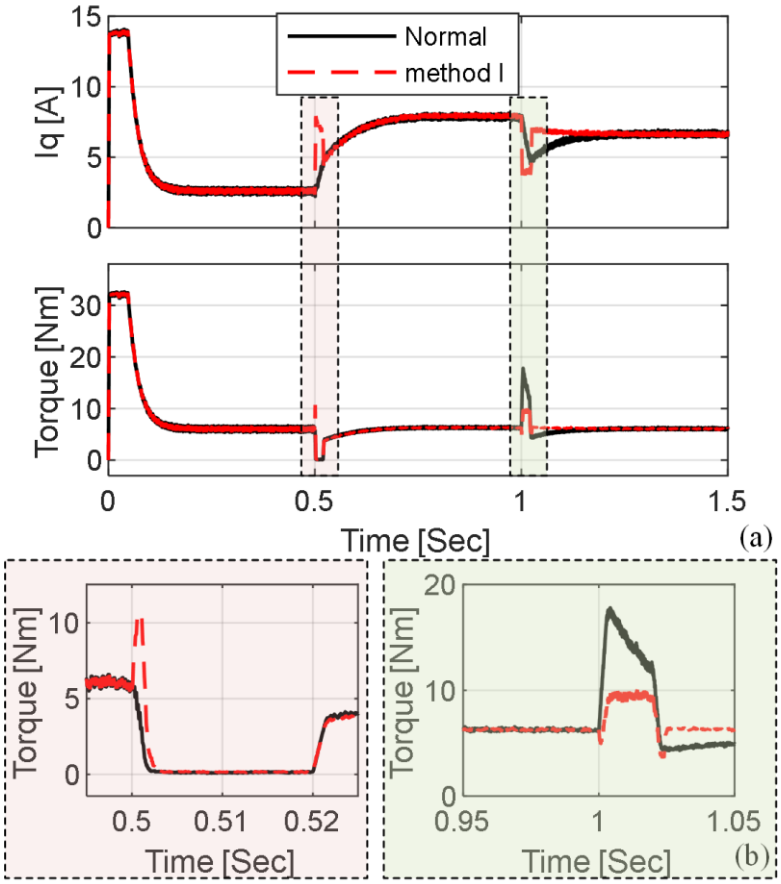

Fig.3-7. De-magnetization and re-magnetization during the loaded condition. (a) Illustration of the pulsating torque during MS change for different methods. (b) zoomed view during MS change for torque.

$$i^*_{q\_final} = \begin{cases} i^*_{q\_mag}\ (3\text{-}7)\,, & for\ x \neq 0 (Method\ I) \\ i^*_{q\_w}, & for\ x = 0\ (Normal) \\ i^*_{q\_mag}\ (3\text{-}11), & for\ x \neq 0\ (Method\ II) \end{cases} \tag{3-12}$$

In order to compare the results, all three methods given by equation (3-12) are plotted together in Fig.3-8. The motor speed drops with the de-magnetizing pulse while it increases with the re-magnetizing pulse in the method where i_q is controlled by the speed error PI controller. For the proposed methods, since the i_q current is controlled based on the speed, magnet flux linkage and torque, lower oscillations are observed in the speed.

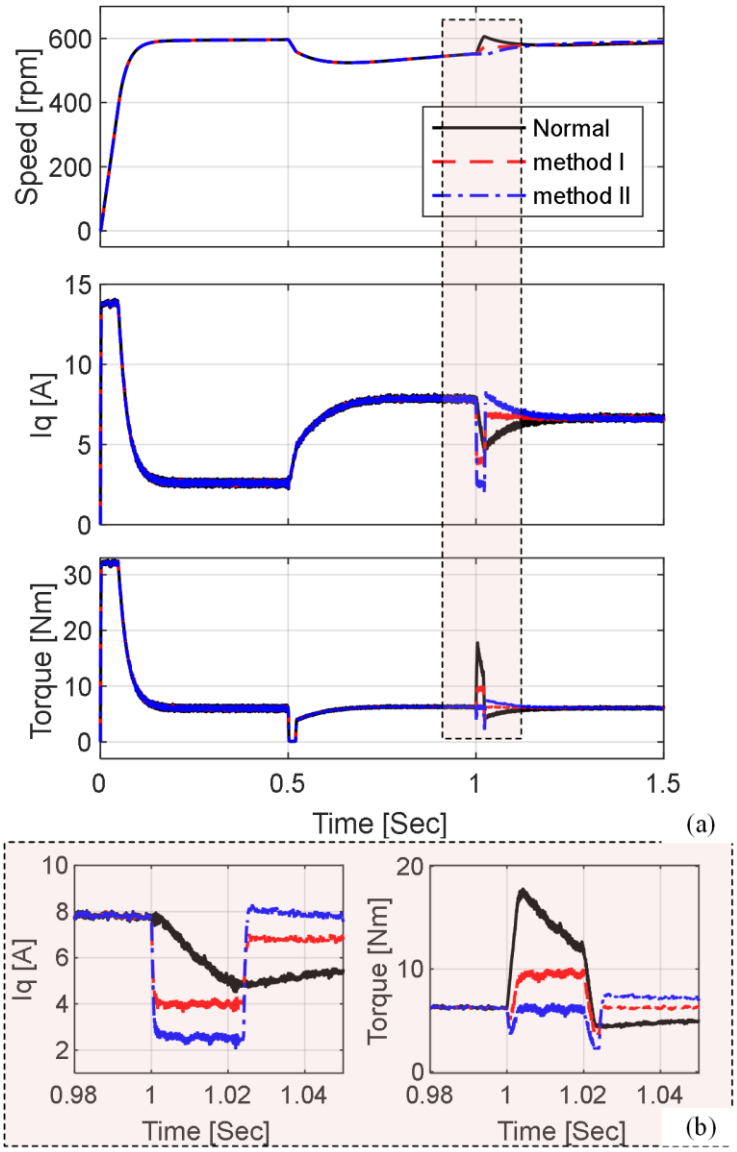

Fig.3-8. De-magnetization and re-magnetization during the loaded condition. (a) Illustration of the pulsating torque during magnetization for different methods. (b) zoomed view during magnetizing pulse for i_q and torque.

Fig.3-8 (b) shows the zoomed view of i_q and torque for the magnetization period. With the correction in the $q-axis$ current reference, lower pulsating torque is observed. The torque response shows that method II, based on load torque produces lower pulsating torque during the magnetization process.

3.4 Experimental Verification

Fig.3-9 shows the VF-PMSM machine test setup. The test bench includes a direct current (DC) dynamometer, torque and speed transducers, a real-time simulator and sensors, a voltage source inverter (VSI), a position encoder, and a data acquisition unit.

The VF-PMSM is coupled to a dc dynamometer through a torque transducer. The dc dynamometer is controlled by a DCS800-DC drive. The VF-PMSM is driven by a two-level VSI. The inverter switching frequency is 5 kHz. The rotor position is given by a 12-bit optical encoder that is mounted on the machine shaft. An OPAL-RT controller is used for real-time control.

During the experiment, first, the VF-PMSM speed is controlled by a VSI as shown in Fig.3-5. Then, the DC dynamometer is controlled in the torque control mode, to produce the required load torque for the VF-PMSM. Once the VF-PMSM is running at the loaded condition, the de-magnetizing and re-magnetizing pulses of 10 ms pulse width are injected

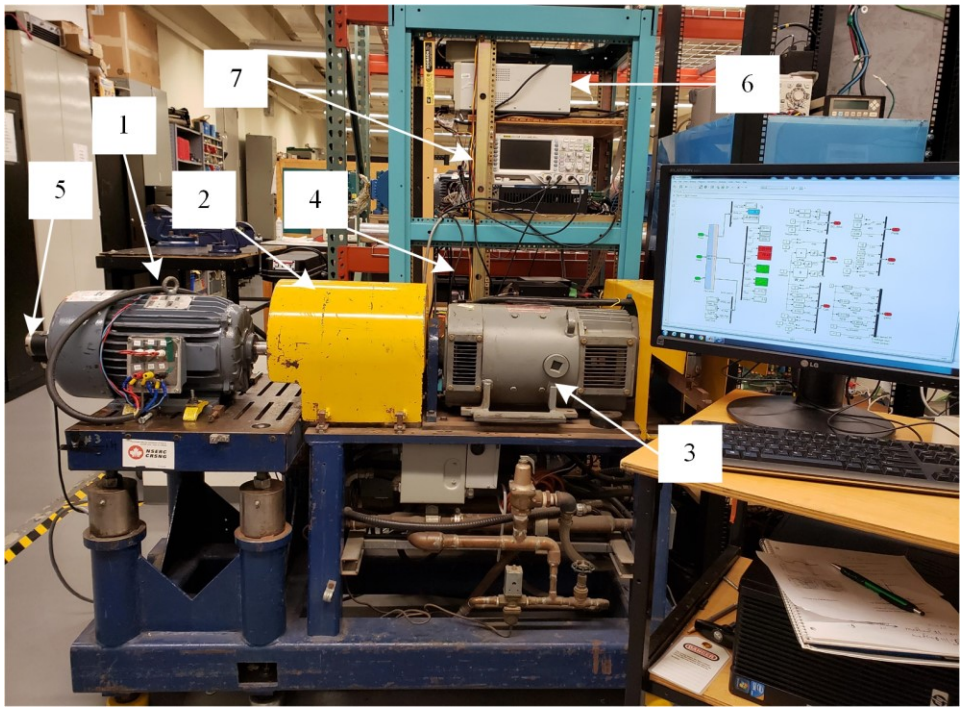

Fig.3-9. VF-PMSM test setup. (1) VF-PMSM; (2) Transducers; (3) Dynamometer; (4) Real-time simulator and sensors; (5) Encoder; (6) DC supply; (7) Data acquisition.

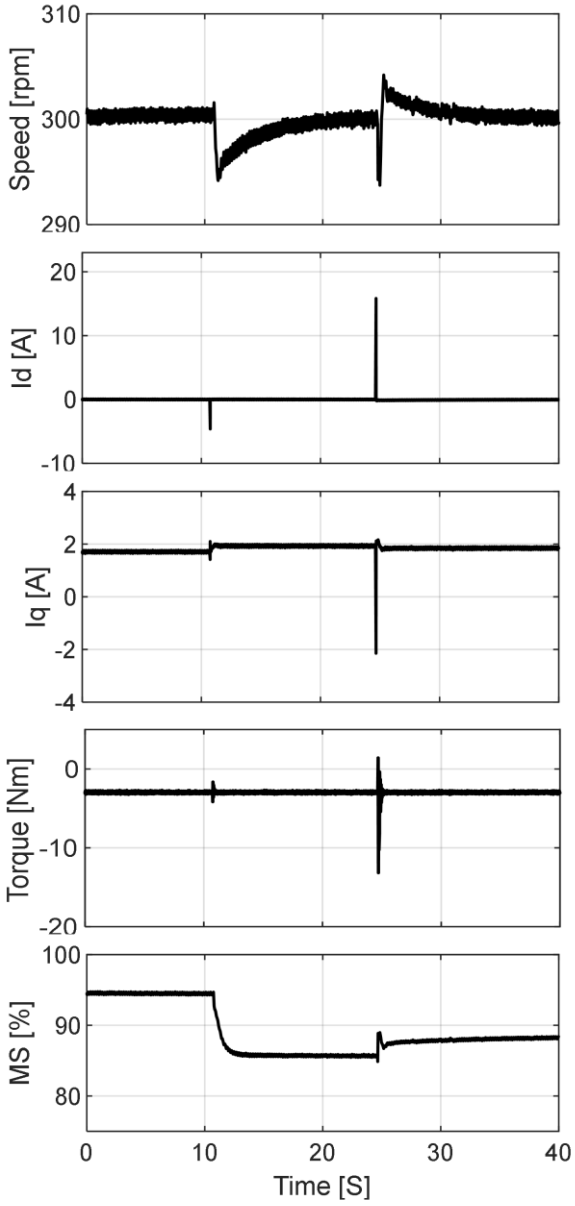

Fig.3-10. De-magnetization and re-magnetization during the loaded condition. Illustration of the pulsating torque during MS change.

manually in the VF-PMSM. In this study, we are not concerned about pulse width but only on the magnitude of the re-magnetizing pulse.

Fig.3-10 shows the experimental results during the MS change at nonzero and loaded conditions. Initially, the motor is running at 300 rpm, 95% MS with 3 N.m of load torque. A de-magnetization pulse of 5 A and a re-magnetization pulse of 15 A are applied at 10.8 s and

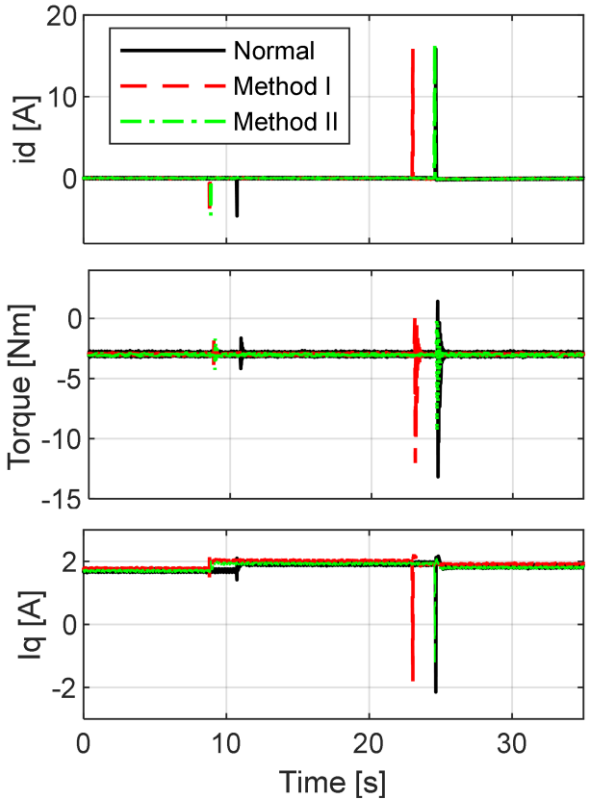

Fig.3-11. Illustration of the pulsating torque during magnetization for different methods.

24.6 s, respectively. These de-magnetization and re-magnetization pulses change the magnet MS. Since the magnet MS varies with the $d-axis$ current, the magnet torque as well as reluctance torque change, which results in pulsating torque. Since the load torque is applied by the dynamometer, torque is seen negatively in Fig.3-10.

The torque response for different re-magnetizing methods is shown in Fig.3-11. Since the de-magnetizing and re-magnetizing pulse are manually injected, the time step is not the same for different methods. The re-magnetizing pulse is applied at 23 s, 24.6 s, and 24.7 s for method I, method II and normal method, respectively. Similar pulsating torque is observed during the de-magnetization for all methods since the proposed algorithm is only implemented during the re-magnetization period. For the same amount of re-magnetizing current, method II, based on the load torque generates lower pulsating torque.

3.5 Summary

During the de-magnetization and re-magnetization process, a $d-axis$ pulse is injected into the VF-PMSM to change the MS. However, apart from the change in the magnet flux linkage, the magnet torque, as well as the reluctance torque abruptly change. This change in machine torque produces the pulsating torque. This pulsating torque is created when the magnet is demagnetized or remagnetized at nonzero and loaded conditions. Moreover, the pulsating torque is more severe during re-magnetization because of the higher amplitude of the re-magnetizing current. To solve this problem, the $q-axis$ current reference during the magnetization period is determined by two different methods: the voltage limit method and the load torque method. The derived $q-axis$ current reduces the torque pulsation during the re-magnetization process at nonzero speed and loaded conditions.

Chapter 4. Automatic Flux Linkage and Inductance Measurement at the Different Magnetization States

4.1 Introduction

An accurate estimation/ measurement of machine parameters is required for high-performance trajectory tracking controller [73], [74], [75]. The machine's performance in terms of power and torque depends on the inductance, flux linkage, stator resistance, rotor position, etc. For accurate control and efficiency optimization, saturation and cross magnetization should be considered [76], [77], [78], [79] [80], [81].

Several methods have been proposed to measure the parameters of PMSMs [82], [83], [84] and synchronous reluctance machines [85], [86], [87]. The $dq-axes$ flux linkage and inductance identification methods can be broadly classified into rotational tests and standstill tests. The rotational test methods can be further classified into the constant speed method and dynamic testing method. Although the rotational test method gives highly accurate results, it requires a full dynamometer setup and cannot be used to measure the position-dependent flux linkages.

The DC standstill test and AC standstill test are the most popular parameter measurement methods. In the DC standstill method, the machine is locked at the axis on which the measurement is to be performed and requires post-processing from the recorded data. In the AC standstill method, an AC voltage is applied at the axis on which the inductance is to be measured. However, the VF-PMSMs are demagnetized with a negative $d-axis$ current. Thus, the AC standstill method cannot be justified for VF-PMSMs.

In the standstill method, a pulsed voltage to the machine is applied in open-loop to measure the flux-linkage [87], [88]. These methods require post-processing of a huge dataset. A current control-based parameter identification using the standstill method is presented in [89]. A current pulse is applied in closed-loop to obtain the machine resistance and inductance in two steps. However, this method cannot be used to generate the machine

parameters in real-time since it requires the controller parameters tuning for each operating point.

In this chapter, a current control-based method proposed in [86] is used to measure flux linkage, inductance and resistance for the VF-PMSM at different MSs. Automated real-time parameter measurements are performed without requiring offline post-processing. This method utilizes the vector-controlled VF-PMSM drive to measure parameters that remove the requirement of locking the rotor at different axes.

4.2 Inductance variation in VF-PMSM

VF-PMSMs have one more dimension for MS control: magnet flux linkage. The magnet flux in the VF-PMSMs is changed based on the MS. This leads to a non-linear change in machine inductances for different operating conditions [88], [90]. The change in the VF-PMSM $d-axis$ inductance is shown in Fig.4-1.

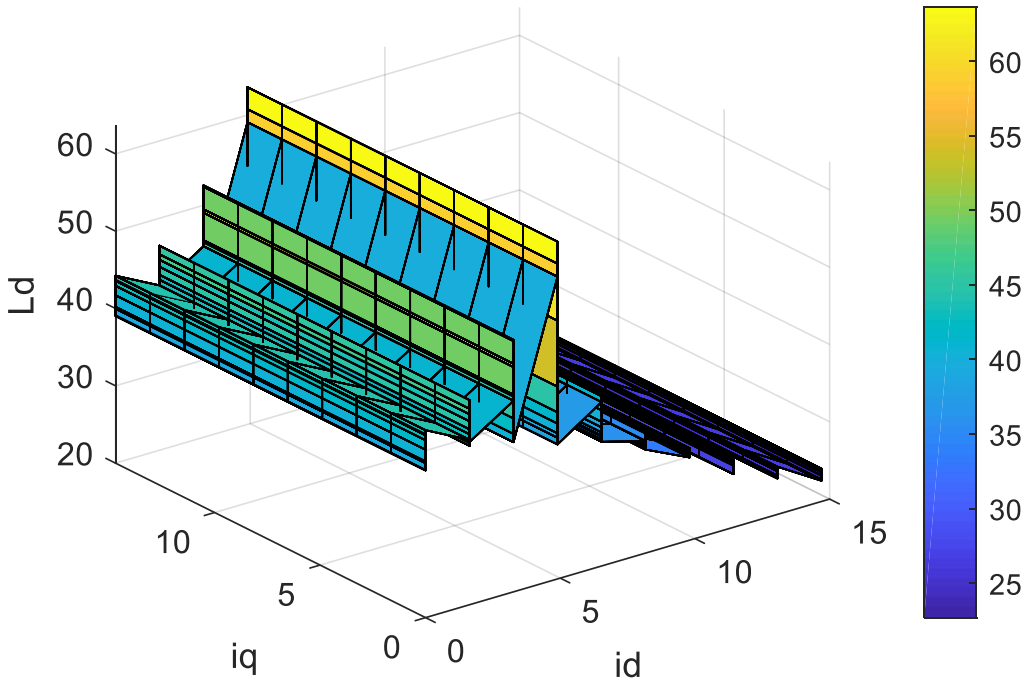

Fig.4-1. FEA generated $d-axis$ inductance.

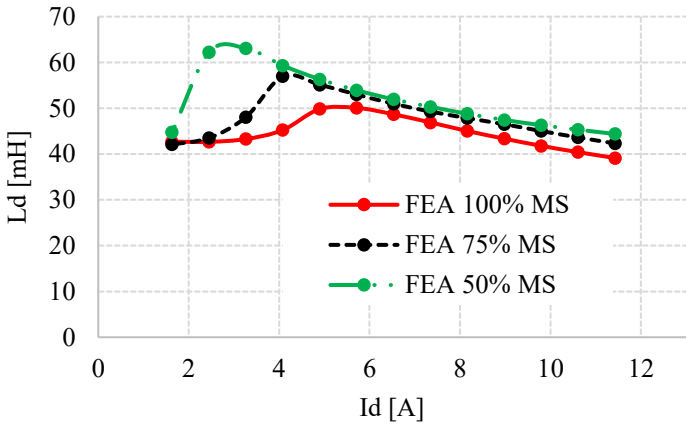

(a)

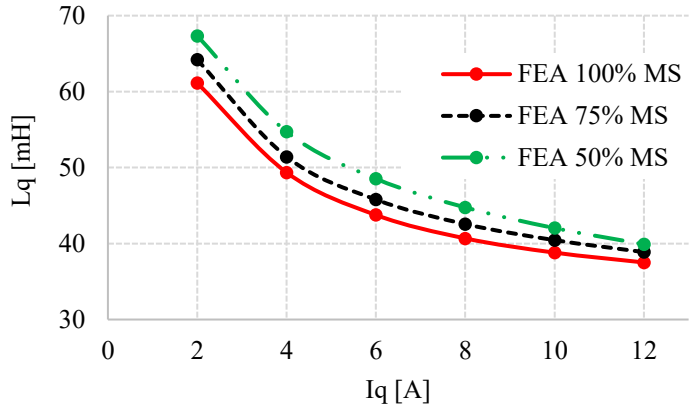

(b)

Fig.4-2. FEA generated $dq-axes$ inductance variations for different MSs.

The variation of the $d-axis$ inductance and $q-axis$ inductance for different MSs are shown in Fig.4-2 for a tangentially magnetized 5 hp VF-PMSM. Thus, $dq-axes$ inductances and flux linkage measurements are of prime importance for high-performance control.

The equations describing the dynamics of the VF-PMSM are given in (3-2) and can be rewritten as follows:

$$\begin{bmatrix} v_d \\ v_q \end{bmatrix} = R_s \begin{bmatrix} i_d \\ i_q \end{bmatrix} + p \begin{bmatrix} \lambda_d \\ \lambda_q \end{bmatrix} + \omega \begin{bmatrix} -\lambda_q \\ \lambda_d \end{bmatrix} \tag{4-1}$$

The $dq-axes$ flux linkage are given as

$$\lambda_d = L_d i_d + \lambda_m(i_d) \qquad (4\text{-}2)$$
$$\lambda_q = L_q i_q$$

During the locked rotor test, the rotor speed is zero and (4-1) is reduced to

$$v_d = R_s i_d + p\lambda_d \qquad (4\text{-}3)$$
$$v_q = R_s i_q + p\lambda_q$$

In the existing voltage pulse-based standstill tests, a voltage pulse is supplied in either of the $dq - axes$ to measure the corresponding $axis$ inductance [82], [87], [88]. To measure the $d - axis$ parameters, arbitrary v_d and $v_q = 0$ are given. However, the actual v_q at the machine terminal is not zero due to the nonlinear effect of the voltage source inverter. Moreover, since the voltage pulse is applied to excite the motor, the response of the machine depends on the electrical time constant. Thus, this method will have lower accuracy for a lower electrical time constant machine. Since the lower time constant machine requires a higher sampling frequency, the data processing becomes challenging due to the processor sampling time limit.

To overcome these problems, a closed-loop current control-based parameter measurement method is implemented using the real-time system. In this method, a pulsed current reference is applied in either of the axes and a constant current is applied to the other axis. Since both currents are controlled, the machine parameters can be computed at any arbitrary operating point in the $i_{\mathrm{d}} i_q$ plane.

Fig.4-3 shows the block diagram of the VF-PMSM drive system to measure the $q - axis$ flux linkage and inductance. The rotor is locked and a pulse $q - axis$ current is injected to measure the $q - axis$ parameters. A different range of constant $d - axis$ current is also supplied to check the parameter variation due to the cross-coupling effect. A three-phase VSI is used to supply the desired voltages in PWM form. The controller controlling the fixed current is made much faster compared to the controller controlling the pulsed current to keep the fixed current constant.

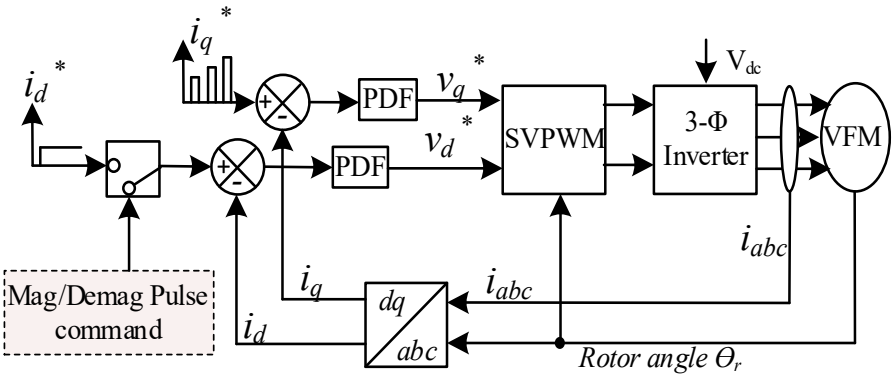

Fig.4-3. VF-PMSM $q-axis$ flux linkage and $q-axis$ inductance measurement system.

If the ratio of K_i to K_p is less than the natural frequency of the system in the PI controller, it causes overshoot in the system even though the closed-loop poles are critically damped. Thus, pseudo-derivative feedback (PDF) current controllers are used to control the currents. The main reason for choosing a PDF controller is its ability to achieve a critically damped response to several first-order systems [86], [91], [92]. The PDF controller can achieve a critically damped response for different step changes in the reference input.

A Magnetizing/De-magnetizing pulse command block is included in the VF-PMSM drive system as shown in Fig.4-3. This block allows changes in the MSs. The magnetizing or de-magnetizing current pulses are manually supplied by this block. Thus, flux linkage and inductance maps can be generated for different MSs without disconnecting the system.

The current and voltage responses at the machine terminals are measured. The measured current and voltage are used in (4-4) and (4-5) to compute the VF-PMSM flux linkage. The expressions for the $dq-axes$ flux linkage are given as

$$\lambda_d = \int_0^t v_d(t) - R_s \int_0^t i_d\,(t) \tag{4-4}$$

$$\lambda_q = \int_0^t v_q(t) - R_s \int_0^t i_q\,(t) \tag{4-5}$$

The stator resistance, R_s is calculated as a ratio of the average steady-state voltage to the average steady-state current during each pulse. However, it is assumed to remain constant during the integration period.

The inductances are calculated from the calculated flux linkage and currents. The expressions for the $dq - axes$ inductance are given as

$$L_d = \lambda_d / i_d \tag{4-6}$$

$$L_q = \lambda_q / i_q \tag{4-7}$$

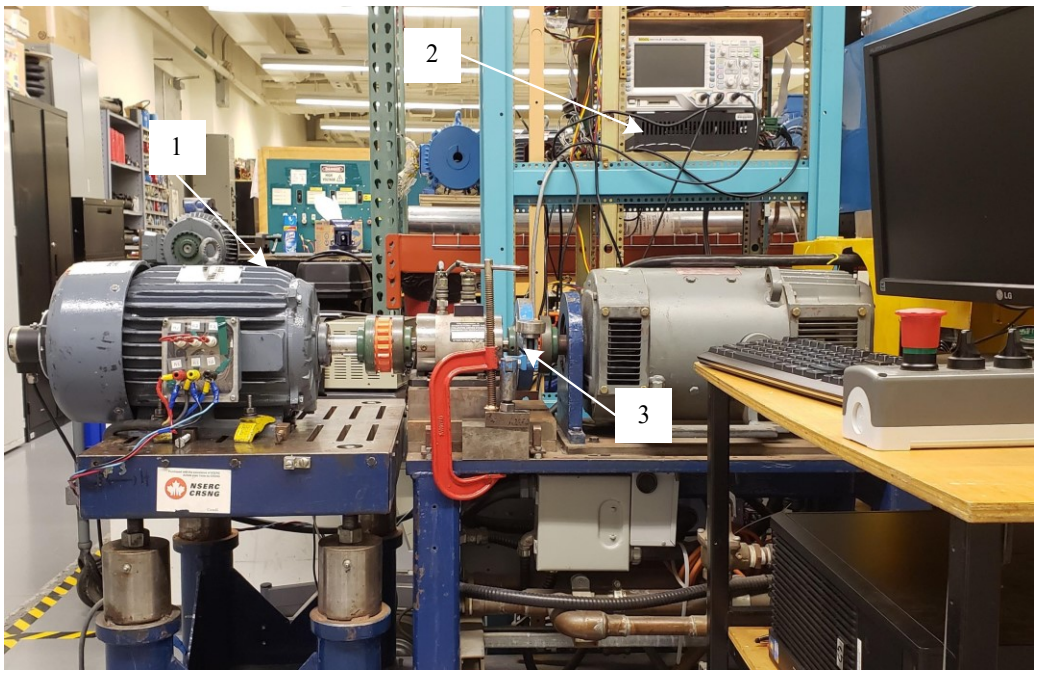

Fig.4-4. VF-PMSM test setup. (1) VF-PMSM (2) Real-time simulator (3) Rotor lock mechanism.

4.3 Experimental Setup And Results

The experimental setup is shown in Fig.4-4. The VSI switching frequency is 5 kHz. An OPAL-RT (OP5142) is used for real-time control. The rotor is locked using a mechanical clamp. The DC voltage is kept constant throughout the experiment. The dynamometer has no important role in the experiment. The machine is coupled with the dynamometer just to have a rigid locking mechanism.

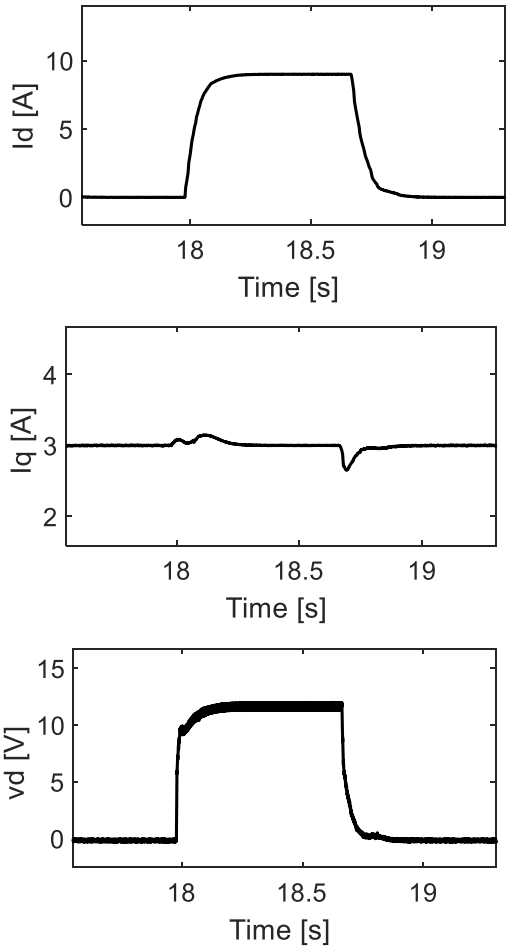

Fig.4-5. v_d response when a pulse i_d and fixed i_q are applied.

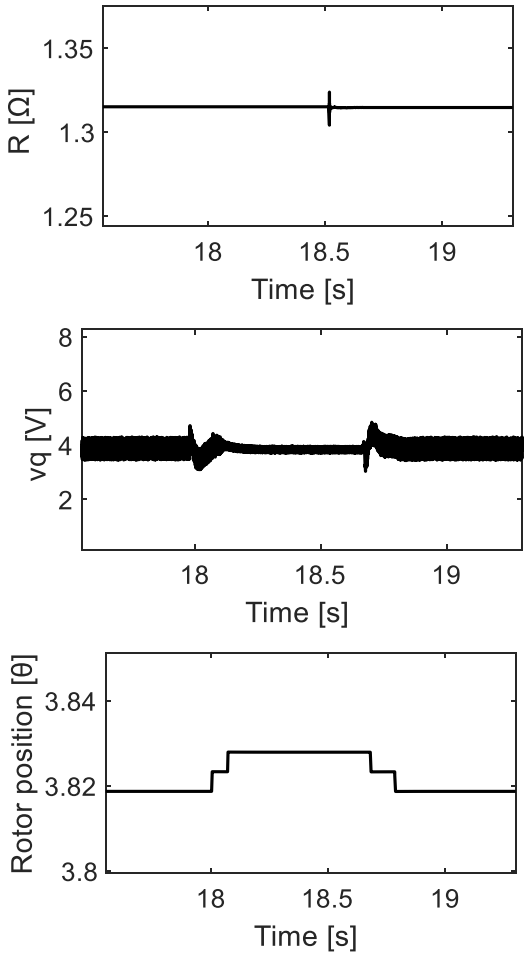

Fig.4-6. Resistance, v_q, and postion response when a pulse i_d and fixed i_q are applied.

Fig.4-5 and Fig.4-6 show the response of the VF-PMSM when a reference pulse current of $i_d = 9A$ and $i_q = 3\ A$ are applied. The voltage and current response for $dq - axes$ are shown. It can be seen that the currents are controlled with little oscillation in the $q - axis$ for the $d - axis$ pulse reference. The steady-state resistance is calculated from the steady-state voltage and current. Change in the rotor position due to the pulse current is minimal.

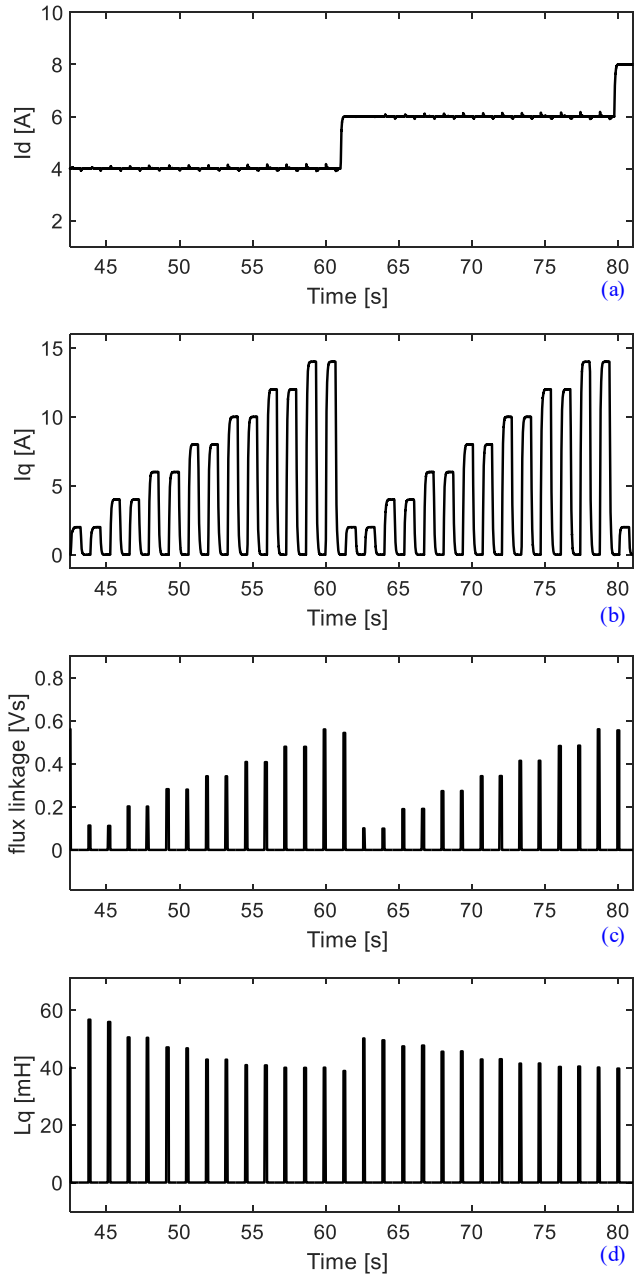

Fig.4-7. Procedure to measure the $q-axis$ flux linkage and inductance by applying the $q-axis$ pulse current for different fixed $d-axis$ currents.

Fig.4-7 shows the procedure to measure the $q-axis$ flux linkage and inductance as a function of the $q-axis$ pulse current for different fixed $d-axis$ currents. Two current pulses are supplied for each operating condition for higher accuracy. The final flux linkage

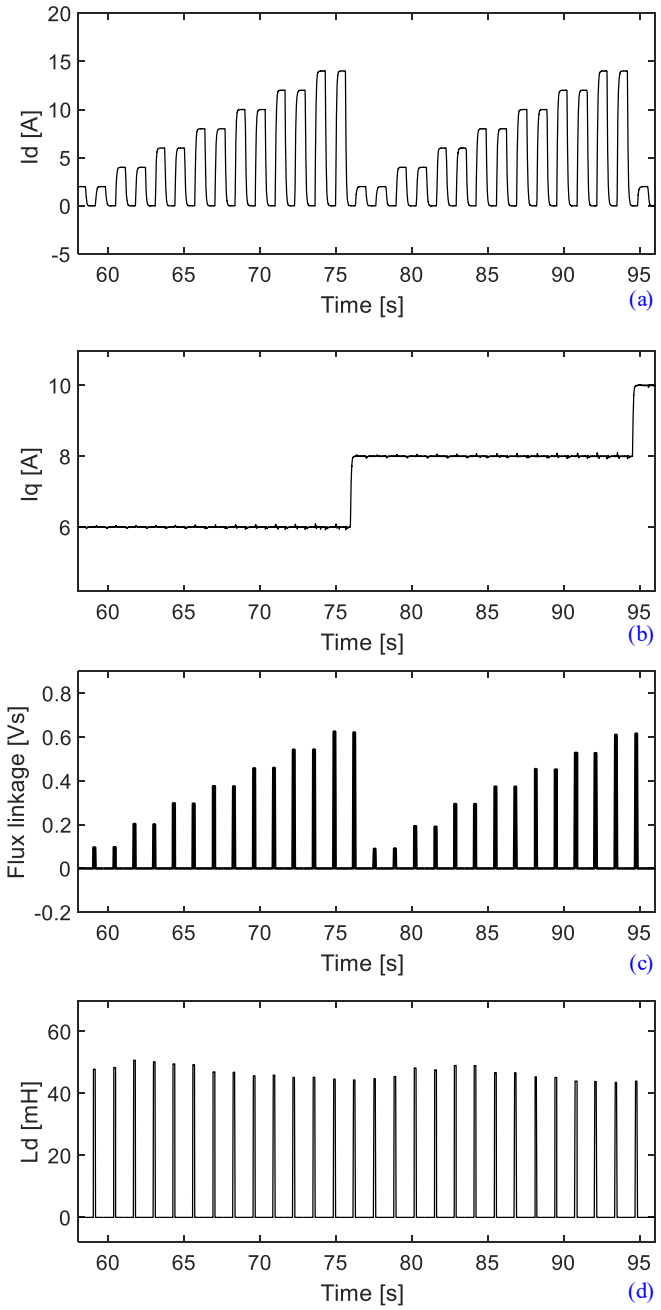

Fig.4-8. Procedure to measure the $d-axis$ flux linkage and inductance by applying the $d-axis$ pulse current for different fixed $q-axis$ currents.

and inductances are the average of two pulses at that particular operating point. Since the calculations (4-4) - (4-7) are performed in real-time; flux linkage, inductance and steady-state resistance maps can be generated at any given operating point.

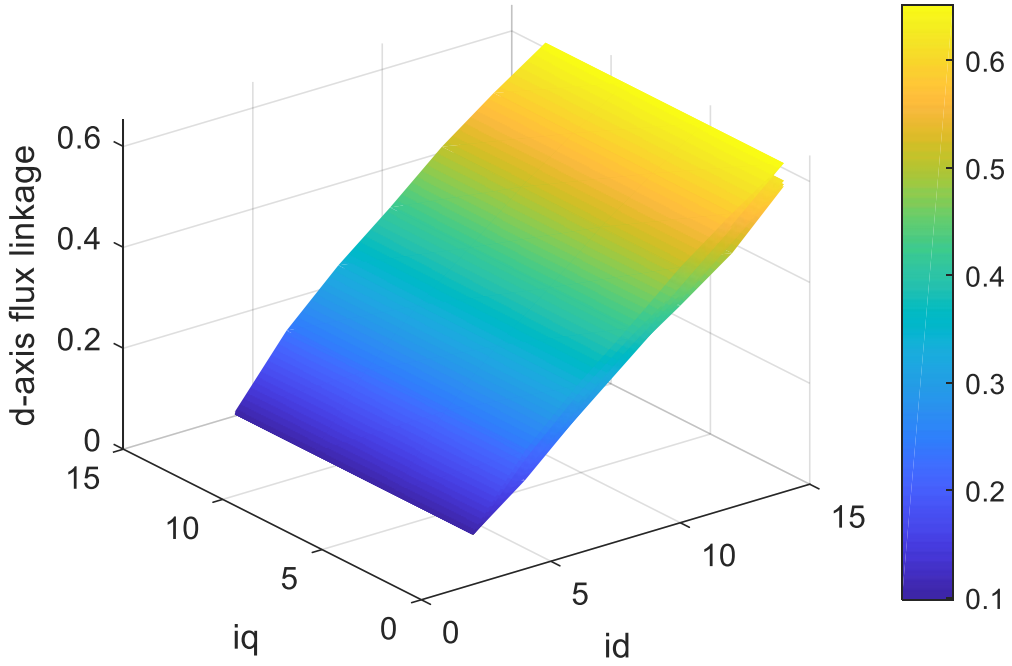

Fig.4-9. $d-axis$ flux linkage at 75% MS.

Fig.4-8 shows the procedure to measure the $d-axis$ flux linkage and inductance as a function of the $d-axis$ pulse current for different fixed $q-axis$ currents. Two current pulses are supplied for each operating condition for higher accuracy. The final flux linkage and inductances are the average of two pulses at that particular operating point.

Fig.4-9 shows the measured $d-axis$ flux linkage at 75% magnetization level. The $d-axis$ flux linkage is shown as a function of $q-axis$ current at different values of $d-axis$ current.

Fig.4-10 shows the $d-axis$ inductance as a function of $d-axis$ current at 75 % MS. It is seen that the inductance increases to 4 A and starts decreasing. This effect is developed as a result of the machine geometry and permeability of the M19G19 steel.

$$L = \frac{N^2 \mu_0 \mu_r A}{l} \tag{4-8}$$

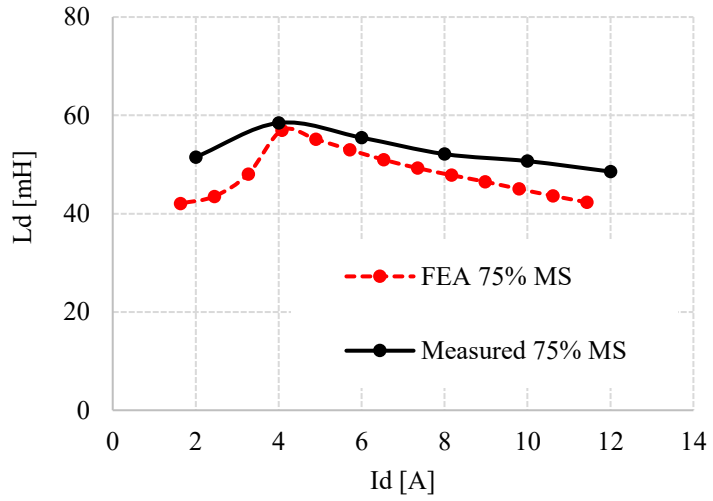

Fig.4-10. $d-axis$ inductance as a function of $d-axis$ current.

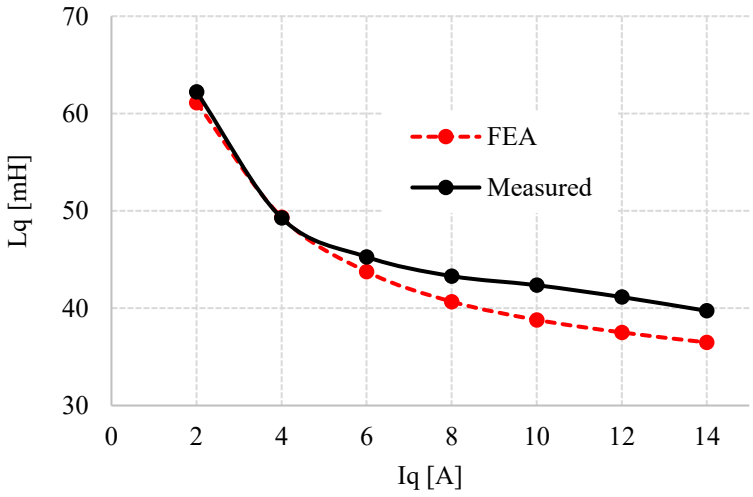

Fig.4-11. $q-axis$ inductance as a function of $q-axis$ current.

$$\mathcal{R} = \frac{l}{\mu_0 \mu_r A} \tag{4-9}$$

In (4-8) and (4-9), area A, the number of turns N^2 and magnetic path l are constant. Thus, $d-axis$ inductance follows the steel permeability curve.

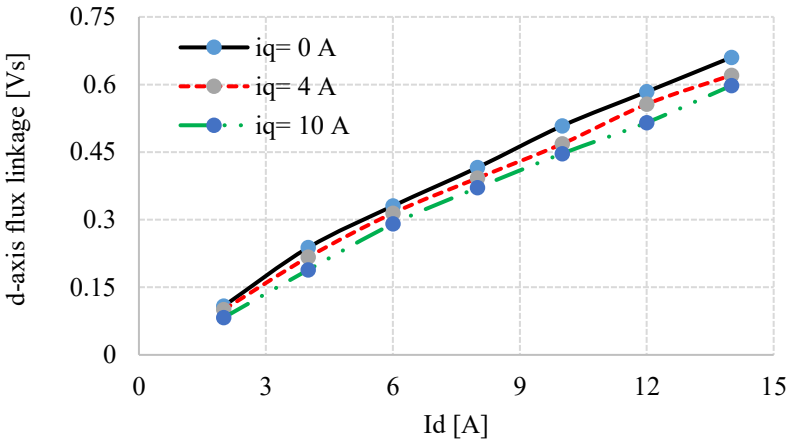

(a)

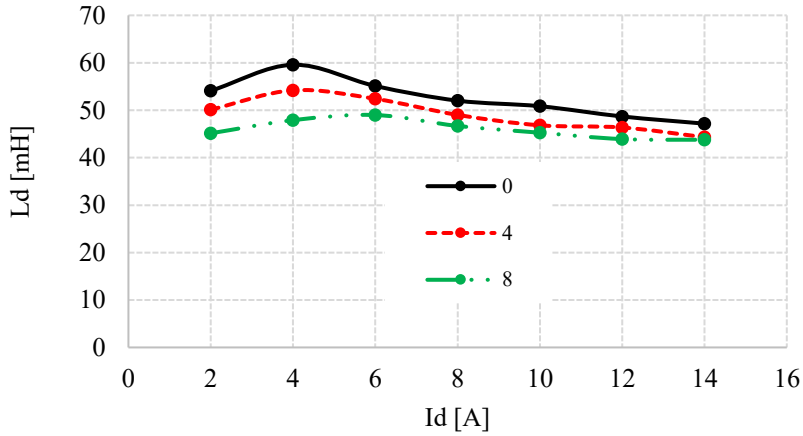

(b)

Fig.4-12. (a) $d-axis$ flux linkage, (b) $d-axis$ inductance for different fixed $q-axis$ current at 100 % MS.

The prototyped VF-PMSM is tangentially magnetized and air barriers are carved to prevent the magnet de-magnetization by the $q-axis$ current. Hence, the $q-axis$ flux path saturates with increased current and the reluctance path increases. This effect can be seen in Fig.4-11. A comparison has been made between the FEA and experimental results for both $dq-axes$ inductance. An error of 2.9 mH in $q-axis$ inductance and error of 1.4 mH in $d-axis$ inductance is observed.

Fig.4-12 shows the experimental results for the $d-axis$ flux linkage and inductance as a function of $d-axis$ current for different fixed $q-axis$ currents at 100 % MS. The $d-$

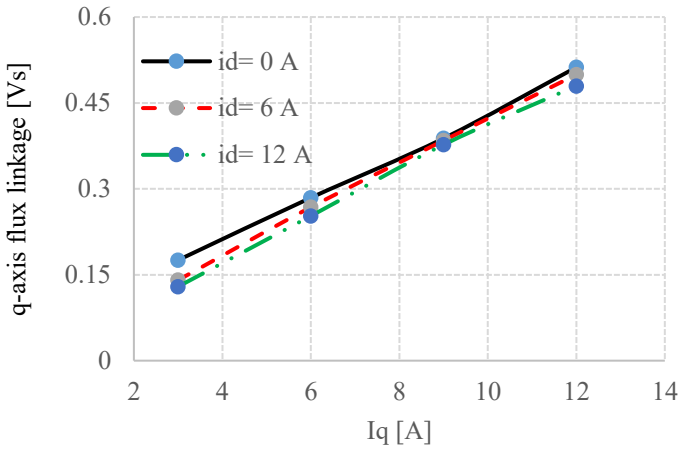

(a)

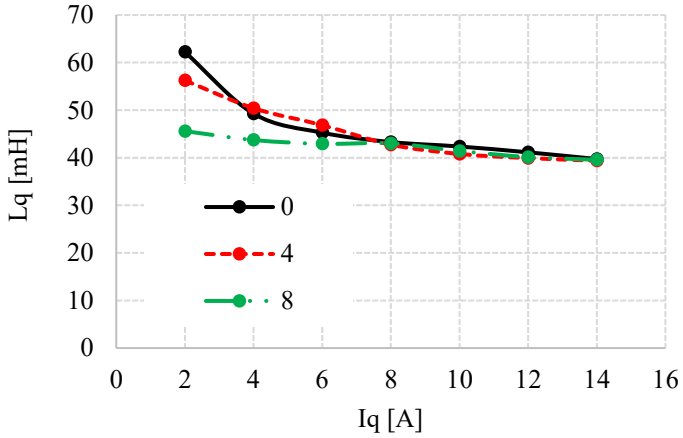

(b)

Fig.4-13. (a) $q-axis$ flux linkage, (b) $q-axis$ inductance for different fixed $d-axis$ current at 100 % MS.

$axis$ flux linkage increases linearly with an increase in the $d-axis$ current. A similar response is observed in the $d-axis$ flux linkage when different constant $q-axis$ currents are applied. The magnitude of flux linkage decreases with an increase in the constant $q-axis$ current. The $d-axis$ inductances as a function of $d-axis$ current are plotted in Fig.4-12 (b) for different constant $q-axis$ currents. Similar waveforms are observed but with reduced magnitude with a higher constant $q-axis$ current.

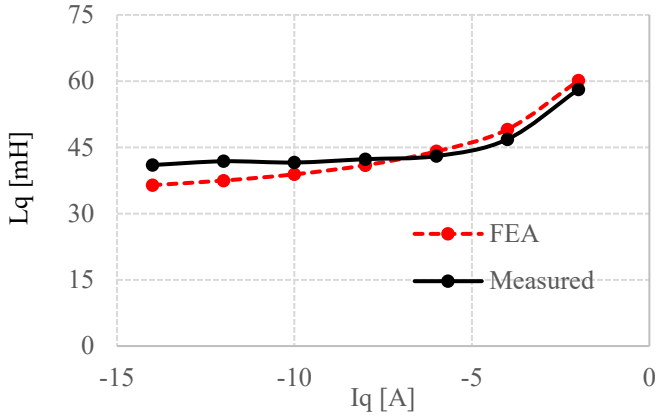

(a)

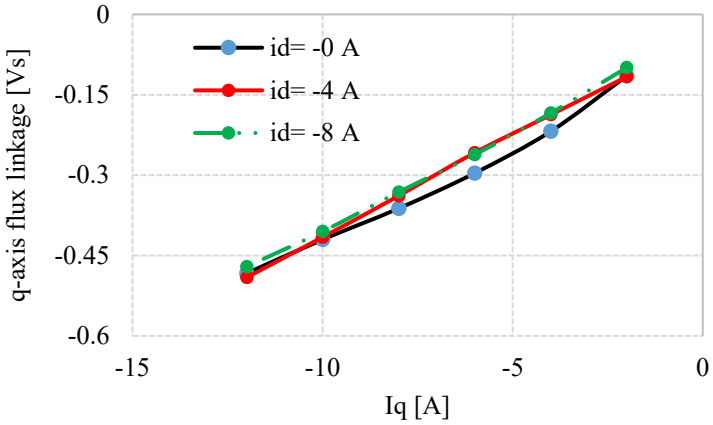

(b)

Fig.4-14. (a) $q-axis$ inductance (b) $q-axis$ flux linkage as a function of negative $q-axis$ current at 100 % MS.

Fig.4-13 shows the experimental results for the $q-axis$ flux linkage and inductance as a function of $q-axis$ current for different constant $d-axis$ currents. It is observed that the $q-axis$ flux linkage increases linearly with an increase in the $q-axis$ current. Similar response is observed in the $q-axis$ flux linkage when different constant $d-axis$ currents are supplied. However, the magnitude of flux linkage decreases with an increase in the constant $d-axis$ current.

Fig.4-14 shows the results for $q-axis$ flux linkage and inductance as a function of negative $q-axis$ current for different fixed $d-axis$ currents. A good correlation is observed between the experimental and FEA results. The $q-axis$ flux linkage for different

negative $d-axis$ currents are plotted in Fig.4-14 (b). The $d-axis$ inductance and flux linkage as a function of negative $d-axis$ current cannot be measured in a VF-PMSM. This is due to the VF-PMSM de-magnetization by the negative $d-axis$ current. For the prototyped machine the demagnetizing current requirement is lower than the machine rated current and the MS change is significant just with a small negative $d-axis$ current. Thus, the same MS cannot be maintained for $d-axis$ parameter measurement as a function of negative $d-axis$ current.

4.4 Summary

The accurate measurement of machine parameters is of prime importance in VF-PMSM drive systems since the machine inductances and flux linkage varies for different MSs. The closed-loop current controller-based flux linkage, inductance and resistance measurements for different MS are conducted. The machine voltage and current response are measured and are processed in real-time. Thus, automated machine parameters without changing the hardware setup are generated in real-time for any given operating condition irrespective of the MS. The experimental results are compared with the finite-element analysis results and show a good correlation.

Chapter 5. Co-simulation Based Electric Vehicle Drive and PWM Loss Analysis

5.1 Introduction

Innovative research papers on the design and performance optimization of VF-PMSMs are reported in the literature every year and more novel topologies will continue to emerge [30]. With the rapid development in new motor topologies and control techniques, validating and testing motor drive system have become important in the design and engineering process [93]. However, physically prototyping the design and testing is a time-consuming process [94]. Thus, a realistic simulation technique is needed to validate the design performance without prototyping the design [95].

Finite element method (FEM) based software provides accurate steady-state results. However, they have limitations in dynamic performance studies. A motor drive system consists of three main parts: motor, power converter, and control. Usually, these parts are designed separately in different software environments.

Conventionally, a mathematical motor model is developed within the control circuit software during the simulation of the drive system, since the designed motor and the control circuits are not in the same software environment. The mathematical motor model may use idealized parameters. However, the motor model with ideal parameters has some major drawbacks: the inductance non-linearities due to magnetic saturation, torque ripple due to motor geometry and spatial harmonics effects are not considered. Consequently, reliable steady and dynamic responses are not achieved. Thus, the conventional simulation approach results in inadequate accuracy [96], [97].

With the advancement in FEM-based software tools, the designs can be dynamically linked with the external drive circuit simulator. The FEM model directly coupled with control simulators in a common co-simulation platform will give higher accuracy results than the conventional simulation approach [98], [99]. Based on published literature, FEA software such as JMAG [100], [101] ANSYS Maxwell [102], Cedrat Flux [103] and

AMESim [104] allows co-simulation with external control software such as MATLAB-Simulink, PSpice and PSIM.

Most motor drive applications are fed by a three-phase PWM inverter to control the current phase and amplitude according to the load and speed requirements. However, the PWM is controlled by a carrier frequency which superimposes carrier harmonics in the basic current waveform. This applies a high-frequency magnetic field to the motor. As a result, high-frequency harmonics are added in the armature currents [105], [106], [107]. The dominant switching harmonics occur at integer multiples of the switching frequency. These harmonics not only cause eddy current loss in the rotor and stator of the motor but also generate torque ripple [108]. The impact of carrier harmonics in motor's operation is vital due to the additional losses in PMs, windings, and iron laminations caused by eddy currents. Hence, an intensive study on the motor losses due to the PWM inverter is necessary.

A comprehensive analysis of PWM power losses in PMSMs with a wide range of PWM switching frequencies has been investigated in [109], [110], [111]. Increasing the PWM frequency helps to suppress the torque ripple in PMSMs. A proper selection of the switching frequency can reduce the magnetic noise due to the PWM inverter [112]. The electric machines inevitably experience a higher iron loss due to the presence of PWM-induced current ripple compared to ideal sinusoidal excitation conditions, accounting for as much as 20%–30% of the total iron loss [113]. Thus, to accurately predict and mitigate these losses during the machine design stage, accurate prediction of the PWM-induced current ripple is important.

The objective of this chapter is to develop a vehicle drive system for the VF-PMSM using a co-simulation platform. Basic ways and steps on coupling the JMAG (FEM software) and MATLAB-Simulink (circuit simulator) are presented. Besides, the comparative effect of the sinusoidal current fed and PWM inverter fed VF-PMSM losses have been studied. The integrative simulation approach determines the motor losses due to the PWM inverter drive system and optimum switching frequency for lower armature current and torque ripple.

5.2 Co-simulation and the VF-PMSM Drive

5.2.1 Co-simulation

Conventionally, during the simulation of the motor drive system, the motor mathematical equations are modeled within the circuit simulator. The mathematical equations of the VF-PMSM in the dq-synchronous rotating reference frame are given as

$$\begin{bmatrix} v_d \\ v_q \end{bmatrix} = R_s \begin{bmatrix} i_d \\ i_q \end{bmatrix} + p \begin{bmatrix} \lambda_d \\ \lambda_q \end{bmatrix} + \omega_e \begin{bmatrix} -\lambda_q \\ \lambda_d \end{bmatrix} \tag{5-1}$$

where v_d, v_q and i_d, i_q are $dq - axes$ armature voltage and current components, respectively. L_d, L_q are $dq - axes$ inductance components. ω_e is the rotor electrical angular velocity and $\lambda_m(i_d)$ is the rotor flux linkage that is a function of the $d - axis$ current. The mathematical equations in (5-1) ignore motor geometry and spatial harmonics effects. λ_d, λ_q are the $dq - axes$ flux linkage and are given as

$$\begin{aligned} \lambda_d &= L_d i_d + \lambda_m(i_d) \\ \lambda_q &= L_q i_q \end{aligned} \tag{5-2}$$

Comparison of the back EMF waveforms obtained from the dq-mathematical model (black), FEA (blue) and experimentally measured (red) are shown in Fig.5-1. The back EMF is shown when the VF-PMSM is running at 1200 rpm and is at 100% MS. The back EMF obtained from the FEM and experiment have harmonics. In contrast, the back EMF obtained from the mathematical model simulation is sinusoidal because it ignores the machine saturation, geometry and spatial harmonics. As a result, the simulation results obtained from the mathematical model will be less accurate than the experimental and FEM results.

Thus, to reduce the errors between the simulation and experimental results, a higher fidelity simulation method called co-simulation is introduced. The co-simulation is the integration and simulation of multiple models, simulated within their own simulation environments, and are communicating at fixed time steps. Integration of an external drive

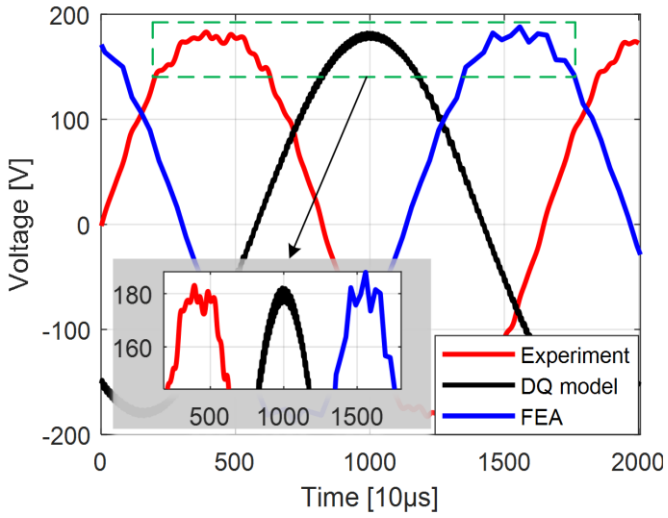

Fig.5-1. Measured and simulated back EMF at 1200 rpm.

system coupled with the FEM model provides a more realistic analysis and control. In this chapter, the power converters and control circuits are designed in MATLAB-Simulink whereas the VF-PMSM is designed in JMAG Designer.

Although the FEM software tool can provide steady-state results for one driving condition, a motor drive system has to be developed to consider both steady-state and transient state performance. Thus, the control circuit required to develop the motor drive system is done in MATLAB-Simulink. Fig.5-2 shows the data flow between the FEM model and circuit simulator that are communicating at the same sampling time. The VF-PMSM is coupled with the MATLAB-Simulink via an S-function block created by the JMAG, JSOL Corporation [114]. A closed-loop system is created between two software tools. The FEM gives the actual motor currents, electromagnetic torque and other motor parameters which are the inputs to the control simulator. Whereas, the control circuit determines the torque angle, and de-magnetization or re-magnetization current based on the reference speed and load torque. The torque angle input to the FEM model is calculated as

$$T_e = T_l + B\omega_e + \mathrm{J}\frac{d\omega_e}{dt} \tag{5-3}$$

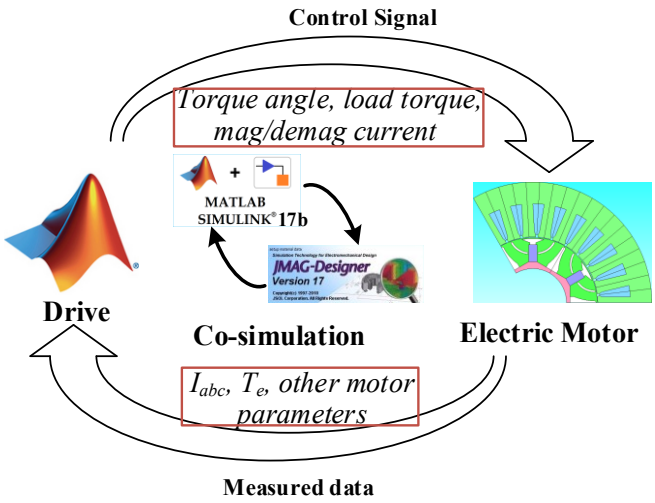

Fig.5-2. Data-flow between two software tools.

where J is the moment of inertia and B is the friction constant, respectively. Solving (5-3), the torque angle is calculated as

$$\iint \frac{d\omega_e}{dt} = \theta \tag{5-4}$$

Similarly, rotor angle can be calculated using mechanical speed (ω_m) and is given as $\omega_e = P\omega_m$, where P is the number of poles pair.

5.2.2 Coupling Methods

JMAG and MATLAB-Simulink can be coupled in two different ways:

5.2.2.1 RT table

It is a behavior table that contains numerical information over a specified range of utilization. The mesh results are stored in RT blocks (lookup tables) for the given current and current angle range. The mesh data includes the machine saturation, geometry and spatial harmonics. The mesh generating process could be longer depending on the user-defined range. However, one-time generated mesh data can be used to analyze the response for all MSs by simply de-magnetizing and re-magnetizing the motor. Since it is separate

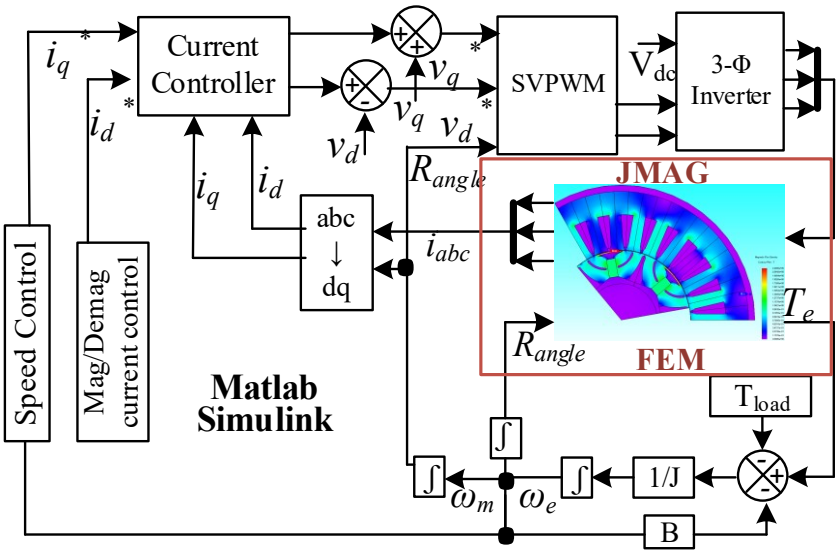

Fig.5-3. Block diagram of the VF-PMSM drive system.

from FEA analysis and only has numerical data, the co-simulation response is fast. However, results might not be as accurate as direct linking because the behavior table provided by this method is calculated by quasi-static calculations and no transient effects are included.

5.2.2.2 Direct link

In this method, the JMAG designer is directly linked with the MATLAB-Simulink. This method gives accurate results for both steady-state and dynamic states. The main advantage of direct simulation over the RT table is that the calculations are fully transient. However, the co-simulation time is longer. This is because for every step of control analysis the FEA calculation has to be performed.

Both RT table and direct link co-simulation methods give high fidelity results since they are based on actual simulation results, not just formulas. e.g. slotting effect, nonlinear behavior of inductance and torque ripple are included.

5.2.2.3 VF-PMSM drives

The VF-PMSM vector controlled drive system in a co-simulation platform is shown in Fig.5-3. The VF-PMSM speed, torque and MS are controlled in a closed-loop system. The

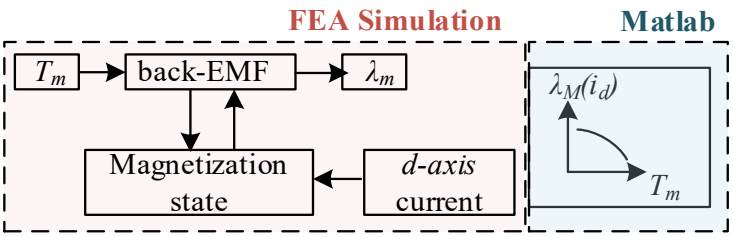

Fig.5-4. Magnet flux linkage estimation process

speed is controlled using a PI controller whereas the MS is manually controlled using the de-magnetization and re-magnetization current pulses based on speed and load requirements. Usually, the MS is reduced by injecting a de-magnetization current pulse when the inverter runs out of voltage. Similarly, the MS is increased by injecting a re-magnetization current pulse when high torque is required. The $d-axis$ and $q-axis$ current references are determined from the speed error and MS requirement, respectively. The control circuit determines the input voltage into the VF-PMSM from the error between the actual current flowing in the VF-PMSM and the current determined by the control circuit.

During co-simulation, in the FEM model, a controlled three-phase voltage is applied to the motor FEM coil. Current determined by the coil impedance and flux flows through the motor. The VF-PMSM inductance and flux-linkage change depending on the current value. For different current values, VF-PMSM parameters are changed because of magnetic saturation and motor geometry. Electromagnetic torque is produced when the current flows through the VF-PMSM coil. Using the generated electromagnetic torque and load torque, the VF-PMSM actual speed and torque angle are determined. Then, the actual motor speed and currents from the FEM model are given to the control unit. Thus, a complete data flow occurs in a closed-loop system between the FEM model and control circuit. Because of this communication, all parameters, including current and voltage in the control unit account for the spatial magnetic saturation and slotting effect.

5.2.2.4 Magnet flux linkage estimation

The co-simulation based drive systems have been studied mostly in PMSMs and IMs where the magnet flux linkage (λ_m) is a constant value unless the field weakening algorithm

is applied. However, λ_m in the VF-PMSM varies with changes in the MSs. The S-function block which links the FEM and MATLAB does not include the variable λ_m signal output but includes the magnet temperature (T_m) input. Thus, to consider different MSs, a λ_m estimation technique is developed. First, the FEM simulation is carried to develop a relationship between T_m and the machine back EMF. With an increase in the magnet temperature, the back EMF decreases. Then, λ_m is calculated from the speed and back EMF. Similarly, FEM simulation is carried out to develop a relationship between the de-magnetization and re-magnetization current and corresponding back EMF. The back-EMF due to different T_m and de-magnetization and re-magnetization currents are compared to generate T_m vs. $\lambda_m(i_d)$ a lookup table in MATLAB as shown in Fig.5-4.

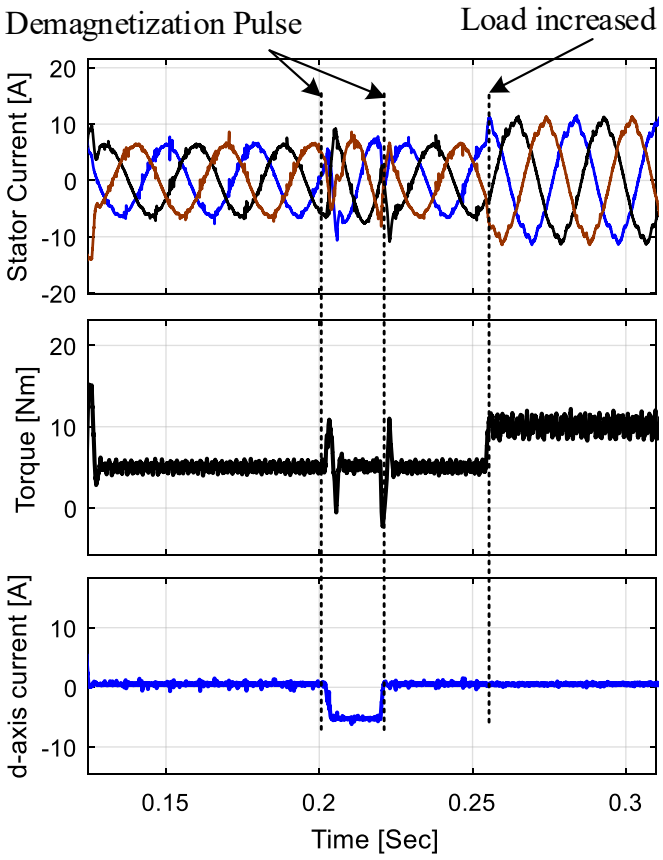

Fig.5-5. Co-simulation results for the direct link method.

5.3 Results and Discussion

Fig.5-5 shows the co-simulation results using the direct method. Stator current, torque and $d-axis$ current are shown when the motor is running at rated speed with a load of 5 N.m. At 0.2 sec a de-magnetization current pulse is applied. The load is increased to 10 N.m at 0.255 sec. In the direct link co-simulation method, the FEA calculation needs to be performed for every step of circuit/control analysis. Thus, this results in a very long co-simulation time. With the system configuration of 16 GB RAM, i7-6700 CPU @3.40GHz processor, it took 47 hours to simulate the VF-PMSM model for 0.5 sec.

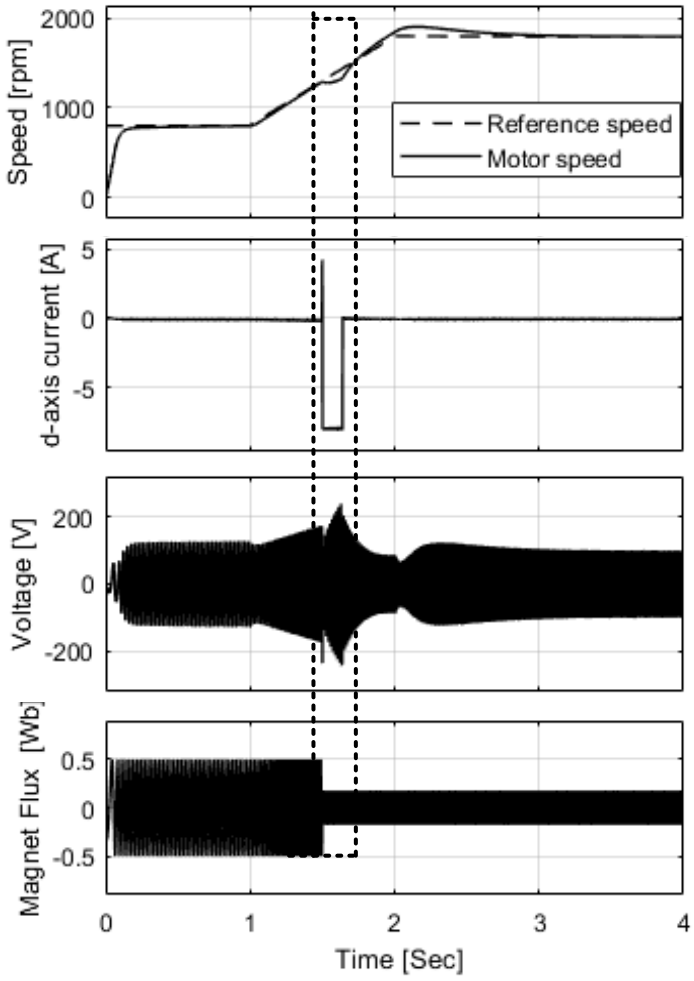

Fig.5-6. Simulation results showing the VF-PMSM working principle using the RT table based co-simulation.

Fig.5-6 presents the operating principle of the VF-PMSM co-simulation using the RT table method. Initially, the VF-PMSM is running at 900 rpm and is at 100% MS. The speed is increased to 1800 rpm by a ramp speed command at 1 sec. However, as the speed increases above the base speed, the terminal voltage tends to exceed the machine voltage limit. Thus, a de-magnetization current pulse is supplied at the rated speed. A de-magnetization current pulse of 8A decreases the MS to 37%. The decrease in MS allows the machine to run safely at a higher speed.

The zoomed co-simulation results during the de-magnetization pulse are shown in Fig.5-7. The de-magnetization pulse shows a small effect on the machine speed but once the pulse is removed the machine speed follows the reference command. Similarly, the VF-

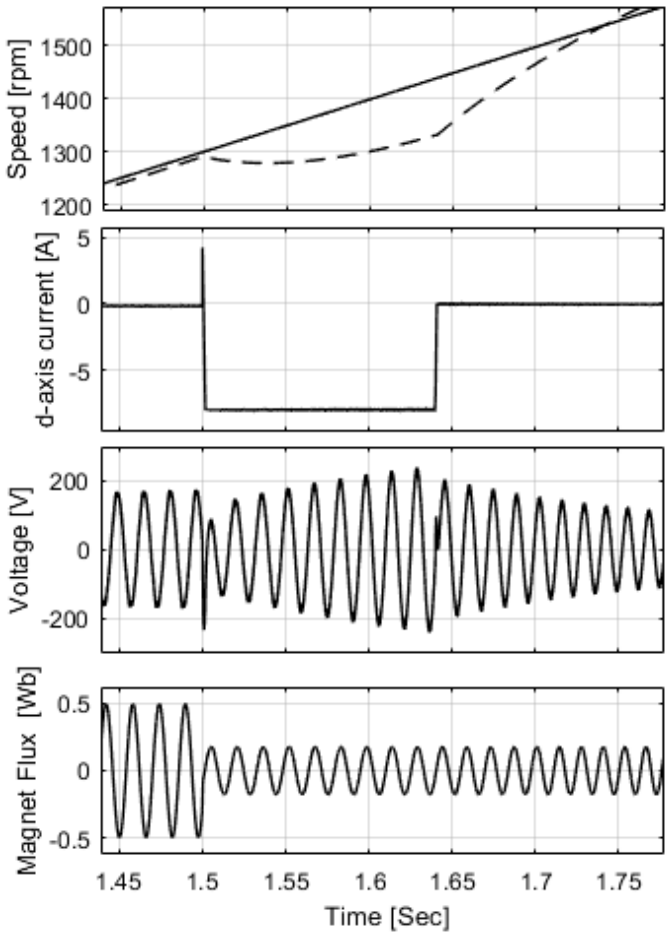

Fig.5-7. Zoomed simulation results during de-magnetization based on co-simulation.

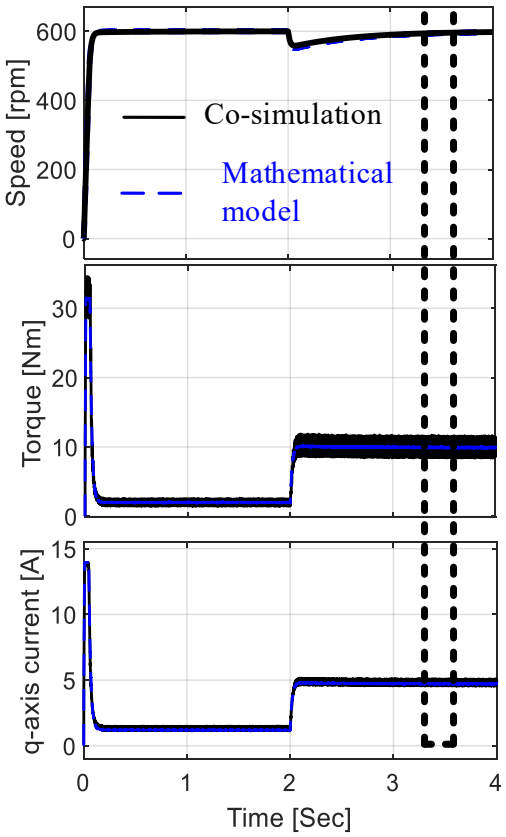

Fig.5-8. Simulation results showing the comparison between the dq-mathematical model (blue) and co-simulation (black).

PMSM can be re-magnetized to the desired MS by the $d-axis$ current pulse depending on the driving requirements.

Fig.5-8 shows the comparison between the dq-mathematical model (dotted blue) and co-simulation (solid black) results. The VF-PMSM is driven at a constant speed of 600 rpm at 100% MS. At 2 sec the initial load torque of 1 N.m is increased to 10 N.m. The response of speed, torque, and $q-axis$ current are shown. The zoomed results during the steady-state between 3.4 sec to 3.44 sec are also shown in Fig.5-9. Due to the machine geometry and spatial harmonic effects, a higher ripple is observed in speed, torque and current in the co-simulation results.

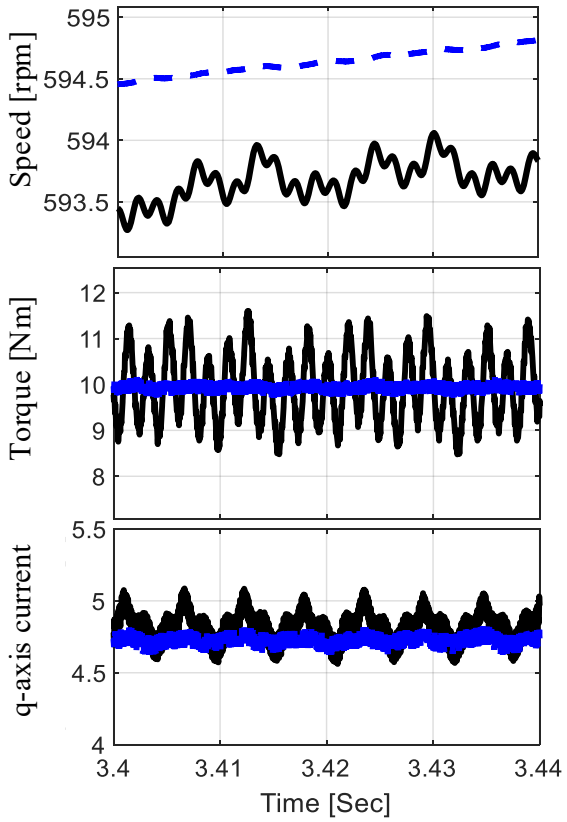

Fig.5-9. Zoomed simulation results showing the comparison between the dq-mathematical model (blue) and co-simulation (black).

Fig.5-10 shows the dynamic state results comparison between the experimental and co-simulation results. It also describes the working principles of VF-PMSMs during transients explaining how the current pulse can change the MS. It is observed that the speed and current have a higher ripple than the co-simulation. This is due to the nonideal sensors and power electronics devices in addition to the machine vibration and its effect on the optical encoder. However, the magnet flux linkage in the experiment has an abrupt response. This is because a lookup table based method is used to determine the λ_m in the experiment due to the unavailability of flux transducers and difficulty in placement inside the motor due to limited space. Thus, a lookup table is made based on the de-magnetization and re- magnetization current and MS. The no-load flux linkage can be estimated from the measured open-circuit voltage (V_p) as

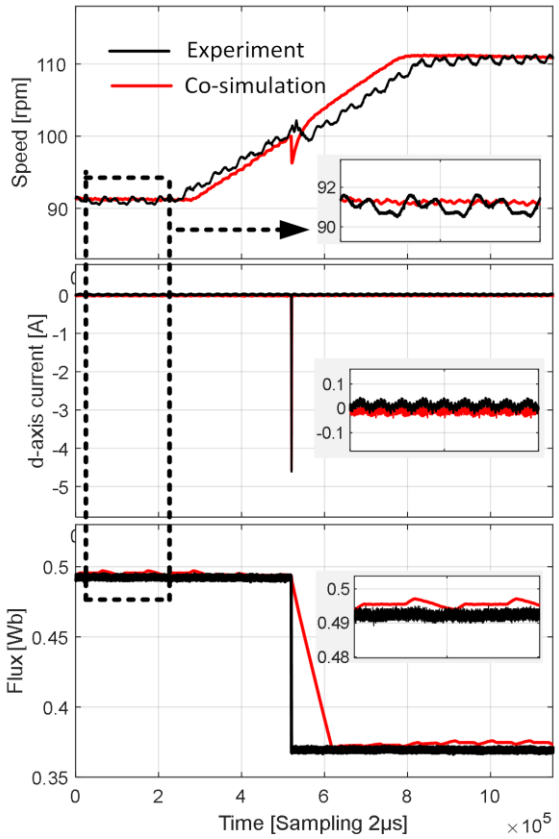

Fig.5-10. Comparison between the experimental and co-simulation results.

$$\lambda_m = \frac{\sqrt{2}V_p}{\omega_e} \tag{5-5}$$

Fig.5-11 shows the comparison of torque waveforms between co-simulation and experiment for 100% MS and 75% MS. Similar torque waveforms are achieved between the co-simulation and experiment. A smooth torque waveform is seen in the experimental result because of the filter used in the torque transducer unit.

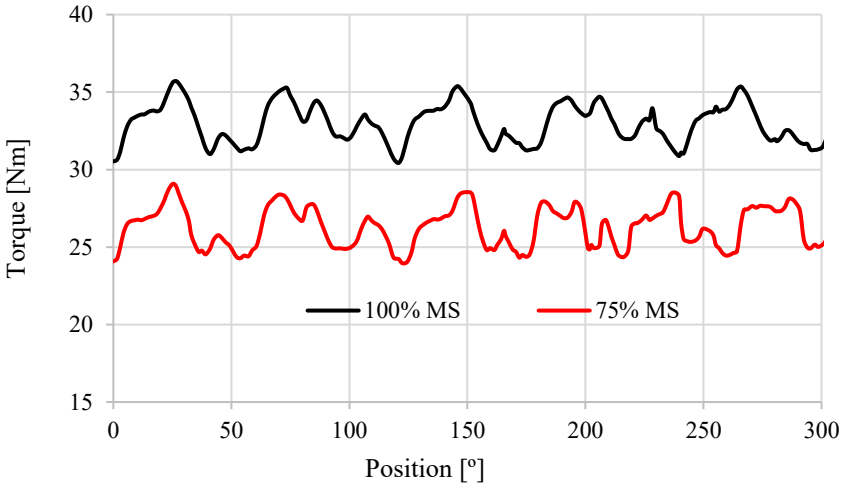

(a)

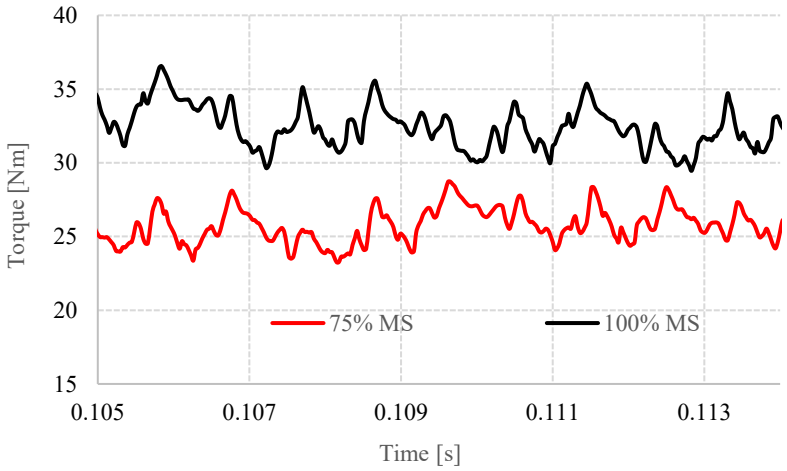

(b)

Fig.5-11. Comparison of torque waveforms for different MSs (a) Experiment (b) co-simulation.

5.4 Iron Loss Analysis

The vector controlled drive using a PWM control technique is a widely accepted control method for the synchronous motor drive system. The PWM-controlled drive system allows controlling the current phase and amplitude according to the load and speed requirements. However, PWM is controlled by a carrier frequency which superimposes carrier harmonic in the basic current waveform. This applies a high-frequency magnetic field to the motor. As a result, an additional iron loss is generated in the rotor and stator of the motor. Thus, an intensive study on the motor losses due to the PWM inverter is necessary.

Fig.5-12 shows the steps to measure the motor's PWM losses. A transient magnetic field analysis model (torque model) is created in FEM software allowing external circuit control. A direct link is created and simulated by linking the torque model and the circuit simulator. Time history data of the magnetic analysis is stored and imported into the torque model. Then, the iron loss analysis model is created for the torque model and loss results are obtained.

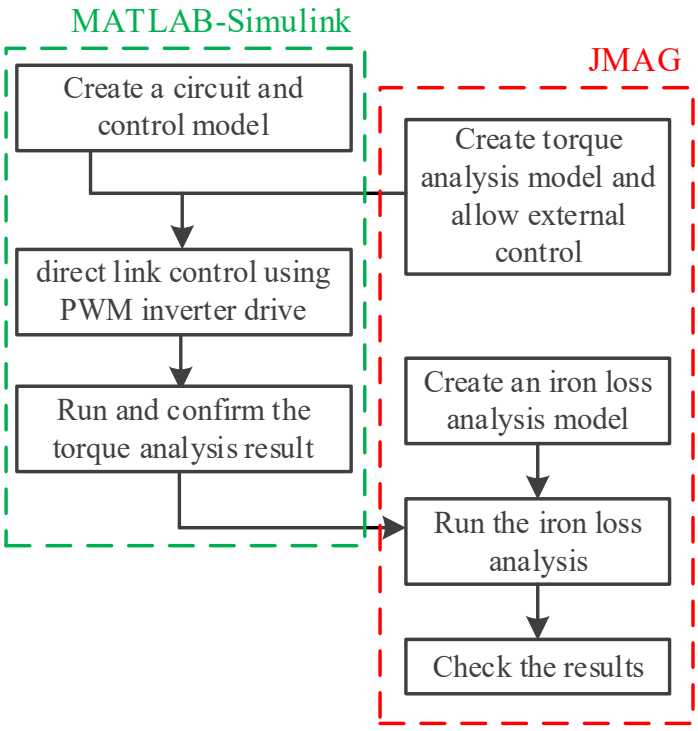

Fig.5-12. Steps to measure the motor's PWM losses.

Table 5-1 Loss analysis results

	Rotor core		Stator core	
	SINE current drive	PWM drive	SINE current drive	PWM drive
Iron	0.78 W	6.93 W	14.34 W	18.97 W
Hysteresis	0.22 W	0.49 W	10.22 W	10.99 W
Eddy	0.56 W	6.43 W	4.12 W	7.98 W

Table 5-1 shows the comparison of the iron loss, hysteresis loss and eddy current loss when the VF-PMSM is driven by a sinusoidal current and PWM inverter at 1100 rpm and producing 1 N.m torque. The iron loss increases both in the rotor core and the stator core when the VF-PMSM is run using a 5 kHz inverter. It is observed that the hysteresis loss is not affected while the eddy current loss significantly increased when the VF-PMSM is run by the PWM inverter.

The eddy current loss density distribution of the VF-PMSM rotor core has been shown in Fig.5-13. The eddy current loss is concentrated most in the $q-axis$ flux path and the loss intensity is much higher when the VF-PMSM is run by a PWM inverter.

The impact of carrier harmonics in the motor's operation is vital due to the considerable additional losses caused by eddy currents. Fig.5-14 shows the comparison of rotor eddy current loss frequency component when the VF-PMSM is driven by a sinusoidal current and PWM inverter at 5 kHz. The fundamental component is almost the same for both SINE and PWM inverter-fed VF-PMSM. The fundament frequency is 55 Hz for the stator core and 495 for the rotor core. The rotor core fundamental frequency is determined from the VF-PMSM geometry and calculated as the cross of slot harmonics (lowest frequency for a rotor) and the rotational speed.

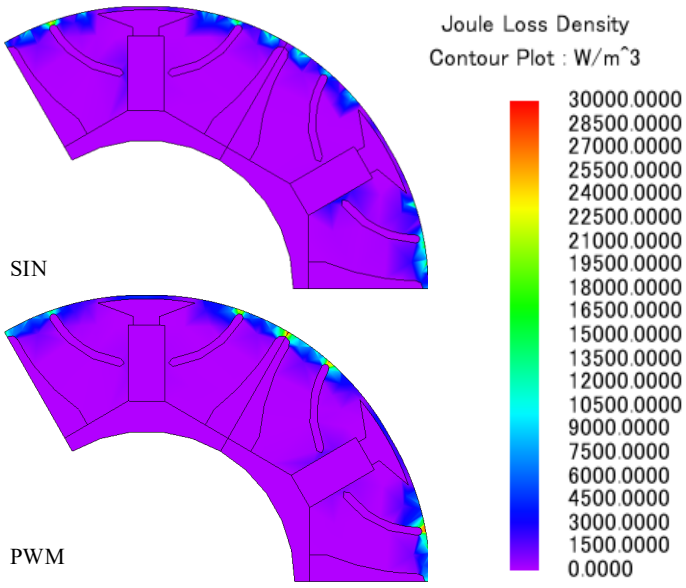

Fig.5-13. Eddy current loss density distribution of the rotor core.

Fig.5-15 shows the comparison of stator eddy current loss frequency component when the VF-PMSM is driven by a sinusoidal current and PWM inverter at 5 kHz.It is observed that additional losses are generated when the VF-PMSM is run by the PWM inverter. The

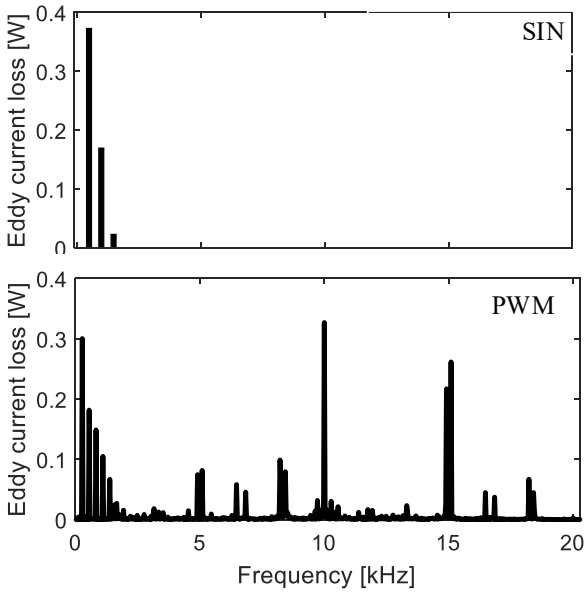

Fig.5-14. Rotor eddy current loss frequency component.

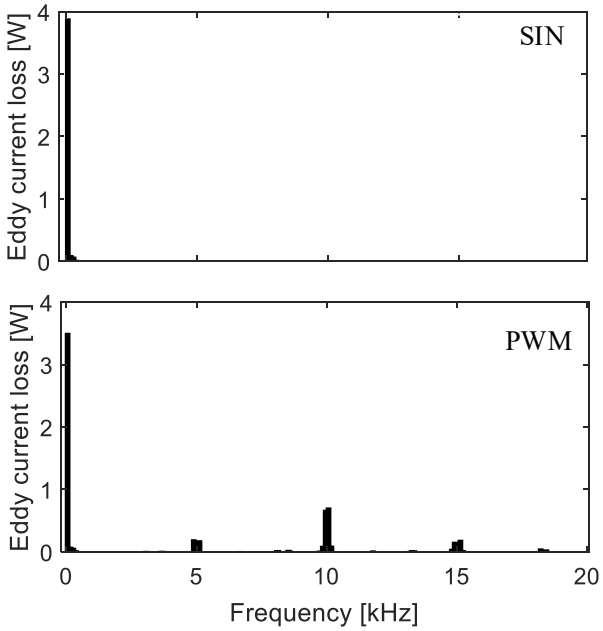

Fig.5-15. Stator eddy current loss frequency component.

harmonics are observed at integer multiples of the PWM switching frequency and is given by

$$f = nSF \pm m \tag{5-6}$$

where n and m are integers. If n is odd, m is 2 and if n is even, m is 1.

Table 5-2 shows the comparison results of the iron loss due to SINE current and PWM inverter drive for different speeds. With the increase in the frequency, iron loss also increases. The iron loss due to the PWM inverter increases by 74.4% at 900 rpm and 71.13% at 1100rpm compared to the SIN current drive.

With different switching frequencies, the harmonics change in the current and thus, the iron loss also varies. Table 5-3 shows the iron loss analysis results for different switching frequencies. By increasing the switching frequency, the current will have a lower harmonic distortion factor due to the higher reactance of the motor for the carrier frequencies. Thus, the lower harmonic flux density is distributed in the motor with a higher switching frequency.

Table 5-2 Loss analysis results for different speeds.

Speed [RPM]	Current [A]	Iron loss [W]	
		SINE current drive	PWM drive
1100	2.86	15.13	25.90
900	2.5	11.59	20.22
700	2.06	80.09	16.19
500	1.9	5.26	10.58
300	1.65	2.70	6.9

Table 5-3 Loss analysis results for different switching frequencies.

Switching Frequency [kHz]	Frequency [Hz]	Iron loss [W]	THD [%]
2.5	30.3	20.86	3.36
5	30.69	19.64	2.87
7.5	30.67	18.94	2.85

Fig.5-16 shows the comparison between co-simulation (red) and FEM (black) results. In the co-simulation results, ripples are present in the speed waveform. The magnitudes of the switching frequency components generated by the inverter are lower in the current than they are in the voltage waveforms due to the low pass characteristic of an electric machine. However, the spatial harmonics are generated inside the machine and are therefore stronger in the current than they are in the voltage waveforms. Thus, harmonics are present in the current waveform during co-simulation. The torque waveforms show a good correlation between the FEM and co-simulation results.

Torque ripple results in periodic oscillations in the speed response, which reduces the accuracy of the control system [115], [116]. The torque ripple is mainly affected by current

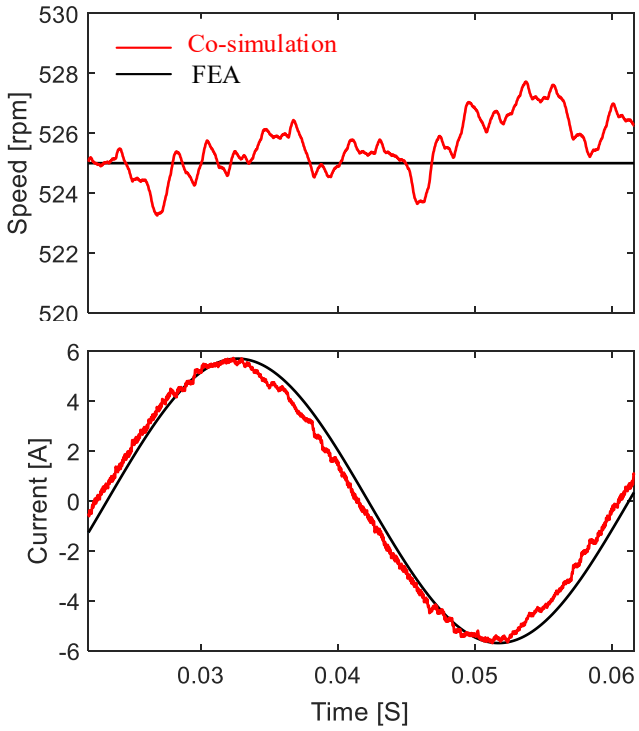

Fig.5-16. Comparison between co-simulation and FEA for speed, current and torque waveform when the motor is running at 525 rpm and 5N.m torque.

harmonics which produce torque harmonics. The higher THD in the armature current significantly increases the magnetic saturation in the stator, enhancing the torque ripple. Thus, by increasing the switching frequency, torque ripple is reduced.

Fig.5-17 shows the comparison between co-simulation and FEA for torque when the motor is running at 525 rpm and 5N.m torque. The torque waveform during the co-simulation has more ripple than the FEA-generated torque waveform.

Fig.5-18 and Fig.5-19 show the current and torque waveforms for different switching frequencies. The current THD is 3.36% at 2.5 kHz and 2.85% at 7.5kHz. The torque ripple of 30.68% is reduced to 26.94% by increasing the switching frequency from 2.5 kHz to 7.5kHz.

Increasing the carrier frequency reduces the motor's PWM losses but the inverter loss increases. To determine the power loss of the inverter, conduction and switching losses in

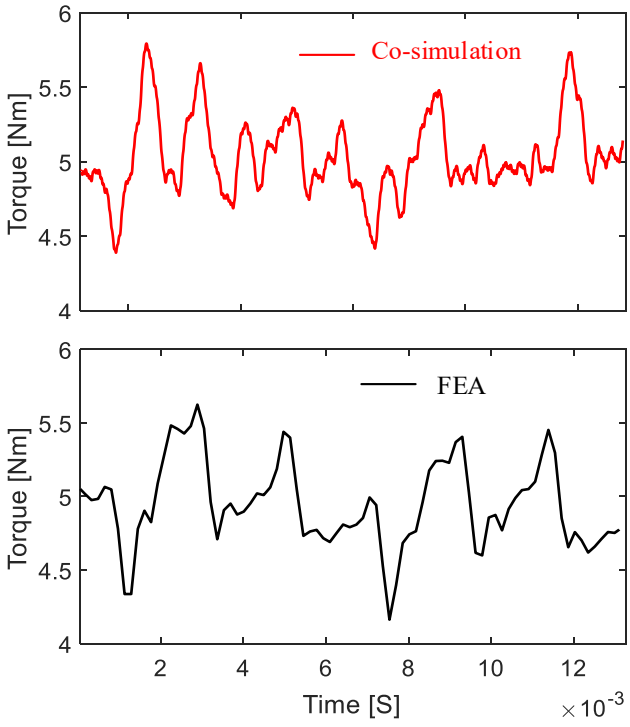

Fig.5-17. Comparison between co-simulation and FEA for torque when the motor is running at 525 rpm and 5N.m torque.

the inverter have to be considered. Thus, for the best drive performance, both the motor's PWM losses and inverter losses have to be considered to determine the optimum switching frequency in terms of both efficiency and torque ripple.

5.5 Summary

This chapter presents an electric vehicle motor drive system and loss analysis due to pulse-width modulation (PWM) inverter drive for a variable flux-permanent magnet synchronous machine (VF-PMSM) using a co-simulation platform. A pair of software tools: finite element method (FEM) based software, which allows computing the electromagnetic behavior and MATLAB, which allows the dynamic simulation of the control circuit and power converters are coupled to develop the VF-PMSM drive. Such an integrative simulation approach gives higher fidelity results since it includes magnetic saturation (inductance nonlinearities), machine geometry (torque ripple and spatial harmonics) effects.

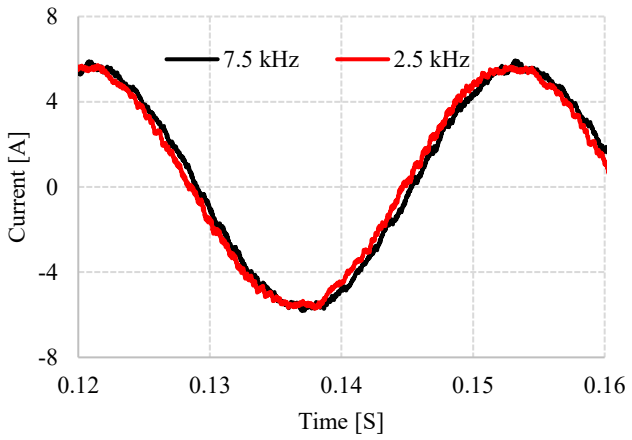

Fig.5-18. The current waveform for different switching frequencies.

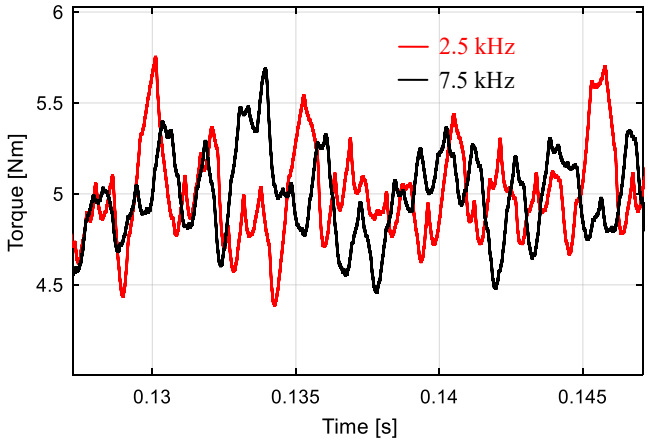

Fig.5-19. Torque waveform for different switching frequencies.

A comparison between sinusoidal current and PWM inverter-fed VF-PMSM's losses have been studied. The PWM inverter superimposes carrier harmonics in the basic current waveform and applies a high-frequency magnetic field to the motor. As a result, iron losses are generated in the rotor and stator of the motor. Since an additional loss due to the PWM inverter has to be considered in high-efficiency motors in the design phase, the impact of different switching frequencies in motor loss, terminal current and torque ripple are investigated. The co-simulation results are validated with conventional simulation (dq-

mathematical model), FEM and experimental results, illustrating that the higher the switching frequency the lower the motor loss and torque ripple.

Chapter 6. Conclusions and Future Works

6.1 Conclusions

In chapter 1, the requirements of an electric motor for traction applications are explained. The advantages and disadvantages of PMSMs are presented. The introduction of VF-PMSMs and how they can overcome the drawbacks of PMSMs are explained. The magnetization state change in a LCF magnet due to magnetization and de-magnetization pulses is presented. The prototyped machine specifications and dimensions used for the simulation, FEM analysis and experiment are presented. The objectives of this research work were presented which is to model, analyze and control the VF-PMSM.

In chapter 2, the effect of different magnetizing pulse widths on the machine back-EMF and no-load losses are analyzed. A nonlinear adaptive filter that can extract time and frequency varying sinusoidal signals from a nonstationary waveform is used to estimate the back-EMF during the motoring mode. It is observed that the higher the pulse width, the higher the losses but the back-EMF quality is improved. Although the locked rotor magnetizing process is redundant, lower THD in back-EMF is observed than other magnetizing methods. It is seen that the minimum magnetizing pulse width to magnetize the VF-PMSM 100% is experimentally determined to be 10 ms with a fixed DC bus of 400 V.

In chapter 3, the effect of the de-magnetization and re-magnetization pulse on the torque is analyzed. The $d-axis$ pulse used to change the MS abruptly changes the magnet flux linkage changing the magnet torque, as well as the reluctance torque. Thus, a pulsating torque is created. Since the remagnetizing current amplitude is much higher than the de-magnetization current, pulsating torque is severe during re-magnetization. The $q-axis$ current reference determined by the voltage limit method and the load torque method reduces the pulsating effect during re-magnetization.

In chapter 4, the closed-loop current controller-based parameter measurement for different MSs are conducted. The machine voltage and current response are measured and are processed in real-time to measure the flux linkage, inductance and resistance for different MSs. Automatic machine parameter maps are generated in real-time for different MSs without

changing hardware setup. Experimental results are compared with the finite-element analysis results and show a good correlation.

In chapter 5, a realistic simulation approach using the co-simulation platform for an electric motor drive system is presented. This integrated simulation approach will be useful to test the dynamic behavior and loss analysis of any electrified transportation by coupling the FEM model with a control/circuit simulator. The FEM-based VF-PMSM co-simulation drive system gives higher fidelity results than the conventional simulation approach since they use the actual FEA model, which includes the inductance non-linearities, magnetic saturation and spatial harmonic effects. The inverter-fed VF-PMSM drive system superimposes carrier harmonics in the basic current waveform and applies a high-frequency magnetic field to the motor which significantly increases the iron loss in the motor. The iron loss due to the PWM inverter increased by 74.4% at 900 rpm compared to the SINE current drive. The increase in the iron loss is dominated by the eddy current loss due to the high-frequency magnetic field. The impact of different switching frequencies in motor loss, armature current and torque ripple are investigated. The results show that the higher the switching frequency the lower the motor loss and torque ripple.

6.2 Future Works

1. Model an AlNiCo-based VF-PMSM with a lower magnetizing current than the machine-rated current.
2. Study the torque ripple and cogging torque considering the back EMF harmonics.
3. Develop a more precise MS estimator without requiring coupling with a dynamometer.
4. Develop a more effective algorithm to control the torque pulsation during the MS change.

References

[1] "The Current State of Electric Vehicle Subsidies: Economic, Environmental, and Distributional Impacts," strata.org, October 2017. [Online]. Available: https://strata.org/pdf/2017/ev-full.pdf. [Accessed August 2019].

[2] "Auto & Mobility Trends in 2019," CB Insights Research., [Online]. Available: https://www.cbinsights.com/research/report/auto-mobility-trends-2019/. [Accessed Retrieved 28 March 2019].

[3] Z. Q. Zhu and D. Howe, "Electrical machines and drives for electric, hybrid,and fuel cell vehicles," *Proceeding of IEEE,* vol. 95, no. 4, pp. 746-765, April 2007.

[4] Z. Q. Zhu, W. Q. Chu and Y. Guan, "Quantitative comparison of electromagnetic performance of electrical machines for HEVs/EVs," *CES Transactions on Electrical Machines and Systems,* vol. 1, no. 1, pp. 37-47, March 2017.

[5] J. Santiago, H. Bernhoff, B. Ekergård, S. Eriksson, S.Ferhatovic, R. Waters and M. Leijon, "Electrical motor drivelines in commercial all-electric vehicles: a review," *IEEE Trans. on Vehicular Technology,* vol. 61, no. 2, p. 475–484, Feb. 2012.

[6] M. Ehsani, K. M. Rahman and H. A. Toliyat, "Propulsion system design of electric and hybrid vehicles," *IEEE Trans. Ind. Electron.,* vol. 44, no. 1, pp. 19-27, Feb. 1997.

[7] T. M. Jahns, G. Kliman and T. Neumann, "Interior permanent-magnet synchronous motors for adjustable-speed drives," *IEEE Trans. Ind. Appl.,* Vols. IA-22, no. 4, pp. 738-747, Jul./Aug. 1986..

[8] C. Jo, J. Y. Seol and I. J. Ha, "Flux-weakening control of IPM motors with significant effect of magnetic saturation and stator resistance," *IEEE Trans. Ind. Electron. ,* vol. 55, no. 3, p. 1330–1340, Mar. 2008.

[9] L. Sepulchre, M. Fadel, M. Pietrzak-David and G. Porte, "MTPV Flux-Weakening Strategy for PMSM High Speed Drive," *IEEE Trans. Ind. App.,* vol. 54, no. 6, pp. 6081-6089, Nov.-Dec. 2018.

[10] I. Petrov, M. Niemelä, P. Ponomarev and J. Pyrhönen, "Rotor Surface Ferrite Permanent Magnets in Electrical Machines: Advantages and Limitations," *IEEE Trans. Ind. Electron,* vol. 64, no. 7, pp. 5314-5322, July 2017.

[11] M. Ibrahim, L. Masisi and P. Pillay, "Design of Variable Flux Permanent-Magnet Machine for Reduced Inverter Rating," *IEEE Trans. Ind. Appl.,* vol. 51, no. 5, pp. 3666-3674, Sept.-Oct. 2015.

[12] J. Chen, J. Li and R. Qu, "Maximum-Torque-per-Ampere and Magnetization-State Control of a Variable-Flux Permanent Magnet Machine," *IEEE Trans. Ind. Electron.,* vol. 65, no. 2, pp. 1158-1169, Feb. 2018.

[13] C. Desai and P. Pillay, "Back EMF, Torque–Angle, and Core Loss Characterization of a Variable-Flux Permanent-Magnet Machine," *IEEE Trans. Transp. Electrific.,* vol. 5, no. 2, pp. 371-384, June 2019.

[14] M. J. Kramer, R. W. McCallum, I. A. Anderson and S. Constantinides, "Prospects for non-rare earth permanent magnets for traction motors and generators," *JOM,* vol. 64, pp. 752-763, Jul. 2012.

[15] V. Ostovic, "Memory motors," *IEEE Ind. Appl. Mag.,* vol. 9, no. 1, pp. 52-61, Jan./Feb. 2003.

[16] V. Ostovic, "Memory motors-a newclass of controllable flux PM machines for a true wide speed operation," *Proc. 36th IEEE Ind. Appl. Conf. Rec. IAS Annu. Meeting,* vol. 4, Sep./Oct. 2001.

[17] H. Liu, H. Lin, S. Fang and Z. Q. Zhu, "Permanent magnet demagnetization physics of a variable flux memory motor," *IEEE Trans. Magn.,* vol. 45, no. 10, p. 4736–4739, Oct. 2009.

[18] J. Chen, J. Li and R. Qu, "Analysis, Modeling, and Current Trajectory Control of Magnetization State Manipulation in Variable-Flux Permanent Magnet Machines," *IEEE Trans. Indl. Electron.,* vol. 66, no. 7, pp. 5133-5143, July 2019.

[19] J. Kim, J. Choi, K. Lee and S. Lee, "Design and analysis of surface-mounted type variable flux permanent magnet motor for wide-speed range applications," *IEEE Trans. Magn.,* vol. 51, no. 11, Nov. 2015.

[20] R. Jayarajan, N. Fernando and I. U. Nutkani, "A Review on Variable Flux Machine Technology: Topologies, Control Strategies and Magnetic Materials," *IEEE Access,* vol. 7, pp. 70141-70156, 2019.

[21] A. M. Aljehaimi, "A Rotor Flux Linkage Estimator and Operating Envelopes of a Variable-Flux IPM Synchronous Machine," *Ph.D. dissertation, Dept. of Electrical and Computer Engineering, Concordia University, montreal, QC, Canada,,* 2018.

[22] K. S. Amitkumar, R. Thike and P. Pillay, "Linear Amplifier-Based Power-Hardware-in-the-Loop Emulation of a Variable Flux Machine," *IEEE Transactions on Industry Applications,* vol. 55, no. 5, pp. 4624-4632, Sept.-Oct. 2019.

[23] A. Takbash, "Modeling and Design Optimization of Permanent Magnet Variable Flux Machines," *Ph.D. dissertation, Dept. of Electrical and Computer Engineering, Concordia University, montreal, QC, Canada,* 2018.

[24] N. Limsuwan, T. Kato, K. Akatsu and R. Lorenz, "Design and evaluation of a variable-flux flux-intensifying interior permanent magnet machine," *IEEE Trans. Ind. Appl,* vol. 50, no. 2, pp. 1015-1024, Mar./Apr. 2014.

[25] B. S. Gagas, K. Sasaki, T. Fukushige, A. Athavale, T. Kato and R. D. Lorenz, "Analysis of magnetizing trajectories for variable flux PM synchronous machines considering voltage, high-

speed capability, torque ripple, and time duration," *IEEE Trans. Ind. Appl.,* vol. 52, no. 5, p. 4029–4038, Sep./Oct. 2016.

[26] Y. Zhou, Y. Chen and J. X. Shen, "Analysis and improvement of a hybrid permanent magnet memory motor," *IEEE Trans. Energy Convers.,* vol. 31, no. 3, p. 915–923, Sep. 2016.

[27] C. Yu and K. T. Chau, "Design, analysis, and control of DC-excited memory motors," *IEEE Trans. Energy Convers.,* vol. 26, no. 2, pp. 479-489, Jun. 2011.

[28] X. Zhu, Z. Xiang, L. Quan, W. Wu and Y. Du, "Multimode optimization design methodology for a flux-controllable stator permanent magnet memory motor considering driving cycles," *IEEE Trans. Ind. Electron.,* vol. 65, no. 7.

[29] H. Yang, H. Lin, E. Zhuang, S. Fang and Y. Huang, "Investigation of design methodology for non-rare-earth variable-flux switched flux memory machines," *IET Electr. Power Appl.,* vol. 10, no. 8, pp. 744-756, Sep. 2016.

[30] H. Yang, H. Lin and Z. Q. Zhu, "Recent advances in variable flux memory machines for traction applications: A review," *CES Transactions on Electrical Machines and Systems,* vol. 2, no. 1, pp. 34-50, March 2018.

[31] G. Qiao, M. Wang, F. Liu, Y. Liu and P. Zhen, "Analysis of Novel Hybrid-PM Variable-Flux PMSMs with Series-Parallel Magnetic Circuits," *IEEE Trans. Magn.,* Early access.

[32] H. Yang, Z. Q. Zhu, H. Lin and S. Lyu, "Comparative Study of Hybrid PM Memory Machines Having Single- and Dual-Stator Configurations," *IEEE Trans. Ind. Electron.,* vol. 65, no. 11, pp. 9168-9178, Nov. 2018.

[33] H. Yang and e. al, "Stepwise Magnetization Control Strategy for DC-Magnetized Memory Machine," *IEEE Trans. Ind. Electron.,* vol. 66, no. 6, pp. 4273-4285, June 2019.

[34] R. Imamura, T. Wu and R. D. Lorenz, "Design of Variable Magnetization Pattern Machines for Dynamic Changes in the Back EMF Waveform," *IEEE Trans. Ind. Appl.,* vol. 55, no. 4, pp. 3469-3478, July-Aug. 2019.

[35] H. Yang, S. Lyu, H. Lin, Z. Q. Zhu, H. Zheng and T. Wang, "A Novel Hybrid-Magnetic-Circuit Variable Flux Memory Machine," *IEEE Tran. Ind. Electron.,* Early Access, 2019.

[36] A. Athavale, D. J. Erato and R. D. Lorenz, "Enabling Driving Cycle Loss Reduction in Variable Flux PMSMs Via Closed-Loop Magnetization State Control," *IEEE Trans. Ind. Appl.,* vol. 54, no. 4, p. 3350–3359, Jul. 2018.

[37] T. Fukushige, N. Limsuwan, T. Kato, K. Akatsu and R. D. Lorenz, "Efficiency contours and loss minimization over a driving cycle of a variable flux-intensifying machine," *IEEE Trans. Ind. Appl.,* vol. 51, no. 4, pp. 2984-2989, Jul./Aug. 2015.

[38] A. Sun, J. Li, R. Qu, J. Chen and H. Lu, "Rotor design considerations for a variable-flux flux-intensifying interior permanent magnet machine with improved torque quality and reduced magnetization current," *Proc. IEEE Energy Convers. Congr. Expo.,* pp. 784-790, Sep. 2015.

[39] Y. Hu, J. Chen, R. Qu, B. Chen, Y. Xiao and X. Li, "Closed-Loop Magnetization State Control for a Variable-Flux Memory Machine," *IEEE Access,* vol. 8, pp. 146983-146993, 2020.

[40] G. Qiao, M. Wang, F. Liu, Y. Liu, P. Zheng and Y. Sui, "Analysis of Magnetic Properties of AlNiCo and Magnetization State Estimation in Variable-Flux PMSMs," *IEEE Trans. Mag.,* vol. 55, no. 7, pp. 1-6, July 2019.

[41] S. Lyu, H. Yang, H. Lin and Y. Ren, "A Magnetization State Initialization Control Scheme for Variable Flux Memory Machines without Requiring Position Sensor Information," *IEEE Trans. Transport Electrific.,* doi: 10.1109/TTE.2020.3004734..

[42] A. Athavale, D. J. Erato and R. D. Lorenz, "Enabling driving cycle loss reduction in variable flux PMSMs via closed-loop magnetization state control," *2017 IEEE Energy Conversion Congress and Exposition (ECCE),* pp. 1932-1939, 2017.

[43] C. Yu, T. Fukushige, N. Limsuwan, T. Kato, D. D. Reigosa and R. D. Lorenz, "Variable-Flux Machine Torque Estimation and Pulsating Torque Mitigation During Magnetization State Manipulation," *IEEE Trans. Ind. Appl.,* vol. 50, no. 5, pp. 3414-3422, Sept.-Oct. 2014.

[44] K. Sakai, K. Yuki, Y. Hashiba, N. Takahashi and K. Yasui, "Principle of the variable-magnetic-force memory motor," *Proc. Int. Conf. Elect. Mach. Syst.,* pp. 1-6, Nov. 2009.

[45] M. Ibrahim and P. Pillay, "Design of Hybrid Variable Flux Motors for Enhanced Wide-Speed Performance," *2019 IEEE Energy Conversion Congress and Exposition (ECCE),* pp. 6046-6053, Baltimore, MD, USA, 2019.

[46] A. Athavale, K. Sasaki, B. S. Gagas, T. Kato and R. D. Lorenz, *IEEE Trans. Ind. Appl.,* vol. 53, no. 5, pp. 4318-4326, Sep./Oct. 2017.

[47] B. Basnet, A. M. Aljehaimi and P. Pillay, "Back EMF Analysis of a Variable Flux Machine for Different Magnetization States," *IEEE Trans. Indu. Electron.,* doi: 10.1109/TIE.2020.3026281.

[48] A. Takbash and P. Pillay, "'Magnetization and demagnetization energy estimation and torque characterization of a variable-flux machine," *IEEE Trans. Energy Convers.,* vol. 33, no. 4, p. 1837–1845, Dec. 2018.

[49] A. M. Aljehaimi and P. Pillay, "Braking a Variable Flux-Intensifying IPMSM in Minimal Time," *IEEE Trans. Transp. Electrific.,* vol. 4, no. 4, pp. 867-876, Dec. 2018.

[50] A. M. P. Co., "How Does Cold Temperature Affect Magnets?," [Online]. Available: https://calculators.adamsmagnetic.com/blogs/how-are-magnets-affected-cold. [Accessed 25 06 2021].

[51] "Temperature Effects on Alnico Magnets," Bunting – Berkhamsted, [Online]. Available: https://e-magnetsuk.com/alnico-magnets/temperature-ratings/. [Accessed 25 06 2021].

[52] B. Guo, Y. Huang, F. Peng, Y. Guo and J. Zhu, "Analytical Modeling of Manufacturing Imperfections in Double-Rotor Axial Flux PM Machines: Effects on Back EMF," *IEEE Trans. Magn.,* vol. 53, no. 6, pp. 1-5, June 2017.

[53] X. Ren, D. Li, R. Qu and T. Pei, "Back EMF Harmonic Analysis of Permanent Magnet Magnetic Geared Machine," *IEEE Trans. Ind. Electron.,* early access, 2019.

[54] W. Hua, X. Zhu and Z. Wu, "Influence of Coil Pitch and Stator-Slot/Rotor-Pole Combination on Back EMF Harmonics in Flux-Reversal Permanent Magnet Machines," *IEEE Trans. Energy Convers.,* vol. 33, no. 3, pp. 1330-1341, Sept. 2018.

[55] X. Zhu, W. Hua, W. Wang and W. Huang, "Analysis of Back-EMF in Flux-Reversal Permanent Magnet Machines by Air Gap Field Modulation Theory," *IEEE Trans. Ind. Electron.,* vol. 66, no. 5, pp. 3344-3355, May 2019.

[56] W. Zhao, M. Cheng, W. Hua, H. Jia and R. Cao, "Back-EMF Harmonic Analysis and Fault-Tolerant Control of Flux-Switching Permanent-Magnet Machine With Redundancy," *IEEE Trans. Ind. Electron.,* vol. 58, no. 5, pp. 1926-1935, May 2011.

[57] X. Zhu, M. Jiang, Z. Xiang, L. Quan, W. Hua and M. Cheng, "Design and Optimization of a Flux-Modulated Permanent Magnet Motor Based on an Airgap-Harmonic-Orientated Design Methodology," *IEEE Trans. Ind. Electron.,* vol. 67, no. 7, pp. 5337-5348, July 2020.

[58] C. Xiong, H. Xu, T. Guan and P. Zhou, "A Constant Switching Frequency Multiple-Vector-Based Model Predictive Current Control of Five-Phase PMSM With Nonsinusoidal Back EMF," *IEEE Trans. Ind. Electron.,* vol. 67, no. 3, pp. 1695-1707, March 2020.

[59] G. Liu, X. Chen, X. Zhou and S. Zheng, "Sensorless Commutation Deviation Correction of Brushless DC Motor With Three-Phase Asymmetric Back-EMF," *IEEE Trans. Ind. Electron.,* vol. 67, no. 7, pp. 6158-6167, July 2020.

[60] C. Bi, Z. J. Liu and S. X. Chen, "Estimation of Back-EMF of PM BLDC Motors Using Derivative of FE Solutions," *IEEE Trans. Magn.,* vol. 36, no. 4, pp. 697-700, July 2000.

[61] B. Basnet, A. M. Aljehaimi and P. Pillay, "Effect of Magnetization Pulse Width on the Back EMF of a Variable Flux Machine and on Inverter Sizing," *IECON 2019 - 45th Annual Conference of the IEEE Industrial Electronics Society,* pp. 1028-1033, Lisbon, Portugal, 2019.

[62] A. M. Aljehaimi and P. Pillay, "Operating Envelopes of the Variable-Flux Machine With Positive Reluctance Torque," *IEEE Trans. Transp. Electrific.,* vol. 4, no. 3, pp. 707-719, Sept. 2018.

[63] T. M. Jahns, "Flux-Weakening Regime Operation of an Interior Permanent-Magnet Synchronous Motor Drive," *IEEE Trans. Ind. Appl.,* Vols. IA-23, no. 4, pp. 681-689, July 1987.

[64] L. Masisi, M. Ibrahim and P. Pillay, "Control strategy of a variable flux machine using AlNiCo permanent magnets," *2015 IEEE Energy Conversion Congress and Exposition (ECCE),* Montreal, QC, 2015.

[65] J. Guo, X. Liu and S. Li, "Flux-Weakening Control for Variable Flux Reluctance Machine Excited by Zero-Sequence Current Considering Zero-Sequence Resistive Voltage Drop," *IEEE Trans. Energy Convers.,* early access.

[66] S. Maekawa and e. al., "Study of the Magnetization Method Suitable for Fractional-Slot Concentrated-Winding Variable Magnetomotive-Force Memory Motor," *IEEE Trans. Power Electron.,* vol. 29, no. 9, pp. 4877-4887, Sept. 2014.

[67] Z. Zhang, C. Wang, M. Zhou and X. You, "Flux-Weakening in PMSM Drives: Analysis of Voltage Angle Control and the Single Current Controller Design," *IEEE Journal of Emerg. Sel. Topics Power Electron.,* vol. 7, no. 1, pp. 437-445, March 2019.

[68] Y. Yao, Y. Huang, F. Peng and J. Dong, "Position Sensorless Drive and Online Parameter Estimation for Surface-Mounted PMSMs Based on Adaptive Full-State Feedback Control," *IEEE Trans. Power Electron.,* vol. 35, no. 7, pp. 7341-7355, July 2020.

[69] A. M. Aljehaimi and P. Pillay, "Novel Flux Linkage Estimation Algorithm for a Variable Flux PMSM," *IEEE Trans. Ind. Appl.,* vol. 54, no. 3, pp. 2319-2335, May-June 2018.

[70] A. K. Ziarani and A. Konrad, "A nonlinear adaptive method of elimination of power line interference in ECG signals," *IEEE Trans. Biomed. Eng.,* vol. 49, no. 6, pp. 540-547, June 2002.

[71] A. Takbash, M. Ibrahim, L. Masisi and P. Pillay, "Core Loss Calculation in a Variable Flux Permanent Magnet Machine for Electrified Transportation," *IEEE Trans. Transport. Electrific.,* vol. 4, no. 4, pp. 857-866, Dec. 2018.

[72] C. Desai, "Torque Characterization of Permanent Magnet and Synchronous Reluctance Machines," *Ph.D. dissertation, Dept. of Electrical and Computer Engineering, Concordia University, montreal, QC, Canada,* 2019.

[73] R. Thike and P. Pillay, "Automatic Inductance Measurements of Synchronous Reluctance Machines Including Cross-Saturation Using Real-Time Systems," *2018 IEEE Energy Conversion Congress and Exposition (ECCE), Portland, OR,* pp. 6121-6127, 2018.

[74] M. S. Rafaq and J. Jung, "A Comprehensive Review of State-of-the-Art Parameter Estimation Techniques for Permanent Magnet Synchronous Motors in Wide Speed Range," *IEEE Trans. Indu. Inform.,* vol. 16, no. 7, pp. 4747-4758, July 2020.

[75] X. Xiao, C. Chen and M. Zhang, "Dynamic permanent magnet flux estimation of permanent magnet synchronous machines," *IEEE Trans.on Applied Superconductivity,* vol. 20, no. 3, p. 1085–1088, June 2010.

[76] S. K. e. al, "Torque Ripple Improvement for Interior Permanent Magnet Synchronous Motor Considering Parameters With Magnetic Saturation," *IEEE Trans. Magnet.,* vol. 45, no. 10, pp. 4720-4723, Oct. 2009.

[77] W. Tong, S. Li, X. Pan, S. Wu and R. Tang, "Analytical Model for Cogging Torque Calculation in Surface-Mounted Permanent Magnet Motors With Rotor Eccentricity and

Magnet Defects," *IEEE Transactions on Energy Conversion,* vol. 35, no. 4, pp. 2191-2200, Dec. 2020.

[78] M. Cheng, K. T. Chau, C. C. Chan, E. Zhou and X. Huang, "Nonlinear varying-network magnetic circuit analysis for doubly salient permanent-magnet motors," *IEEE Transactions on Magnetics,* vol. 36, no. 1, pp. 339-348, Jan. 2000.

[79] G. Feng, C. Lai and N. C. Kar, "A Novel Current Injection-Based Online Parameter Estimation Method for PMSMs Considering Magnetic Saturation," *IEEE Transactions on Magnetics,* vol. 52, no. 7, pp. 1-4, July 2016.

[80] N. Imai, S. Morimoto, M. Sanada and Y. Takeda, "Influence of Magnetic Saturation on Sensorless Control for Interior Permanent-Magnet Synchronous Motors With Concentrated Windings," *IEEE Transactions on Industry Applications,* vol. 42, no. 5, pp. 1193-1200, Sept.-Oct. 2006.

[81] C. Mademlis and V. G. Agelidis, "On considering magnetic saturation with maximum torque to current control in interior permanent magnet synchronous motor drives," *IEEE Transactions on Energy Conversion,* vol. 16, no. 3, pp. 246-252, Sept. 2001.

[82] B. Stumberger, G. Stumberger, D. Dolinar, A. Hamler and M. Trlep, "Evaluation of saturation and cross-magnetization effects in interior permanent-magnet synchronous motor," *IEEE Trans. Ind. Appl.,* vol. 39, no. 5, pp. 1264-1271, Sept.-Oct. 2003.

[83] G. Stumberger, B. Polajzer, B. Stumberger, M. Toman and D. Dolinar, "Evaluation of experimental methods for determining the magnetically nonlinear characteristics of electromagnetic devices," *IEEE Transactions on Magnetics,* vol. 41, no. 10, p. 4030–4032, Oct 2005.

[84] X. Liu, H. Chen, J. Zhao and A. Belahcen, "Research on the Performances and Parameters of Interior PMSM Used for Electric Vehicles," *IEEE Trans. Indu. Electron.,* vol. 63, no. 6, pp. 3533-3545, June 2016.

[85] S. Wiedemann, R. M. K. S. Hall and M. Alaküla, "Dynamic Testing Characterization of a Synchronous Reluctance Machine," *IEEE Trans. Ind. Appl.,* vol. 54, no. 2, pp. 1370-1378, March-April 2018.

[86] R. Thike and P. Pillay, "Automated Current Control Method for Flux-Linkage Measurement of Synchronous Reluctance Machines," *IEEE Trans. Ind. Appl.,* vol. 56, no. 2, pp. 1464-1474, March-April 2020.

[87] J. Im, W. Kim, K. Kim, C. Jin, J. Choi and J. Lee, "Inductance Calculation Method of Synchronous Reluctance Motor Including Iron Loss and Cross Magnetic Saturation," *IEEE Trans. Magn.,* vol. 45, no. 6, pp. 2803-2806, June 2009.

[88] R. Thike and P. Pillay, "Characterization of a Variable Flux Machine for Transportation Using a Vector-Controlled Drive," *IEEE Trans. Transp. Electrific.,* vol. 4, no. 2, pp. 494-505, June 2018.

[89] S. H. Hwang, J. M. Kim, H. V. Khang and J. W. Ahn, "Parameter identification of a synchronous reluctance motor by using a synchronous PI current regulator at a standstill," *J. Power Electron.,* vol. 10, p. 491–497, Sep. 2010.

[90] B. Gagas, T. Fukushige, N. Limsuwan, C. Yu, K. Akatsu and R. D. Lorenz, "Suggested design space in a PMSM parameter plane for variable flux machines," *2013 International Electric Machines & Drives Conference,* pp. 549-556, Chicago, IL, 2013.

[91] J. C. Akiror, R. S. Kaarthik, J. Wanjiku, P. Pillay and A. Merkhouf, "Closed-Loop Control for a Rotational Core Loss Tester," *IEEE Transactions on Industry Applications,* vol. 54, no. 6, pp. 5888-5896, Nov.-Dec. 2018.

[92] A. M. Aljehaimi and P. Pillay, "A Closed-loop Magnetization State Controller for Variable-Flux IPMSMs," *2019 IEEE Energy Conversion Congress and Exposition (ECCE),* pp. 5610-5615, Baltimore, MD, USA, 2019.

[93] S. Abourida, C. Dufour, J. Belanger, T. Yamada and T. Arasawa, "Hardware-In-the-Loop Simulation of Finite-Element Based Motor Drives with RT-LAB and JMAG," in *2006 IEEE International Symposium on Industrial Electronics*, Montreal, Que., 2006.

[94] H. H. Eldeeb, A. Berzoy and O. Mohammed, "Stator Fault Detection on DTC-Driven IM via Magnetic Signatures Aided by 2-D FEA Co-Simulation," *IEEE Trans. Magnetics,* vol. 55, no. 6, pp. 1-5, June 2019.

[95] Y. Li, H. Deng, X. Xu and W. Wang, "Modelling and testing of in-wheel motor drive intelligent electric vehicles based on co-simulation with Carsim/Simulink," *IET Intelligent Transport Systems,* vol. 13, no. 1, pp. 115-123, 2019.

[96] D. Shu, X. Xie, Z. Yan, V. Dinavahi and K. Strunz, "A Multi-Domain Co-Simulation Method for Comprehensive Shifted-Frequency Phasor DC-Grid Models and EMT AC-Grid Models," *IEEE Trans. Power Electron.,* vol. 34, no. 11, pp. 10557-10574, Nov. 2019.

[97] B. Basnet and P. Pillay, "Co-simulation Based Electric Vehicle Drive for a Variable Flux Machine," *2020 IEEE Transportation Electrification Conference & Expo (ITEC),* pp. 1133-1138, Chicago, IL, USA, 2020.

[98] R. Venkatraman, S. K. Khaitan and V. Ajjarapu, "Dynamic Co-Simulation Methods for Combined Transmission-Distribution System With Integration Time Step Impact on Convergence," *IEEE Trans. Power Systems,* vol. 34, no. 2, pp. 1171-1181, March 2019.

[99] T. Longfei, H. Zhiping and X. Zhihong, "Neural Network-Based Co-Simulation Technology for Intelligent Contactors," *IEEE Trans. Magnetics,* vol. 56, no. 2, pp. 1-8, Feb. 2020.

[100] C. M. Apostoaia, "AC machines and drives simulation platform," *2013 International Electric Machines & Drives Conference,* Chicago, IL, 2013.

[101] JMAG, "Iron Loss Analysis of an IPM Motor Accounting for a PWM -Direct Link," *JMAG-Designer,* Mar 2009.

[102] C. Schulte and J. Böcker, "Co-simulation of an electric traction drive," in *2013 International Electric Machines & Drives Conference*, Chicago, IL, 2013.

[103] L. D. Leonardo, F. Parasiliti, M. Tursini and M. Villani, "Transient analysis of PM synchronous motor drives by finite element model co-simulation," in *IECON 2013 - 39th Annual Conference of the IEEE Industrial Electronics Society*, Vienna, 2013.

[104] C. Irimia, M. Grovu, C. Husar, D. Fodorean and C. Antonya, "Co-Simulation Analysis for an Electric Vehicle Powered by a High-Speed Electrical Machine," in *2017 IEEE Vehicle Power and Propulsion Conference (VPPC)*, Belfort, 2017.

[105] S. S. Nair, J. Wang, L. Chen, R. Chin, I. Manolas and D. Svechkarenko, "Prediction of 3-D High-Frequency Eddy Current Loss in Rotor Magnets of SPM Machines," *IEEE Trans. Magnetics,* vol. 52, no. 9, pp. 1-10, Sept. 2016.

[106] A. G. Sarigiannidis and A. G. Kladas, "Switching Frequency Impact on Permanent Magnet Motors Drive System for Electric Actuation Applications," *IEEE Transactions on Magnetics,* vol. 51, no. 3, pp. 1-4, March 2015.

[107] M. Boesing, M. Niessen, T. Lange and R. D. Doncker, "Modeling spatial harmonics and switching frequencies in PM synchronous machines and their electromagnetic forces," *2012 XXth International Conference on Electrical Machines,* pp. 3001-3007, Marseille, 2012.

[108] K. Basu, J. S. S. Prasad and G. Narayanan, "Minimization of torque ripple in PWM AC drives," *IEEE Trans. Ind. Electron.,* vol. 56, no. 2, p. 553–558, Feb. 2009.

[109] L. Chang, W. Lee, T. M. Jahns and J. Kim, "Comparative Analysis of PWM Power Losses in IPM Machines with Different Modulation Schemes Using Wide-Bandgap-Based Inverters," *2020 IEEE Energy Conversion Congress and Exposition (ECCE),* pp. 3629-3636, Detroit, MI, USA, 2020.

[110] L. Chang and T. M. Jahns, "Prediction and Evaluation of PWM-Induced Current Ripple in IPM Machines Incorporating Slotting, Saturation, and Cross-Coupling Effects," *IEEE Trans. Indu. Appl.,* vol. 54, no. 6, pp. 6015-6026, Nov.-Dec. 2018.

[111] A. Balamurali, G. Feng, C. Lai, J. Tjong and N. C. Kar, "Maximum Efficiency Control of PMSM Drives Considering System Losses Using Gradient Descent Algorithm Based on DC Power Measurement," *IEEE Transactions on Energy Conversion,* vol. 33, no. 4, pp. 2240-2249, Dec. 2018.

[112] J. L. Besnerais, V. Lanfranchi, M. Hecquet and P. Brochet, "Characterization and Reduction of Audible Magnetic Noise Due to PWM Supply in Induction Machines," *EEE Trans. Ind. Electron.,* vol. 57, no. 4, pp. 1288-1295, April 2010.

[113] A. Krings, J. Soulard and O. Wallmark, "PWM influence on the iron losses and characteristics of a slotless permanent-magnet motor with SiFe and NiFe stator cores," *IEEE Trans. Ind. Appl,* vol. 51, no. 2, p. 1475–1484, Mar. 2015.

[114] JMAG-Designer and JMAG-Express, software components of JSOL Corp (Japan). Powersys Inc. is the JMAG's Distributor in North America, Middleton, WI.

[115] M. Huang, Y. Deng, H. Li and J. Wang, "Torque ripple suppression of PMSM using fractionalorder vector resonant and robust internal model control," *IEEE Trans. Transport. Electrific.,* doi: 10.1109/TTE.2021.3053063.

[116] M. V. d. Paula, T. A. d. S. Barros, H. S. Moreira, E. H. Catata, M. G. Villalva and E. R. Filho, "A Dahlin Cruise Control Design Method for Switched Reluctance Motors with Minimum Torque Ripple Point Tracking Applied in Electric Vehicles," *IEEE Trans. Transport. Electrific.,* doi: 10.1109/TTE.2020.3019997.

Appendix

Table 0-1. Variable-flux IPMSM parameters

Number of poles	6
Number of slots	27
Magnet material	AlNiCo 9
magnet remnant flux density (T)	1.08
Rated current (A)	10
Rated torque (N.m)	36.8
Rated speed (rpm)	1200
Resistance at ambient temperature (Ω)	1.3
d and $q-axis$ inductance at rated current (mH)	52 & 36